MECHANICS OF DUCTILE FRACTURE AND SEGMENTED CHIP FORMATION IN CUTTING OF METALS

by

Mojib Saei

A Dissertation

Submitted to the Faculty of Purdue University

In Partial Fulfillment of the Requirements for the degree of

Doctor of Philosophy

School of Industrial Engineering

West Lafayette, Indiana

May 2021

THE PURDUE UNIVERSITY GRADUATE SCHOOL

STATEMENT OF COMMITTEE APPROVAL

Dr. Srinivasan Chandrasekar, Chair

School of Industrial Engineering

Dr. Kevin Trumble

School of Materials Engineering

Dr. Ramses Martinez

School of Industrial Engineering

Dr. David Johnson

School of Materials Engineering

Approved by:

Dr. Abhijit Deshmukh

To my mother, father, sister and brother, with love

ACKNOWLEDGMENTS

I like to thank my advisors, Prof. Srinivasan Chandrasekar and Kevin Trumble, for their excellent support and advising. Not only they helped me learn about ups and downs of machining processes, but also let me explore many other interesting topics. Furthermore, their general support and constant encouragement made the graduate experience enjoyable and fruitful. I am also thankful to my committee member, Prof. Ramses Martinez for being attentive, and for providing great advice inside and outside the classroom. I am especially thankful to my other committee member, Prof. David Johnson, whose teachings on fracture of materials motivated me to work on ductile fracture in machining.

The author acknowledges his colleagues for support throughout his graduate studies. In particular, I want to send my thanks to James, Anirudh, Anirban, Pinaki, Jason, Mohammed, Stiven, Koushik, Ho, Xiaolong, and Yang.

The author also would like to thank his loving mother, father, sister, and brother. Without them, this dissertation would not have been possible.

Finally, the author would like to thank Purdue University for providing this opportunity to pursue my PhD in a field that I value.

This work was supported in part by NSF Grants CMMI 2100568 and DMR 1610094; and the US Department of Energy EERE program via Award No. DE-EE0007868.

TABLE OF CONTENTS

LIST OF TABLES

LIST OF FIGURES

ABSTRACT

The machining of metals is of significant technological importance for discrete products manufacturing encompassing automotive, aerospace, energy systems and biomedical sectors. Any gains obtained by improving surface quality and increasing tool life can have important impacts in this vital manufacturing sector. Obtaining such improvements is closely tied to reducing forces and specific energy, and, hence, directly to the mechanics of the material removal process (chip formation).

Typically, there are four principal chip types in metal cutting, each corresponding to a different (underlying) plastic flow mode with characteristic deformation attributes. In this dissertation, we examine mechanics of segmented chip formation, one of the principal chip types, with a view to understanding the underlying flow dynamics and instabilities, forces and deformation, development of chip morphology and attributes, and how segmentation can be controlled. This is done using high speed *in situ* imaging of material flow and deformation, complemented by force and surface topography characterization, using varied material systems that show a strong propensity for segmentation.

It is shown that ductile fracture plays a key role in the segmentation, with periodic fracture events being nucleated on the back (free) surface of the chip, and each fracture then propagating towards the tool cutting edge, to create the segmented chip/flow. Furthermore, the crack nucleation triggering the fracture occurs at a critical strain, that is independent of the deformation geometry. Two types of segmentation morphologies are uncovered, each with its distinct (characteristic) force signature. In the first type, the segmentation runs straight across the chip width, and the force profile shows an oscillation at the same frequency as the segmentation frequency. In the second type, the segmentation meanders across the chip width, and the force trace in this case is fairly

steady with no oscillation. The strain field with segmented flow is non-uniform, with significant localization of the strain occurring in the crack propagation zone.

Based on an understanding of the deformation conditions and stress state prevailing in the fracture zone, we demonstrate material-agnostic strategies to control the segmentation. This control includes 1) suppression of the segmentation by application of a second constraining die (constraint) located directly across from the cutting tool – Hybrid Cutting Extrusion (HCE); this results in the chip being formed as a continuous strip of uniform thickness with uniform laminar plastic flow and homogeneous deformation; and 2) inducing segmentation to occur in ductile metals (e.g., Cu) that would normally not segment in metal cutting, by utilizing a surface medium, applied to the initial workpiece surface, to locally embrittle the metal in the chip-formation zone – a mechanochemical effect. The HCE, by suppressing the segmentation, offers opportunities for use of machining as a forming process to produce sheet metals, even from low-workability alloys, in a single step of deformation, by chip formation. The deliberate triggering of segmentation via a mechanochemical effect offers opportunities to cut the so-called “gummy” metals with smaller forces and energy. Our understanding of deformation mechanics of segmentation has other benefits for machining process, including improvement of surface finish, cutting force control/reduction, and for study of ductile fracture phenomena.

1. INTRODUCTION

Machining operations with metals such as turning, drilling and milling constitute a vital segment of the manufacturing domain, encompassing sectors as diverse as automotive, aerospace, energy systems and biomedical industries. Machining is usually employed in the latter stages of the manufacturing process chain to achieve desired dimensional accuracy and surface finish [1]. Equally importantly in modern manufacturing, the integrity of surfaces created by machining processes has become a critical characteristic. The defining attributes of surface integrity, and more generally surface quality, go beyond surface finish; it includes parameters such as microstructure, and residual plastic strain and stress [2]. The quality of the machined surface is in large part governed by the mechanics of the chip formation process and the large-strain deformation field underlying this chip formation.

The mechanics of the unit interaction in chip formation, across machining processes, is well-captured in the interaction between a sharp wedge (tool) and a metal surface as depicted in Figure 1-1 under plane-strain conditions. Here the tool is idealized as removing a thin sliver of material (chip) of undeformed chip thickness (t_0) by intense shear deformation that is confined to a thin region, often idealized as a plane—the Merchant-Piispaanen shear plane model of chip formation [3], [4]. The geometry of the cutting in Figure 1-1 is one of plane strain with no deformation assumed to occur into the plane of the paper. The tool rake angle, α= 0°, for this case; this rake angle which is the angle of inclination between the tool rake face and the vertical in the figure defines the tool geometry. The chip formed is continuous and the deformation field underlying the chip formation, homogeneous, with smooth streaklines (the loci of all the points that have passed continuously through a particular spatial location in the past) as shown in the figure. The attributes of the cut surface are dependent on the chip formation, for a large fraction of the cutting specific

energy (> 65%) is due to the plastic deformation work in the primary deformation zone (shear plane) [1]. The remainder is mostly due to frictional dissipation at the tool-chip contact, with only a small fraction going into deforming the workpiece surface. Strains of 1–10 in the chip are common, as reflected in a significant thickening of the chip under the plane-strain deformation conditions.

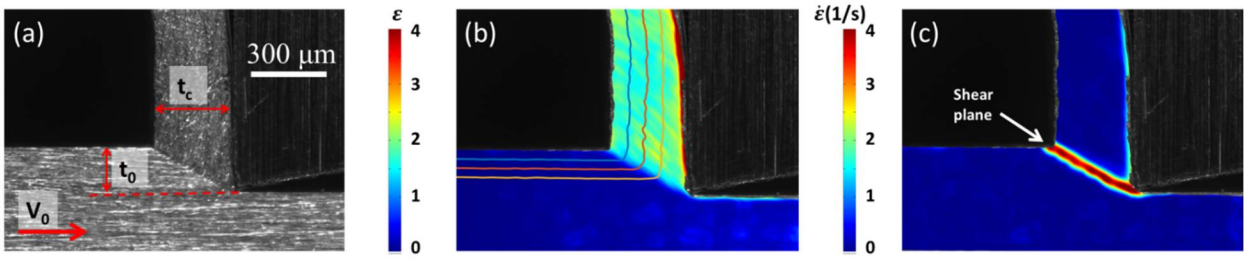

Figure 1-1. Chip formation in machining of hardened copper showing smooth laminar flow typical of a shear plane model. Principal parameters of the cutting process are also marked. (a) Raw image, (b) strain field with superimposed streaklines, and (c) von Mises (effective) strain rate field. The strain rate field which is a measure of the incremental deformation demarcates the deformation zone; in the present case this resembles a shear plane. $\alpha = 0°$, $V_0 = 1$ mm/s, $t_0 = 150$ μm.

The continuous chip with uniform deformation (type 2 chip) shown in Figure 1-1 (also Figure 1-2b) is but one type of commonly encountered chip. It arises most commonly in the cutting of metals of moderate workability, such as Al and Cu alloys, and low to medium carbon steels. Three other widely encountered chip morphologies are also shown in Figure 1-2, each characterized by a non-uniform deformation in the chip [5], [6]. The type 1 chip (Figure 1-2a) forms by large amplitude folding triggered by buckling of a thin surface layer ahead of the tool; the underlying flow mode has been termed as a sinuous flow mode [6]–[9]. This chip occurs in cutting of soft annealed metals and highly strain-hardening metals, and results in high forces and poor surface finish. Furthermore, some significant fraction of the cutting energy (~ 15%) is expended in straining the workpiece surface [7]. The chip deformation is quite non-uniform with

the strains varying by a factor of 2–3, and the chip morphology is characterized by mushroom shaped structures along its free surface. The type 4 chip (Figure 1-2d) is associated with a deformation field that is highly non-uniform due to the occurrence of shear bands. In this chip, which forms with Ti and Ni alloys, the strain variations between the band and the adjoining regions are quite large, often as much as a factor of 10–50 [10]–[12]. This intense strain localization is a consequence of catastrophic adiabatic shear, resulting in a flow instability that is somewhat akin to necking in a uniaxial tensile test. The chip has a characteristic saw-tooth morphology that reflects the underlying strain heterogeneity. The type 3 chip (Figure 1-2c), the focus of this study, has a morphology similar to the type 4 chip, but fracture plays an important role in its formation [13]–[16]. The strain heterogeneity (factor of 2–3) is also much less than in the type 4 chip [17]. It has been suggested that the saw-tooth or segmented chip morphologies give rise to oscillations in the cutting force with adverse effects on workpiece surface quality (e.g., chatter vibrations, poor surface finish and non-uniform deformation state) and tool life.

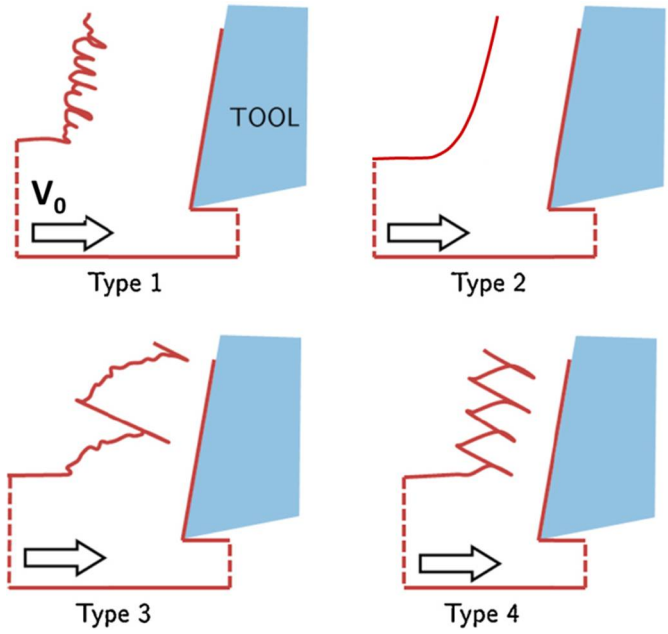

Figure 1-2. Four common chip morphologies in cutting of metals: (a) continuous chip with mushroom shaped-features on back (free) surface of chip typical of sinuous flow, (b) continuous chip of constant thickness typical of laminar flow, (c) segmented or saw-tooth chip with periodic fractures, and (d) shear banded (shear-localized) chip with regions of intense flow localization occurring at periodic intervals. There is a one-tone correspondence between the chip morphology and underlying flow pattern/mode. Adapted from references [5], [17].

Since the quality of the machined surface and the process performance are determined by the type of chip, there has been much effort devoted to understanding the mechanics of chip formation even though the chip is part of the "waste" stream. Most of this prior work has utilized post-cutting observations of chip and workpiece surface attributes besides measurement of forces and deformation. Based on these observations, many important aspects of the mechanics of chip formation have been elucidated resulting in improvements to the cutting processes. However, key details of the deformation instabilities (e.g., buckling, fracture, shear band development) that trigger the non-steady deformation modes have remained nebulous.

In recent years, there has been an attempt to study the flow instabilities using direct *in situ* observations of the chip formation process (using high-speed photography) and the underlying

deformation field[9], [17]–[19]. This has enabled important details of the development of flow instabilities, and the micromechanics of the deformation to be captured. It has led to uncovering of a new mesoscale plastic flow mode—sinuous flow [9]; solution of problems such as why soft metals are difficult to cut earning them the title “gummy” [7], [8], and demonstration of plastic boundary layers with very small viscosities in shear bands [12], [20]. The implications of these findings extend well beyond machining, impinging on areas such as large-strain deformation of metals, plastic flow instabilities, mechanochemical effects in plasticity and pattern formation on surfaces.

1.1 Problem Statement

The objective of the dissertation is to understand the mesoscale mechanics of type 3 (segmented) chip formation and underlying deformation/fracture. This is done via the *in situ* observational approach, developed in prior work. We characterize the evolution of the deformation field, and the underlying fracture instability in both the nucleation and development stages. Using high-speed imaging, in conjunction with image correlation analysis, the main features of the deformation and fracture processes are described, both in terms of the flow phenomena, and quantitatively via deformation fields. Based on this understanding, we demonstrate control of the deformation/fracture (segmentation) instability. By ‘control’, here, is meant not only suppression of the segmentation but also means to induce it to occur in metals where segmented flow would not be the norm. We also address microstructural origins of the segmented flow, examining contribution of surface features in nucleation of segmentation. Besides its relevance for improving machining processes, improved understanding of segmentation mechanics offers potentially new routes for studying ductile failure in metals.

1.2 Hypothesis

The hypotheses being explored in this thesis are 1) segmentation is initiated on the free surface of the workpiece, ahead of the advancing tool, by nucleation of a crack that then propagates inward towards the tool tip, and 2) segmentation can be controlled via changes in deformation geometry in the zone where it is initiated.

In addressing this problem and hypothesis, we hope to also clarify and answer several questions and misconceptions about the segmentation process in cutting. These pertain to location of segmentation initiation and details of evolution of segmentation process; any criteria can be established for onset of segmentation, assuming it is fracture driven; whether segmentation always leads to force oscillations and adverse effects on workpiece surface quality, as is commonly assumed; is segmented chip formation an energetically favorable mode compared to the sinuous and laminar flow modes; and nature of the deformation/flow field underlying the segmentation process.

2. BACKGROUND

In this chapter, we review a) prior relevant work related to chip formation b) fracture phenomena in workpiece material deformation zone, and c) application of Particle Image Velocimetry (PIV), an image correlation technique, to study material flow in large strain deformation, as in cutting of metals.

2.1 Chip formation in metal cutting and underlying material flow

Figure 2-1 shows a schematic of plane strain machining, wherein a sharp, wedge-shaped tool removes a preset depth (t_0) and width (w) of material—the chip—by moving in a direction perpendicular to its cutting edge. The deformation rate or machining speed is V_0. The chip forms by shear in a narrow deformation zone idealized as a shear plane OA—this is the model of chip formation proposed by Merchant and Piispaanen in the 1940s [3], [4] It is based on observations of the type 2 continuous chip with the underlying material flow being uniform and laminar (smooth). Measurement of the undeformed (t_0) and deformed chip thicknesses (t_c) provides an estimate of the shear strain (γ) for this shear plane model as [1], [21]:

$$\gamma = \frac{\lambda}{\cos(\alpha)} + \frac{1}{\lambda \cos(\alpha)} - 2\tan(\alpha) \tag{2-1}$$

where α is the tool rake angle and λ is the chip thickness ratio t_c/t_0. The latter is typically greater than 1 in conventional plane-strain machining due to the shear deformation. The corresponding von Mises effective strain is:

$$\varepsilon = \frac{1}{\sqrt{3}}\gamma \tag{2-2}$$

It is this von Mises strain (and strain rate) that is reported in the results.

A range of strains can be imposed in the chip by appropriate selection of α (Equation 2-1), with plastic strains of up to 15 in a single pass being not atypical of the machining of ductile metals such as annealed copper [22]. The strain given by Equation 2-1 is the strain in the primary deformation zone (see Fig. 2-1)

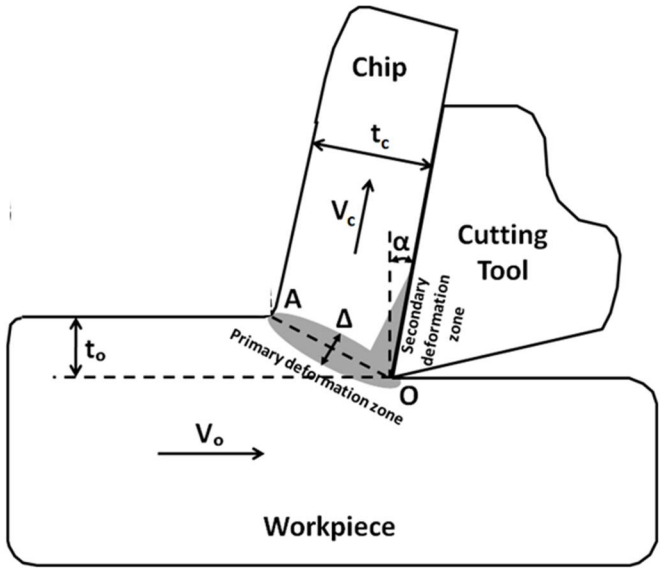

Figure 2-1. Schematic of plane strain (2D) machining showing geometric parameters and deformation zones.

Equation 2-1 assumes that all the strain is imposed at a plane in what is essentially an upper bound model for the deformation. This is perhaps the most widely used model in machining because of its simplicity. In this model, since the chip strain is imposed over a plane (infinitesimally thin), the strain rate in the deformation zone is infinitely large, since the deformation zone is a plane of infinitesimally small thickness. In practice, the deformation zone (OA), is not a plane but a zone of small, but finite, thickness (Δ), see Figure 2-1. Even when the deformation zone is somewhat thicker, the largest increments in strain are still quite localized and imposed over a narrow region [23]–[25]. Equally importantly the zone is found to extend slightly into the workpiece subsurface below the tool cutting edge [26]. As a result, the strains in the

workpiece surface layer are also predicted to be quite large at the surface and to decrease with depth into the subsurface over a region that is tens of micrometers in extent [21], [27]–[29].

The strain rate is a measure of the strain increment imposed as the tool advances by a small distance. Consequently, the region of intense strain rate represents the deformation zone; this zone corresponds also to the region wherein the change in velocity of material flow is a maximum. The effective strain rate in the primary deformation zone is well-approximated as (Figure 2-1) [1], [21]:

$$\frac{d\bar{\varepsilon}}{\mathrm{dt}} = \frac{\gamma V_0}{\sqrt{3}\Delta} \tag{2-3}$$

where γ is obtained using Equation 2-1 or measured in some manner, and Δ is the mean thickness (width) of the deformation zone. The strain rate in machining can thus be controlled using V_0.

The average temperature in the primary deformation zone (T) can be estimated using thermal analyses that are based on the shear plane model for primary deformation and frictional heating in a thin secondary deformation zone at the tool-chip contact. The estimation can be done using either measured forces and velocities, or strain rate, strain and velocity, as inputs, or combinations thereof [1], [30]. Alternatively, T can be measured using thermocouple or thermographic methods. Thus, T can be varied by changing the machining input parameters.

While Equation 2-1 provides a straightforward estimate of the strain in the chip for the laminar flow case, it is not applicable to the other types of chip formation, see Figure 1-2. A deviation from laminar flow is normally the result of an instability in the plastic flow – examples include shear banding [31], [32], tensile necking [33], plastic buckling [8], [34] and kinking [35].

There are various ways to categorize chip morphologies [5], [36], the classification by Nakayama in Figure 1-2 is most useful for we can link the morphology in this scheme to the underlying flow pattern [5], [37]. In this scheme the type 1 chip with stacked folds and mushroom like free-surface morphology arises from sinuous flow with large-amplitude folding [7], the type

2 smooth continuous chip from laminar flow, the type 3 saw-tooth chip from segmented flow characterized by fracture, and the closely related type 4 saw-tooth chip from shear band flow with intense localization of strain [10]. In this study, we focus on type 3 (segmented) chip formation and how the underlying flow evolves.

Type 3 and type 4 flow both result in a serrated chip with periodic steps at the free surface which is a result of localized flow at bands of concentrated shear. However, the flow localization in type 3 chip is the result of (ductile) fracture whereas material softening (due to adiabatic shear) is the root cause of localized flow in type 4 flow.

It is necessary to pay attention to the features in these two types of chips, since their morphologies closely resemble one another. Both segmented and shear band chips exhibit variations in chip thickness and have a saw-tooth shape with pointy edges (Figure 1-2). Both are also characterized by heterogeneous straining. But the strain localization is more intense in the shear banded type 4 chip (10–50 fold strain variation), with the individual chip segments being separated by narrow regions of intense shear [38]. In contrast the type 3 chip shows smaller strain heterogeneity, only a factor of 2–3, between the segmented regions and the segment interfaces.

Distinct mechanisms have been proposed for the segmented and shear banded chips. Segmentation has been suggested to occur as a result of fracture instability in the primary deformation zone [5], [16], [39]. Nakayama [5] and Shaw [13] suggested that cracks initiate periodically at the free surface of the workpiece ahead of the advancing tool and propagate downward along a shear plane toward the tool tip, this being the root cause of the segmented chip. On the other hand shear bands are known to be a result of catastrophic shear, with localized heat generation leading to thermal softening and a flow instability [40]. Strain rate plays a positive role in shear band promotion [10], [40], but in the case of the segmented chip the relation of

deformation speed to segmentation is complicated [39]. An increase in cutting speed has opposing effects: an increase in the tendency for saw-tooth chip formation due to promotion of brittle behavior at the higher strain rate, but a decrease in segmentation propensity due to thermal softening. Overall shear bands dominate at higher cutting speeds, while the segmented chip is more prevalent at lower speeds. However, both segmentation and shear banding are work-material dependent. Shear bands are commonly seen in high speed machining of Ti and Ni alloys [10], [41]. Segmented chip formation is more common in cutting of less-ductile metals (e.g., 2-phase brass [17], hardened steel) and at low speeds. Komanduri et al. [11] obtained segmented chips for AISI 4340 Steel at speeds below 15 m/min; but this morphology changed to continuous chip in the speed range of 30 to 60 m/min. Shear bands were observed when machining AISI 1045 steel at a cutting speed of 125 m/min or higher.

While the effects of temperature and strain rate in formation of segmented chip are not fully understood, it has been suggested that segmentation occurs at a critical surface strain [5], [16]. Nakayama's work implies that brittleness of material plays a role and that the roughness of the surface contributes to the chip "brittleness", the roughness serving as pre-cursor flaws [42].Walker and Shaw [43] proposed a mechanism for the segmented chip that involves void formation in the deformation zone, evolution of voids into microcracks, and coalescence of these cracks leading to partial fracture in the chip. Instability in the secondary deformation at the rake face, resembling stick-slip, has been proposed as another mechanism for segmentation [44], akin to relaxation oscillations of the type envisaged by van der Pol [45].

Since segmented chip formation involves both large-strain deformation and fracture, a direct *in situ* examination of this type of chip formation, including of the deformation fields, is likely to provide insight into ductile fracture and damage in metals. Thus more information may

be extracted by examination of a segmented chip than from a classic laminar chip [46]. Examination of the segmented chip formation could also help better place it in the larger framework of chip types. The possibility also exists that since fracture likely interrupts the evolution of large-scale plastic deformation, and the deformation is confined to local regions, the segmented chip may be more favorable from the viewpoint of machining specific energy than the laminar flow chip. These are some of the reasons guiding the present *in situ* study of segmented chip formation and the underlying flow.

2.2 Ductile Fracture and Formation of Segmented Chip

The problem of ductile fracture in metals, especially under conditions of large-strain deformation, is still an open problem in fracture mechanics. Bridgman's pioneering work [47], [48] and that of others like Pugh [49], [50] showed that the superimposition of hydrostatic pressure in the deformation zone can significantly delay the fracture process in metals. In fact, the presence of significant hydrostatic pressure and high temperatures is the main reason why large shape changes can be performed by cutting and forming processes in metals, that is strains well in excess of failure in a tensile test.

The change in fracture properties of metals as a function of pressure has been studied by several investigators. French and Weinrich studied the influence of hydrostatic pressure on tensile deformation and fracture of aluminum [51], copper [52], α-brass [53] and free machining brass [54]. The general behavior observed was that the natural strain at fracture increases approximately linearly with hydrostatic pressure up to a critical hydrostatic pressure. For pressures greater than the critical value, the strain at fracture was almost constant. They found that variation of fracture behavior with pressure to be related to a change in the fracture mechanism. For example, tensile fracture of commercial aluminum occurred by a double-cup mechanism at pressures of up to

125MPa, while failure occurred with necking down to a chisel point, with no void development, at pressures above 150MPa [51]. Similar behavior was also seen in copper, with chisel point fracture dominating at pressures greater than 300 MPa [52]. This mechanism involves many highly localized shear bands which finally produce a chisel point.

It is also important in ductile failure to distinguish between the nucleation and subsequent growth of cracks. McClintock [55] proposed nucleation and growth criteria to explain different fracture types. He claimed that pure Mode I (normal) fracture is unlikely to exist except in cleavage. In other work [56], he discussed the effects of crack sharpness and crack angle using studies with plane-strain grooved specimens of OFHC copper and aluminum in tension.

The role of damage accumulation in influencing fracture in metals is a recurring theme in ductile fracture mechanics and especially important for processes involving large-strain deformation. Based on this damage accumulation hypothesis, various criteria have been proposed for ductile fracture of metals. Johnson and Cook [57] considered fracture characteristics of metals subjected to torsion, Hopkinson bar tests, and quasi-static tensile tests. They developed a cumulative-damage fracture model which expresses the strain at fracture as a function of the strain rate, temperature, and pressure. McClintock [58] developed a ductile fracture criterion based on studies of specimens with cylindrical holes, subjected to a prescribed history of applied principal components of stress and strain. Rice and Tracey [59] introduced a stress triaxiality function to describe the growth of a spherical void in a general remote field. LeRoy et al. [60] proposed a ductile fracture model by examining void growth and accumulation of damage during tensile loading. These criteria were limited to mostly tensile types of loading, more relevant to sheet metal forming than bulk deformation processes or cutting.

The pioneering study of ductile failure in the context of forming and cutting processes is that by Cockcroft and Latham [61]. They postulated that fracture was controlled by an integrated quantity of stress and strain ($\int \sigma . d\varepsilon$), very much analogous to plastic work accumulation along the strain path, reaching a critical value, with the caveat that at least one of the principal tensile stresses be tensile. If the stress quantity in the integrand is constant, then this criterion is essentially a critical strain criterion of failure. Subsequent advances have involved only minor modifications to the Cockcroft-Latham approach. Oh et al. [62] modified the criterion by normalizing the maximum principal tensile stress by the equivalent stress. Clift et al. [63] introduced effective stress into the integrated damage function, instead of maximum principal tensile stress. However, the range of applicability of these criteria is still under debate. Bao and Wierzbicki [64] have compared several of these Cockcroft-Latham type criteria with experimental results. Based on this type of comparison, they concluded that the functional form of the fracture locus is determined by the local stress triaxiality (η) (ratio of hydrostatic stress (σ_m) to effective stress ($\bar{\sigma}$)) ($\eta = \frac{\sigma_m}{\bar{\sigma}} = \frac{\frac{\sigma_1+\sigma_2+\sigma_3}{3}}{\bar{\sigma}}$). They claimed that the criteria were generally well established in the range of high triaxiality (> 0.4) and negative stress triaxiality (between -1/3 and zero). By performing tests in the intermediate range of stress triaxiality, they proposed fracture loci for this range of stress-strain space [65]. In a later publication, Wierzbicki [66] compared seven fracture models that are compatible with the newly suggested fracture loci. Perhaps the most important conclusion from Wierzbicki's work is that ductile fracture will not occur when the stress triaxiality is < -1/3. This prediction can be directly tested in the current work.

The analysis of fracture is greatly aided by examination of the topography and microscopic features (fractography) [67], [68]. This type of fractographic investigation has provided insights into also how microstructure influences fracture, see for example the analysis of ductile-to-brittle

transition in steels [69], [70], and the role of grain size in fracture of bismuth by Dembowski et al. [71]. The latter study considered effect of hydrostatic pressure on failure. It showed that the brittle-ductile transition was sensitive to grain size, but with the transition pressure increasing with the grain size. Fractographic investigation is also useful for identifying the fracture mechanisms such as cleavage, intergranular vs transgranular fracture, and shear fracture.

It is critical that material failure must not occur in metal forming processes, since the product must not have defects [72]. It is unclear if we can hold machining processes to the same standard. This is because of the question—what is the product in a machining process? the chip or the workpiece? Certainly, the workpiece should not contain defects arising from material failure during the cutting process. But from the chip perspective, ductile fracture could be beneficial in reducing energy consumption and forces, with attendant benefits to workpiece quality. In other instances, if any fracture were to lead to force oscillations as has been commonly assumed in segmented chip formation, then this has the potential to cause chatter vibrations with potentially adverse effects on quality. Keeping these factors in mind, we explore the microscopic mechanics of flow and fracture in segmented chip formation, and its relation to the forces and surface finish, with a view to answering these questions.

2.3 Estimation of Deformation Parameters—Particle Image Velocimetry (PIV)

The typical flow characterization methods employed—post-mortem analyses of grid deformation [16], [73] and microstructure markers [74], [75]—while useful for analyzing steady flow—lack the spatial and temporal resolution needed to map unsteady flow fields, flow dynamics and development of instabilities/fracture. *In situ* observations of the deformation using high-speed photography, in conjunction with image correlation, offer a direct way for quantitative analysis of

unsteady flow [76], [77] and the ductile fracture process. In the present study we rely on such *in situ* observations, coupled with the flow analysis conducted by Particle Image Velocimetry (PIV).

There are various image correlation techniques available to map velocity of material flow, displacements, and associated deformation fields. In this study, one of these techniques, Particle Image Velocimetry (PIV), is used to characterize the deformation field in machining. PIV has been used in fluid mechanics since the early 1980s to map the velocity field of fluid flows [78], [79]. In its basic form, it involves injecting tracers or particles into the fluid and tracking the motion of ensembles of these particles by digitizing high-speed images of the flow. In the present adaptation of the PIV method to study deformation fields in solids, the role of the particles is played by "asperities"—roughness features in the solid surface being imaged [18], [23], [80], [81]. The PIV-based methods yield displacement and velocity fields associated with material flow from which strain rate and strain tensors are estimated by spatial and temporal differentiation [18]. The spatial resolution of the PIV is ~ 1.5 um, enabling deformation fields, including in the immediate vicinity of tool/die interfaces, to be mapped over wide regions at high resolution.

A PIV-based measurement (digital PIV) of material flow is consisted of 2 steps: (1) recording the flow of material, in a sequence of images using a high-speed camera/imaging system. The imaged region and spatial resolution can be designed by using proper objective lenses and camera sensor size, while the temporal resolution of the recording relies on the camera speed; and (2) analyzing the images in pairs, selected from the image sequence, using image correlation techniques. Each image pair results in a frame of displacement vector field and a frame of velocity vector field, the latter being obtained by dividing the former by the time interval between the images in the pair. Thus, the outcome of the PIV analysis is a discretized sequence of displacement/velocity vector fields representing flow of the material over specific time durations;

in this manner, the flow is essentially discretized both in space and in time. If the spatial and temporal resolution is sufficiently high, then these displacement/velocity vector fields can approximate the complete material flow with sufficiently high accuracy.

The deformation parameters, strain, strain rate, and their principal directions, can be derived from the measured flow (velocity, displacement) information. The tensor components of strain increment during each time are obtained, according to the small strain definition, by differentiating the corresponding displacement vector [82]:

$$d\varepsilon_{xx} = \partial u/\partial x,\ d\varepsilon_{yy} = \partial v/\partial y,\ \ d\gamma = 2d\varepsilon_{xy} = \partial v/\partial x + \partial u/\partial y \qquad (2\text{-}4)$$

and the strain rate components at each point as

$$\dot{\varepsilon}_{xx} = \partial \dot{u}/\partial x,\ \dot{\varepsilon}_{yy} = \partial \dot{v}/\partial y,\ \ \dot{\gamma} = 2\dot{\varepsilon}_{xy} = \partial \dot{v}/\partial x + \partial \dot{u}/\partial y \qquad (2\text{-}5)$$

where u and v are components of the displacement vector in the x and y directions, respectively; ε_{xx} and ε_{yy} are the longitudinal strains and γ is the shear strain.

In this formulation the incremental strain and strain rate tensors at a point can be written in matrix form as

$$\begin{bmatrix} \frac{\partial u}{\partial x} & \frac{1}{2}\left(\frac{\partial u}{\partial y} + \frac{\partial v}{\partial x}\right) \\ \frac{1}{2}\left(\frac{\partial u}{\partial y} + \frac{\partial v}{\partial x}\right) & \frac{\partial v}{\partial y} \end{bmatrix} \text{ and } \begin{bmatrix} \frac{\partial \dot{u}}{\partial x} & \frac{1}{2}\left(\frac{\partial \dot{u}}{\partial y} + \frac{\partial \dot{v}}{\partial x}\right) \\ \frac{1}{2}\left(\frac{\partial \dot{u}}{\partial y} + \frac{\partial \dot{v}}{\partial x}\right) & \frac{\partial \dot{v}}{\partial y} \end{bmatrix}$$

To estimate the total plastic strain imposed along a deformation path, the strain increments will have to be ‘summed up’ in some suitable manner. In general, the accumulated strain tensor components at a point cannot be obtained by ‘summation’ as the principal direction of the incremental tensor components will vary with location along the deformation path. However, in plastic deformation, the strain increment components are related to the incremental effective strain $d\bar{\varepsilon}$ (assuming a von Mises yield criterion), as [83]:

$$d\bar{\varepsilon} = \sqrt{\frac{4}{9}\left(\frac{1}{2}\left[\left(d\varepsilon_{xx} - d\varepsilon_{yy}\right)^2 + d\varepsilon_{xx}{}^2 + d\varepsilon_{yy}{}^2\right] + \frac{3}{4}d\gamma^2\right)} \tag{2-6}$$

and effective strain rate as

$$\dot{\bar{\varepsilon}} = \sqrt{\frac{4}{9}\left(\frac{1}{2}\left[\left(\dot{\varepsilon}_{xx} - \dot{\varepsilon}_{yy}\right)^2 + \dot{\varepsilon}_{xx}{}^2 + \dot{\varepsilon}_{yy}{}^2\right] + \frac{3}{4}\dot{\gamma}^2\right)} \tag{2-7}$$

The total effective strain value at a point can then be estimated by summation of the individual effective strain increments along the deformation path up and until this point, or by integration of the effective strain rate along this path. It is this combination of effective strain and strain rate, both scalar parameters, which is commonly used to assess the level of plastic deformation that a material is subjected to in deformation processing. Furthermore, in conjunction with temperature, they determine the evolution of microstructure during the deformation. The components of the incremental strain tensor are, however, relevant for assessing evolution of crystallographic texture.

3. EXPERIMENTAL PROCEDURES OF CUTTING AND CHARACTERIZATION

Details of material selection, experimental setup, sample preparation and characterization methods are discussed in this chapter. The experimental cutting procedures to study segmentation can be classified into 2 groups: 1) Low-speed, plane-strain (2D) cutting, with high speed imaging and analysis of material flow and fracture, and 2) High-speed plunge turning (2D) on CNC lathe to study the chip segmentation at higher speeds. Furthermore, we use this framework to explore suppression of segmentation.

3.1 Material Selection

Plane-strain (2-D) machining experiments are carried out using a high-speed steel and carbide tools to cut commercially pure zinc, brass 260 (α-brass: 70% Cu – 30% Zn), brass 360 (2 phase: 60% Cu - 40% Zn), silicon steel (92% Fe, 4% Si, 4% Cr), oxygen-free high conductivity (OFHC) copper (99.99% Cu), Ti6Al4V, wrought magnesium alloy (AZ31B), and a low-melting point alloy (Woods metal). The selection of this wide range of material systems is to illustrate various features of flow dynamics related to fracture and segmented chip formation. Table 3-1 provides information about composition, initial state and hardness for these materials. The tools were made of commercial high-speed steel (HSS) and WC-Co alloy.

Several of the metal systems were selected because of their propensity for segmented chip formation at low-to-moderate speeds. We use a combination of *in situ* imaging, and *ex situ* analysis of material displacement (prow formation/pile-up) ahead of the tool, to estimate the strain just prior to segmentation, and various details of the flow dynamics. Suppression of segmented flow

is illustrated with brass, silicon steel and Zn. This suppression is critical for possible utilization of chip formation to produce metals in sheet and strip forms for applications.

To illustrate promotion of segmentation, another aspect of flow control, we utilize cutting of annealed Cu. Annealed copper is a very ductile metal that does not typically segment in cutting but instead undergoes sinuous material flow with large-amplitude folding. We show that even in this material it is possible to induce segmentation via local embrittlement with benefits to the cutting process in terms of energy, forces and surface quality.

To explore the interaction between microstructure and flow dynamics, we use cutting of thermally etched copper and Ti6Al4V, in conjunction with *in situ* imaging.

The relevant nominal properties of the model work material systems are given in Table 3-1. The work materials are subjected to varying deformation conditions by varying the tool rake angle (strain) and cutting speed (strain rate).

Table 3-1. Nominal properties of the model work material systems

Material	Composition	Condition	Hardness
Commercially pure zinc	99.95% Zn	Cold Rolled	30 HV
Brass 260	70% Cu, 30% Zn	1/4 Hard	50 HRB (equivalent with 92 HV)
Brass 360	60% Cu, 40% Zn	1/2 Hard	78 HRB (equivalent with 144 HV)
Silicon Steel	92.0% Fe, 4.0% Si, 4.0% Cr	Hot forged	200 HV - 240 HV
OFHC copper	99.99% Cu	Annealed	40 HV
Ti6Al4V	90% Ti, 6% Al, 4% V, (less than 0.3% Fe, 0.2% O, and 0.1% C)	Annealed	36 HRC (equivalent with 342 HV)
Magnesium AZ31B	96% Mg, 3.0% Al, 0.7% Zn, 0.3% Mn	Cold rolled	49 HB (500 gm load) (equivalent with 41 HV)
Woods metal	50% Bi, 26.7% Pb, 13.3% Sn, 10% Cd	As cast	9 HB (500 gm load) (below the acceptable range for HV hardness)

3.2 Experimental Setup

Tool rake angle and cutting speed were the principal parameters varied to change the deformation conditions in chip formation. The cutting speed V_0 was varied between 1 mm/s to 6000 mm/s. The low speed plane-strain machining was carried out using a linear machining arrangement (Figure 3-1), where the workpiece in the form of a plate, 50–100 mm length × 20–30 mm height × 3–5 mm width, was moved with respect to the cutting tool. A HSS tool (unless otherwise noted) was used, with the cutting being carried out on the 50–100 mm × 3–5 mm face of the workpiece. The edge radius of the tool in all cases was smaller than 5 μm (unless otherwise noted). During the cutting, the tool was held stationary in a holder while the workpiece is moved by a linear slide. The rake angle was varied by using tool bits ground with different geometries. The undeformed chip thickness, t_0, see Fig. 2-1, was set to desired values (typically in range of 50 μm to 300 μm) by adjusting the tool position in the vertical direction. This thickness was also directly measured by checking the depth of material removed from the recorded image sequence (*in situ* high speed imaging). The cutting width (w) into the plane in all cases was much greater than t_0 (20–50 times), thereby ensuring a plane strain deformation condition. A 3-component piezoelectric dynamometer (Kistler) was incorporated into this setup on the tool side to measure the main cutting force (power component, parallel to V_0), and the thrust force perpendicular to V_0. The low speed cutting experiments were done using Mobil 1 Advanced Full Synthetic Motor Oil 5W-30 as lubricant.

Cutting experiments at higher V_0 (> 20 mm/s) were conducted using disc samples (3–50 mm width × 50–200 mm diameter) in a plunge rotary-machining configuration on a CNC lathe (Haas lathe for smaller chip width samples, and an Okuma lathe for the larger chip width samples). Here, the cutting tool made of WC-Co alloy (unless otherwise noted) was plunged radially into the

disc at the rate of t_0 per revolution; note that in this configuration, t_0 is again the undeformed chip thickness. Plane strain conditions were ensured by keeping the workpiece width w (3–5 mm, disc thickness) >> t_0 (Figure 3-1b). Forces were measured using a 3-component piezoelectric (Kistler) dynamometer coupled to the tool-holder.

It is straightforward to see from Fig. 3-1 that the geometry of cutting in both the linear and rotary configurations is essentially the same.

Material flow and deformation measurements were made via *in situ* imaging of the chip formation, and PIV analysis, in the low-speed linear cutting. For these deformation measurements, one (50–100 mm × 20–30 mm) side of the workpiece was imaged during the cutting using a high-speed CCD-based imaging system coupled to an optical microscope assembly. A transparent glass plate (Figure 3-1c) was used to constrain this side of the workpiece during the cutting so as to minimize side (lateral or out-of-plane) flow of material in the deformation zone, ensuring plane-strain. The glass constraint also helps with better alignment of the side faces of the tool and workpiece (being imaged), that is they lie in the same plane, enabling proper focusing of the camera onto the deformation zone. The imaged side of the workpiece was abraded with 600 grit abrasive paper to create a set of asperities (speckle pattern) for the image correlation analysis. The PIV analysis was applied to a sequence of high-speed images captured by the camera. From this analysis, effective (von Mises) strain and strain rate fields, velocity of material flow and flow lines were derived. This provided both quantitative and phenomenological information including about onset of fracture, crack propagation etc.

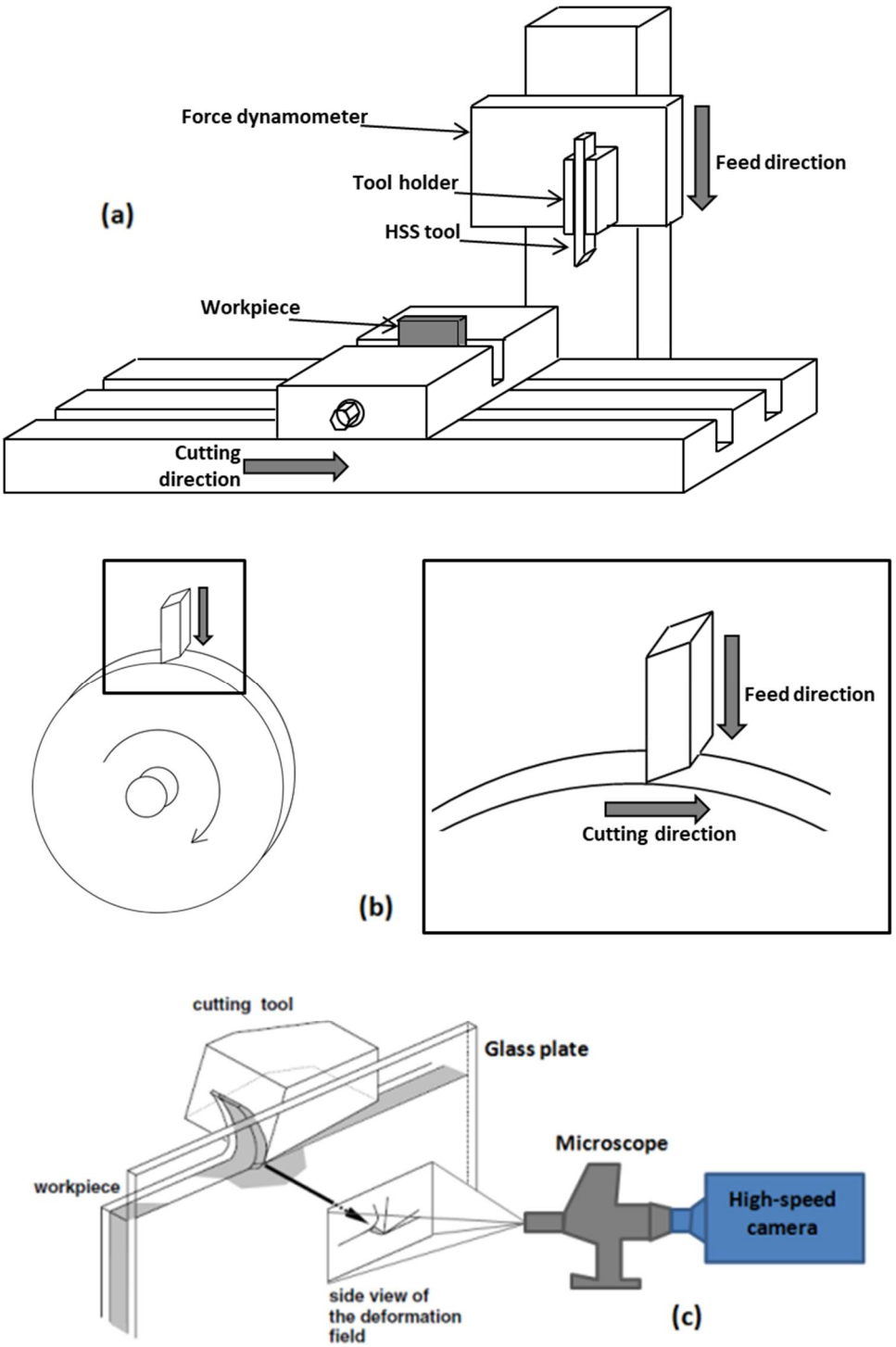

Figure 3-1. Schematic of (a) linear machining setup used at low-speeds, (b) rotary plunge turning (cutting) system used at the higher cutting-speeds, and (c) high speed imaging system configuration used to map the material flow and deformation. The local geometry of the cutting in both the linear and rotary configurations is essentially the same as in Figure 2-1, i.e. plane strain cutting.

3.3 Sample Preparation and Characterization Methods

To study microstructural origins of segmented flow, a set of experiments on thermally etched (fully annealed) copper samples and Ti6Al4V samples were performed. As will be seen, in these experiments, especially with the Cu, segmentation was promoted locally through a mechanochemical effect, using Sharpie permanent marker ink painted onto the workpiece surface being cut. Details of the segmentation process were obtained by *in situ* imaging. The thermal etching made visible, the grain scale microstructure of sample for the direct *in situ* observations. Details of thermal etching process are given in the Appendix B.

A Kistler 3-component piezoelectric dynamometer (Kistler Model 9254 dynamometer) was used for the cutting force measurements. The natural frequency of the dynamometer was ~ 2000 Hz. The dynamometer settings were suitably set to measure force traces up to a frequency of 1000 Hz.

Ex situ optical microscopy and metallography of the workpiece and chip samples were done by polishing the samples with SiC (down to 1200 grit size) and diamond (down to 1 μm) abrasives, followed by further polishing in colloidal silica. Electron microscopy was done with FEI XL-40 scanning electron microscope at 20kV accelerating voltage (unless otherwise noted) after cleaning (ethanol followed by isopropyl alcohol) and air drying of the samples. These microscope observations provided details of chip morphology, workpiece surface macro defects, and fracture and flow patterns.

Post-cutting surface topography characterization of workpiece (WP) surface was done by stylus profilometry (Form Talysurf 50) and optical profilometry (Zygo NewView 8000). Zygo NewView 8300 is a large-area 3D optical profilometer which enables 3-dimensional (3D) study of surface with analytical representations in the form of surface and line profiles. This provided

details about surface quality of the cut surface and parameter effects (e.g., segmentation vs no-segmentation etc)

The hardness values for chip and workpiece surface were measured utilizing indentation methods (Brinell, Rockwell, Vickers), depending on the material system. Samples where mounted and polished, where necessary, with abrasives down to 1 μm diamond before the indentation.

4. MECHANISM OF SEGMENTATION

The PIV analysis has been used to characterize the nature of material flow in segmented chip formation and obtain strain and strain rate data in the deformation zone, workpiece (WP) surface and chip. This data points is presented and analyzed, together with force and roughness. We use this analysis to obtain a description of the mechanics of segmentation.

4.1 Flow Dynamics in Segmentation

The *in situ* observations have provided critical details about segmented flow mechanics, in particular that segmentation is initiated by a crack from the chip back-surface. Figure 4-1 shows selected frames from a high-speed image sequence of cutting of Zn (α = -40°), highlighting how a flow instability triggers chip segmentation. A prow of material first develops ahead of the tool, constituting the base of the chip (frame 1). This prow is inclined at angle θ to the WP free surface (horizontal orange line). But the flow is unsteady and the prow unstable, as seen in the sequence. This prow can be idealized as forming by shearing of surface elements, the shear occurring along planes inclined at 45° to the surface [5], [17]. A crack then initiates on the prow surface (red arrow, frame 1), i.e., chip back-surface, and propagates some distance towards the tool tip (frames 1 to 4); this prow-crack formation triggers a flow instability which is the nucleation phase of segmentation flow. The (critical) prow angle θ^* when the crack forms is ~ 40° (frame 1).

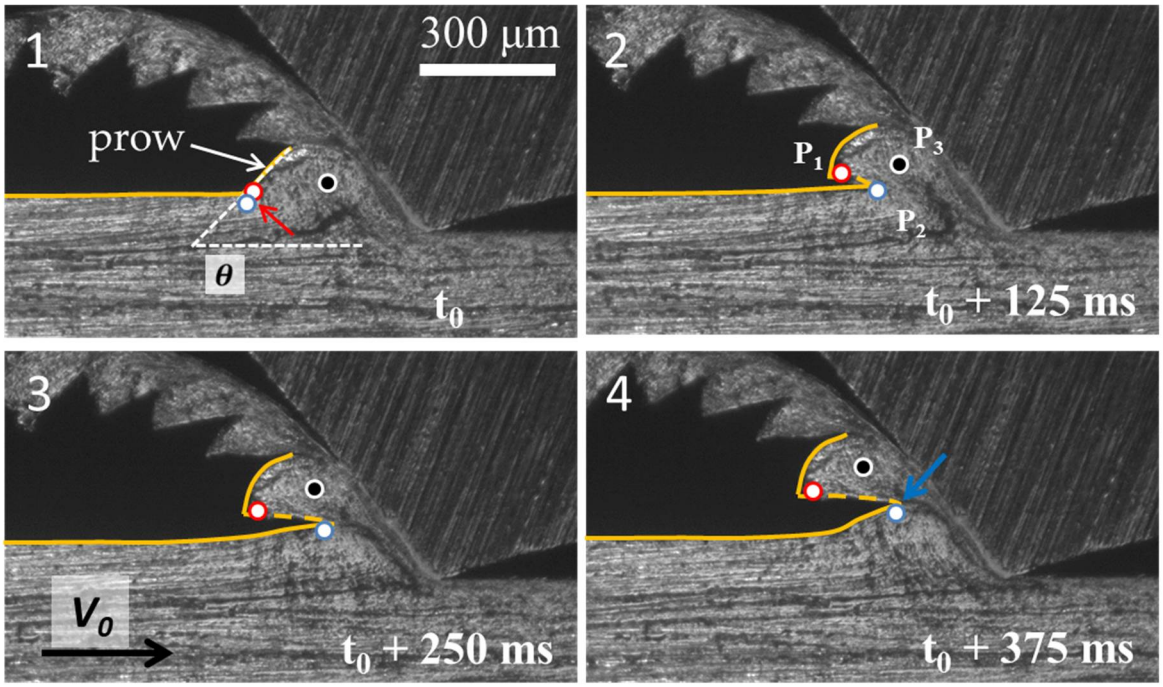

Figure 4-1. Four select frames from a high-speed image sequence showing segmentation and associated flow dynamics in cutting of Zn. The segmentation occurs due to a crack initiating (red arrow) in the prow which forms ahead of the tool. The prow is inclined at angle θ to the (horizontal) workpiece surface. The segmentation develops by propagation of the free-surface crack towards the tool tip (blue arrow). α = -40°, V_0 = 1 mm/s, t_0 = 100 μm.

To analyze crack propagation and flow development, different points in the deformation/prow region were tracked using PIV. The motion of three points P1, P2 and P3 (frame 2) is used to describe the segmentation. P1, P2 are initially located very close to each other, and on either side of an incipient crack tip. Subsequent crack growth increases the separation between P1 and P2 (frames 2–4). In Figure 4-1, the crack is arrested approximately half way between the chip back-surface and tool tip (blue arrow in frame 4).

The segmentation is also tracked via strain-rate mapping as shown in Figure 4-2 for α = -40°. Again, the initiation of the crack is at the chip free (back) surface. The crack propagation direction is aligned parallel with the deformation zone, which is the region of high strain rate. Frame 1 displays the final stage of crack propagation for a particular segment. At this point, the

crack-tip driving force is reduced, frame 2, and a new prow and crack develop, frame 3, and the process repeats cyclically.

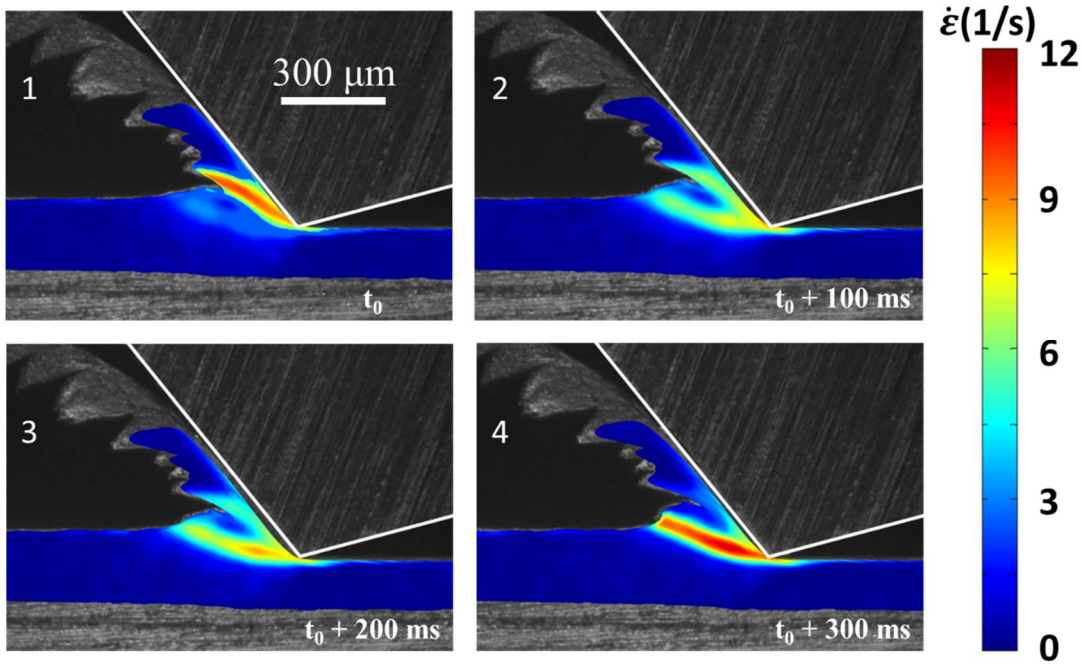

Figure 4-2. Evolution of strain rate field and its relation to the segmentation in cutting of zinc. α = -40°, V_0 = 1 mm/s, t_0 = 100 μm.

This segmented flow with prow-crack propagation from the chip free surface was observed for all α between -60° and -10°. The crack propagation, however, extended closer to the tool tip as α was made more negative. Figure 4-3 shows selected frames from image sequence of cutting of Zn with tool rake angle α = -20°. The extent of the segmentation (blue arrow) is much less here, highlighting the decreased segmentation at less negative α.

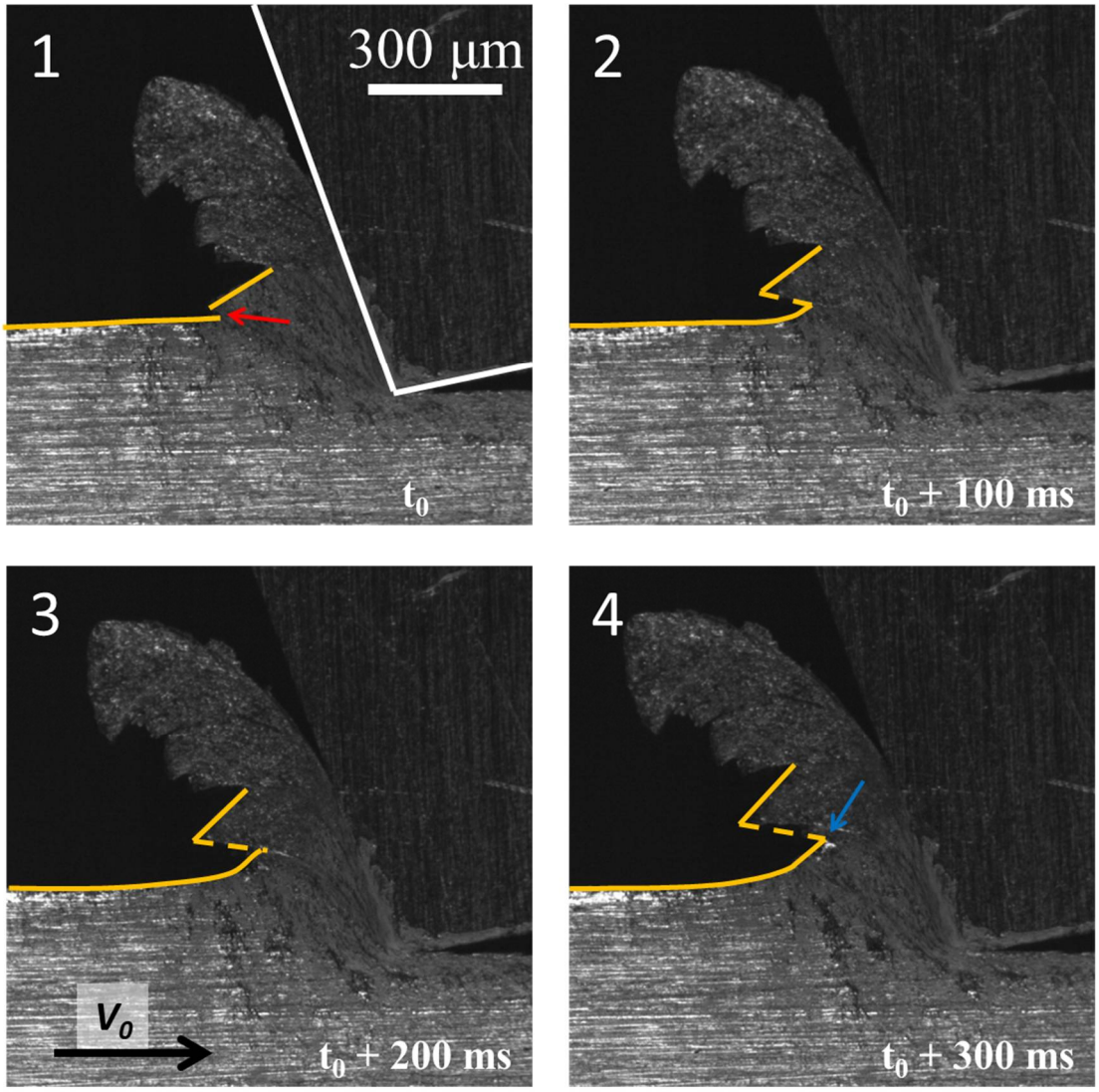

Figure 4-3. Four frames from a high-speed image sequence showing segmentation and material flow in cutting of zinc. The red arrow points to crack initiation location. The blue arrow shows crack growth front. This sequence is similar to Figure 4-1 except that the rake angle is less negative (i.e., more positive). α = -20°, V_0 = 1 mm/s, t_0 = 150 μm.

The dependence of chip formation and segmentation on α is summarized in Figure 4-4. Segmentation is more pronounced at larger negative α, but does not occur at positive α . Besides illustrating the increasing segmentation with decreasing α, the summary also shows that for α > 0°, the chip formation is continuous without segmentation and the flow laminar. Furthermore, at large negative α, e.g., α = -70° (Fig. 4-4(e)), chip formation ceases to occur, and the process

changes to asperity sliding without material removal. At this condition, the workpiece material piles up ahead of the indenter forming a prow. This prow is stable, with a small steady growth in its size with increasing sliding. For $\alpha > 0°$ the flow was mostly laminar, Figure 4-4(a), with a continuous smooth chip (free) surface at the mesoscale. The deformation zone at the positive rake angle conditions resembles that of the shear plane model [3], similar to Figure 1-1c. The average strain in the chip for $\alpha = 30°$ is 0.65 ± 0.04, while the strain on the newly created surface is much smaller. In some $\alpha \geq 0°$ cases, there was prow-crack formation, but these cracks were arrested very soon after initiation, resulting in small-scale waviness on chip back-surface similar to the case of α = -20° (Figure 4-3). These observations suggest that the fine-scale roughness observed on the chip back (free) surface in typical machining operations, usually done with $\alpha \geq 0°$, is all due to segmentation events that get arrested very soon after they are initiated.

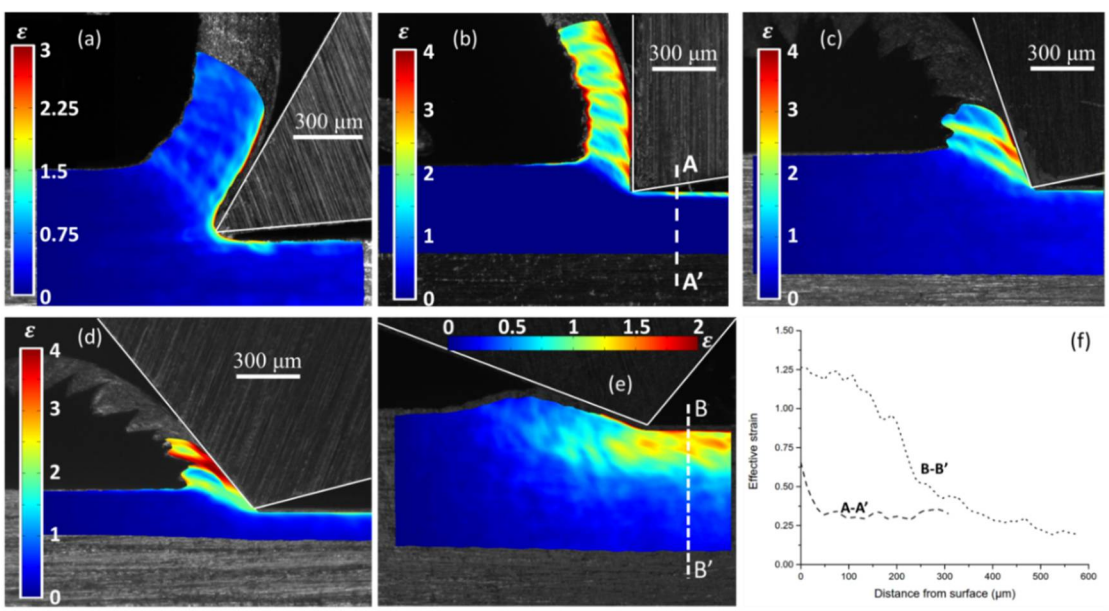

Figure 4-4. Dependence of the effective strain field and segmentation on rake angle α in cutting of Zn. (a) α = +30°, (b) α = 0°, (c) α = -20°, (d) α = -40°, (e) α = -70°. The strain distribution with depth into the workpiece in the wake of the tool is shown in (f) for 2 cases α = 0° (cutting) and α = -70° (pure sliding). V_0 = 1 mm/s.

The average speed of the crack propagating from the free surface of the chip, as estimated from the high-speed image sequences, was 0.9 mm/sec, for α = -40° (frames 1–3 in Figure 4-2). This speed is close to the loading rate V_0 = 1 mm/s. This is analogous to shear-band flow, wherein the band propagation speed ~V_0 [12]. A similar evolution of segmented flow has also been observed in cutting of H02 brass 260 [17].

It is obvious by comparing Figure 4-4(a) (continuous chip) with Figures 4-4(b), 4-4(c) and 4-4(d) (segmented chip) that strain fluctuation (or strain heterogeneity) is a key feature of segmentation. For example, for α = 0°, the chip strain varies between 0.5 and 2.5, with a volume averaged strain of 1.58 ± 0.05 in the chip. The bands of high strain are aligned with the line of crack propagation, and orientation of the shear plane. These bands of high strain are thicker for the more negative rake angle, see for example for α = -40° in Figure 4-4(d). The thickness and orientation of a high strain band has some correlation with the duration and alignment of each active shear plane that is developed during the cutting. This can be explained using the strain rate field shown in Figure 4-2. The sequence of 4 frames here depicts formation of a segment under the influence of an active shear zone, while a prow is growing, frame 1. When a new prow is fully developed, the previous shear plane (zone) decreases in strength while a new shear zone is activated and strengthening (frames 2 and 3). After the prow formation is complete and the prow passes into the chip, the deformation is concentrated in the new shear zone while the previous shear zone becomes inactive. The process of activation and deactivation of consecutive shear zones is the cause of the bands of high and low strain in the chip. The duration for which a shear zone remains active influences the thickness of the high band strain region.

The strain on the residual cut surface of the workpiece behind the tool was also mapped using the PIV analysis. Generally, this cut surface strain is lower for segmented chip formation

than for case of sliding without material removal. This can be seen in the strain profile with depth into the workpiece surface shown in Fig. 4-4(f) for α = 0° and α = -70°. While the strain for the sliding case (α = -70°) remains higher than 0.75 until a depth of 200μm into the sample, for α = 0° (segmented cutting case), this strain is ~ 0.6 at the surface and reduces to 0.3 after a depth of only 50μm into the substrate. Also, the cut surface does not appear to show any strain variations along its length in contrast to the chip even when the segmentation is quite pronounced.

The present direct observations suggest that segmented (saw-tooth) chip formation is initiated by a ductile failure originating on the chip back-surface in the form of a crack that then propagates towards the tool tip at a speed $\sim V_0$. The direct observations thus confirm earlier inferences about where the segmentation failure nucleates [5], [16], [46].

4.2 Segmentation in Cutting of Brass and Silicon Steel

The details of the segmentation – fracture initiation, propagation etc. - were explored also in brass 360, brass 260, and silicon steel.

4.2.1 Brass 360

It was in cutting of two-phase brass 360 at low speeds that Nakayama [5] had first observed the formation of a segmented chip, and documented details about the fracture-driven segmentation. A picture of this segmentation is shown in Figure 4-5 [39]. Based on analysis of such micrographs, Shaw [13], [39] derived relations for typical metal cutting process variables, including the chip thickness ratio (λ), chip strain (ε), shear angle (φ) and specific energy(u). For example, the cutting ratio (λ), which is the ratio of mean chip thickness (t_c) to the undeformed chip thickness (t_0), was shown to be:

$$\lambda = \frac{t_c}{t_0} = \frac{V_0}{V_c} = \frac{p}{p_c} \tag{4-1}$$

where p and p_c refer to morphological details (amplitude, pitch) of the chip segment that can be measured from a post-mortem examination of the chip (Fig. 4-5).

Similarly, through the analysis of hodograph of the shear bands, it is shown that the shear angle φ may be obtained from

$$\lambda = \frac{\cos(\alpha+\varphi)}{\sin(\varphi)} \tag{4-2}$$

This formula for strain assumes still homogeneous deformation (laminar flow) with a shear plane approximation to the deformation zone. The only difference from the laminar flow case is that λ is now calculated using Equation 4-1. Clearly the results with Zn earlier show that homogeneous deformation is not the norm with segmented chip formation.

Key deformation and energy parameters of the cutting process for the case of the segmented chip could thus be obtained from post-mortem observations of the chip. Alternatively, *in situ* observations may also be used to estimate these parameters as is done here.

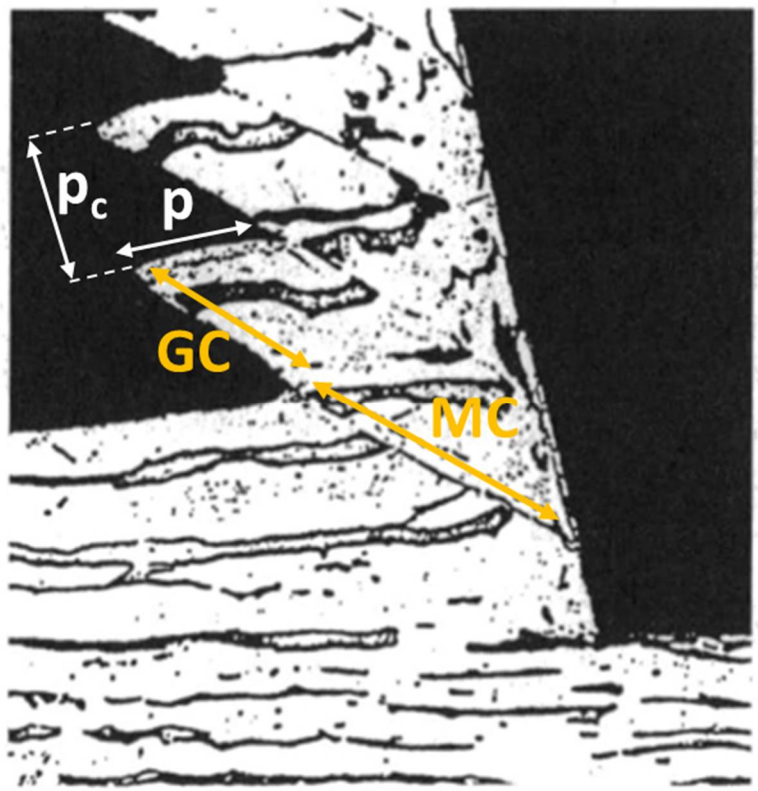

Figure 4-5. Saw-tooth or segmented chip in low speed turning of brass 360 with negative rake angle tool. α = -15°, V_0 = 1.25 mm/s, t_0 = 160 μm (from Ref. [39]). In the analysis presented by Shaw [13], [39] on the mechanics of fracture driven segmentation, segmented chip is divided to two areas of gross crack (GC) and microcracks (MC).

Nakayama and Shaw both inferred that the segmentation process in cutting of brass 360 is initiated by a crack that nucleates at the free surface of the chip in the shear zone. It is worthwhile to re-examine this claim through our high speed *in situ* imaging.

Figure 4-6 shows 4 frames from a high-speed image sequence from cutting of brass 360 (half-hard) with α = 0°. As in the case of Zn, segmented chip formation is observed to occur, driven by nucleation of a crack (red arrow, frame 1-2) on the back surface of the chip and its propagation towards the tool tip (blue arrow, frames 3-4). Note that the crack initiates in the prow region; the slope of the prow is shown by dotted line. As the crack propagates towards the tool tip and the extent of the segmentation grows, the chip moves with speed V_c relative to the tool (frame

3) and with speed V_s relative to the workpiece (frame 4). The average crack speed is 7.0 mm/s which is close to the cutting speed $V_0 = 6$ mm/s. This crack growth is somewhat faster than in the case of Zn where the crack speed was ~ V_0. Secondary microcracks are also seen in brass 360, initiating at the tool tip along the rake face, see frame 1 and frame 4 at orange arrow. In this document, we use the term microcracking to describe cracking from the tool tip side. These cracks however do not propagate any significant distance into the chip in cutting of brass 360. They certainly do not play a role in the segmentation process, even though their initiation often occurs before the (surface) macrocrack initiation. The microcracks do leave behind residual markings on the workpiece cut surface in the form of high and low points, see white circles in Fig. 4-6.

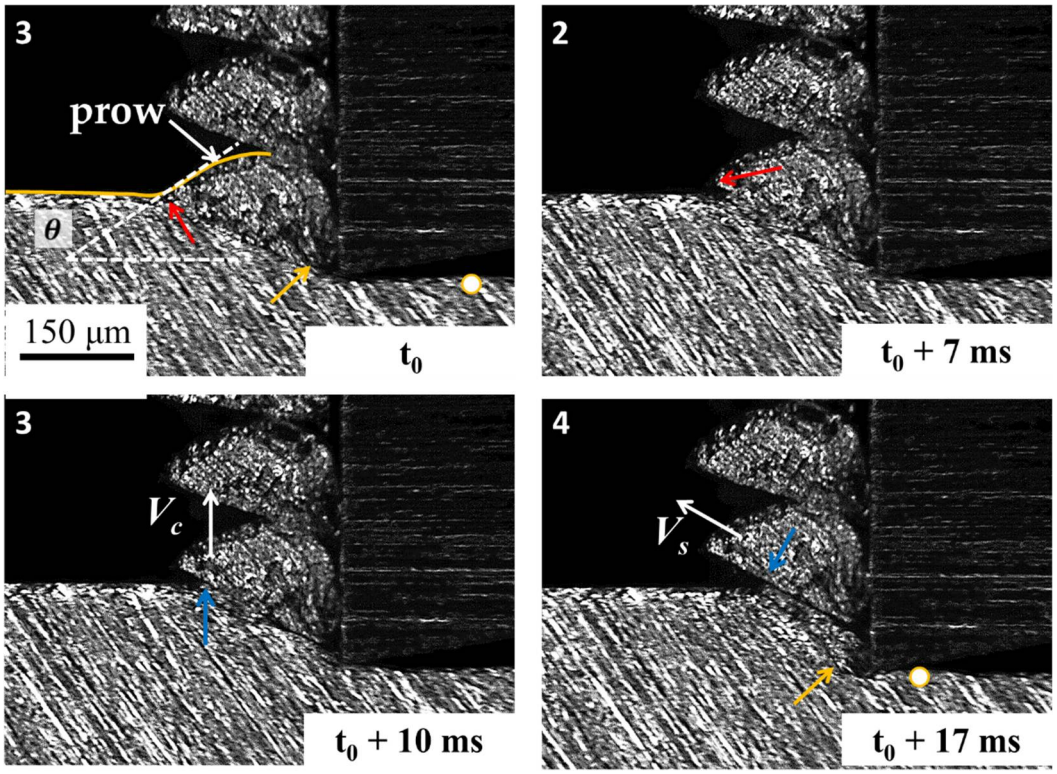

Figure 4-6. Four frames from a high-speed image sequence showing macro-crack initiation from chip free surface (red arrow, frame 1-2) that drives the segmentation in cutting of brass 360. The development of the segmentation, from this crack, is seen at blue arrows in frame 3-4. The evolution of the segment formation is due to propagation of this macro-crack towards the tool tip. The prow slope is demarcated by dotted line. An additional feature here is occurrence of secondary microcracks close to the tool tip along the rake face of the tool (orange arrows). These microcracks (cracking from the tool tip side) leave behind residual high and low points on the cut surface of the workpiece (white circles). $\alpha = 0°$, $V_0 = 6$ mm/s, $t_0 = 120$ μm.

A similar segmentation process (evolution) was also seen when cutting with a positive rake angle $\alpha = +20°$. The imaging results are shown in Figure 4-7; they are very much analogous to Figure 4-6. Frame 1 shows formation of microcracks near the tool tip (orange arrow). But as is clear from frames 3 and 4, the microcracks after forming are carried along the rake face without contributing to formation of the chip segments. Frame 3 shows the segmentation beginning with formation of a macrocrack crack on the chip free surface (red arrow). As this segment develops with the macrocrack propagating towards the tool tip (blue arrow in frame 4), the deformation is

confined to this surface crack region. The microcrack region stays inactive. As shown in frame 4, development of a new segment is only possible with rigid body movement of the current chip segment along the rake face of tool. A new cycle of segmentation then will initiate. The average macro-crack speed is 5.5 mm/s which is close to V_0 = 6 mm/s. Also, it is noteworthy that at this positive rake angle, no high/low points occur on the workpiece cut surface due to the microcracks. Importantly, the key observation from Figure 4-7 is that segmentation development again occurs from the chip back surface and is not linked to the microcracks at the tool tip. The *in situ* observations support the inferences of Nakayama and Shaw that the segmentation is tied to ductile fracture initiating quasi-periodically at the chip free surface.

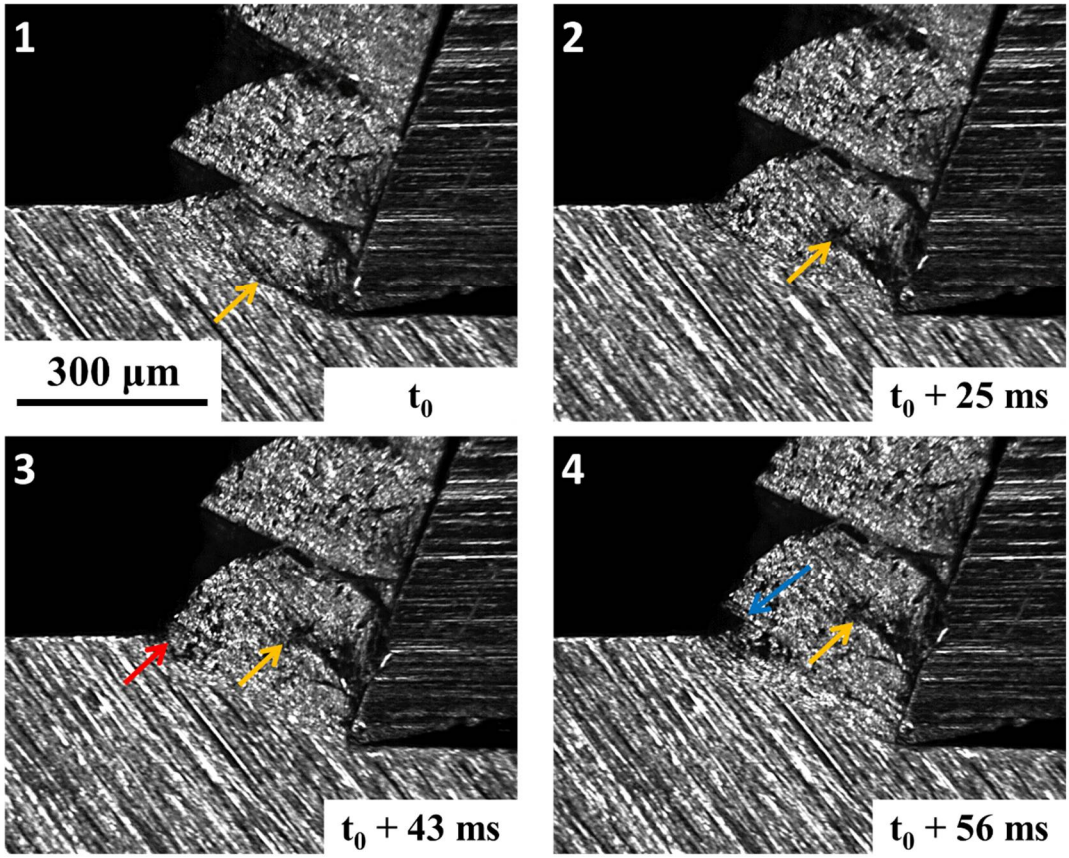

Figure 4-7. Four frames from a high-speed image sequence showing microcrack initiation from rake face of the tool (orange arrow) and crack initiation from free surface (red arrow) which results in segment formation (blue arrow) in cutting of brass 360. α = +20°, V_0 = 6 mm/s, t_0 = 150 µm.

The strain and strain rate field for cutting of brass 360, derived from the PIV analysis for α = 0° and α = +20°, are shown in figure 4-8. For α = 0°, the chip strain varies between 0.5 and 3.5, indicating significant strain heterogeneity due to the segmentation. The corresponding volume averaged strain in the chip is 1.6 ± 0.08. For α = +20°, the chip strain varies between 0.3 and 3.0, with average value of 1.1 ± 0.05. The bands of high strain are somewhat thicker for α = 0°. The microcrack region is shown by orange arrow and free surface crack by red arrow in the strain field plots. It is clear from the strain rate fields that the crack propagation from the free surface, which

drives the segmentation, is oriented parallel to the deformation (shear zone), similar to Zn. Note that the shear zone can be identified with the region of high strain rate in the figure.

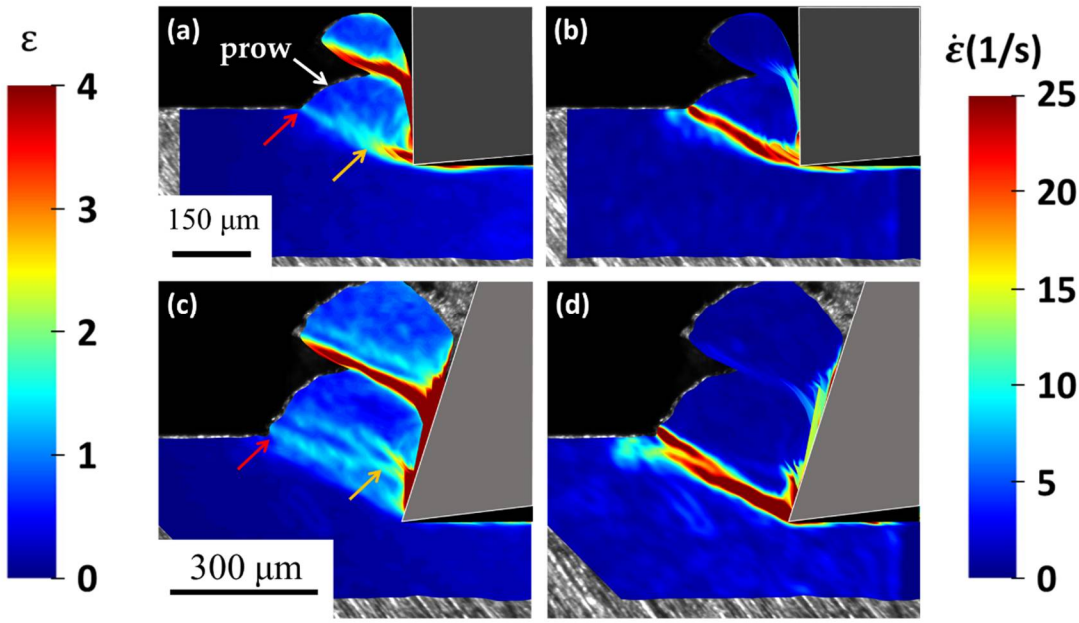

Figure 4-8. Strain (left) and strain rate (right) field for cutting of brass 360. (a) and (b) α = 0°; (c) and (d) α = +20°. In each case, the strain field is on the left and the strain rate field is on the right. Frames selected from the same cutting experiments shown in figures 4-6 and 4-7.

4.2.2 Brass 260

The segmentation mechanics was also explored with single-phase brass 260 (quarter-hard), a system in which segmentation was studied for an initial half-hard workpiece condition by Guo et al. [17]. Figure 4-9 shows 4 frames from high-speed image sequence of cutting of brass 260 with tool of rake angle α = 0° and α = -30°. The onset of crack initiation in prow region is seen in part (a) and (c) at red arrow. The propagation of the crack towards the tool tip (and segmentation) is shown in part (b) and (d) at blue arrow (crack tip). Similar to Figure 4-1 and Figure 4-3 (zinc), but unlike the case of brass 360, there was no microcracked region observed near the tool tip. The segmentation is, thus, again clearly a result of crack nucleation on the prow surface (chip free surface) and its propagation inwards towards the tool tip. Crack growth rate for α = 0° is 3.1 mm/s

while it is 1.4 mm/s for α = -30°. Experimental cutting speed was V_0 = 4 mm/s and V_0 = 2 mm/s for α = 0° and α = -30°, respectively. Consequently, the crack growth speed is 20% to 30% slower than V_0 in cutting of H04 brass 260. Furthermore, the segmentation traverses a longer portion of chip thickness for a more negative rake angle, similar to zinc. Similar results were reported with the brass 260 half-hard by Guo et al [17].

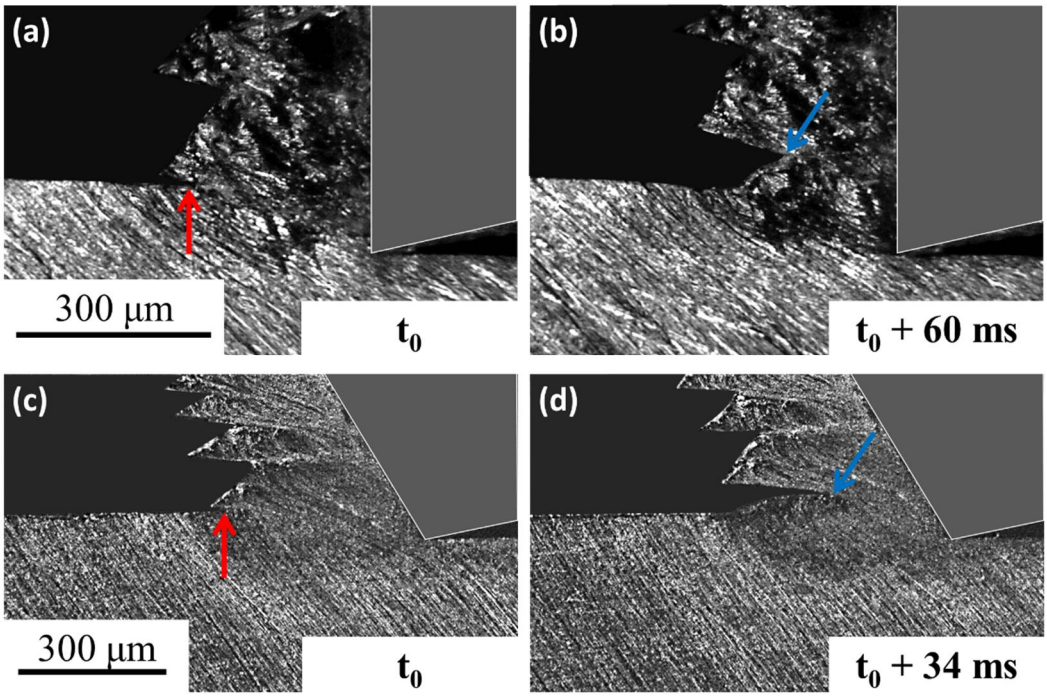

Figure 4-9. Frames from high-speed image sequence showing crack initiation from free surface (red arrow) which results in segment formation. The blue arrow shows the crack tip after it has propagated part way into the chip. Brass 260, (a) and (b) α = 0°, V_0 = 4 mm/s, t_0 = 100 μm, (c) and (d) α = -30°, V_0 = 2 mm/s, t_0 = 60 μm.

Strain and strain rate field for cutting of brass 260 with rake angle α = 0° and α = -30° is shown in figure 4-10. The chip strain ranges from 0.5 to 4.1, and 1.5 to 4.8 for α = 0° and α = -30°, respectively. This gives an averaged strain of 2.0 ± 0.1 in the chip for α = 0°. For α = -30°, the averaged strain is 3.2 ± 0.1. As expected, average strain as well as strain limits are larger for

α = -30°. Strain rate field in the shear region is stronger for α = 0°, but it is due to faster cutting speed, V_0 = 4 mm/s.

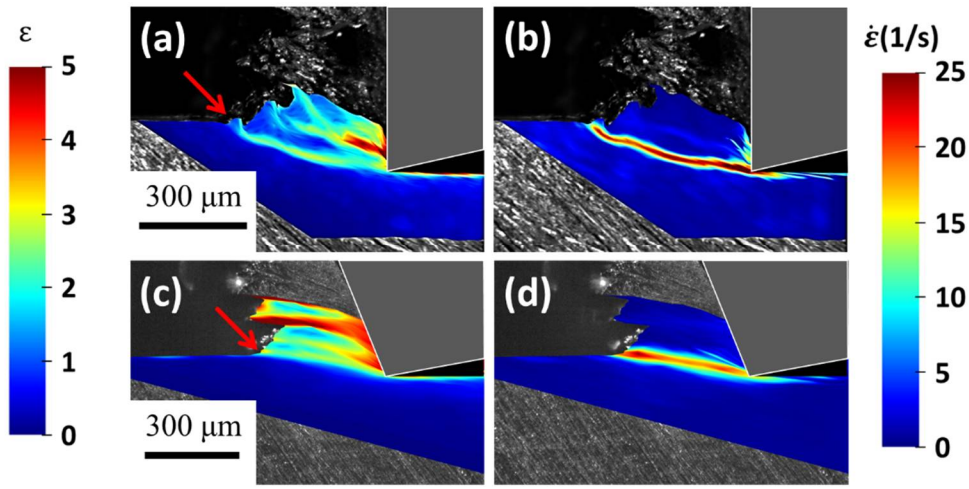

Figure 4-10. Strain and strain rate field for cutting of brass 260 with (a) and (b) a tool of rake angle α = 0°, (c) and (d) a tool of rake angle α = -30°. In each case, the strain field is on the left and the strain rate field is on the right. The red arrow shows the crack initiation point. Frames selected from the same cutting experiments shown in figure 4-9.

4.2.3 Silicon Steel

Another material system of interest is silicon steel with many applications in electric motors [4] and soft magnetic materials market [85]. Four frames of segmentation development for cutting of silicon steel at a rake angle of α = +10° is shown in figure 4-11. Due to higher hardness of workpiece material a carbide tool is used for linear cutting experiment. Frame 1 show prow formation. Frame 2 shows onset of crack initiation (red arrow) at the free surface of workpiece ahead of the tool. No microcracked region is formed. Frame 3 depicts growth of crack (blue arrow) and formation of segmented chip. Rigid motion of chip with a velocity of V_c along rake face of tool and fully developed segmentation is shown in frame 4. The average crack speed is 3.2 mm/s which is close to cutting speed V_0 = 3 mm/s. The crack nucleation and growth follow similar pattern to that of brass 260 and zinc.

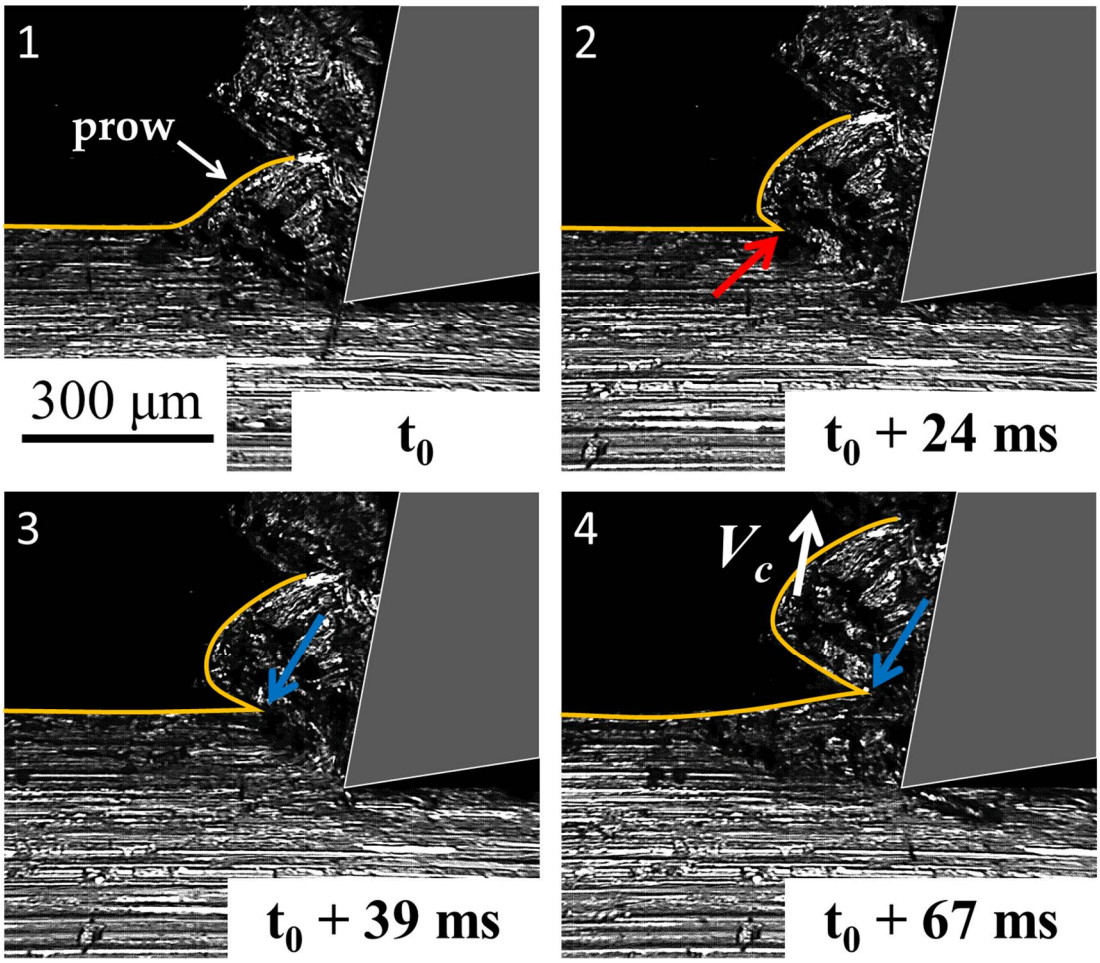

Figure 4-11. Four frames from a high-speed image sequence showing crack initiation from free surface (red arrow) followed by crack growth (blue arrow) in cutting of silicon steel. α = +10°, V_0 = 3 mm/s, t_0 = 120 μm.

4.3 Fracture Initiation in Prow

The direct *in situ* observations have shown that a prow or pile-up of material forms ahead of the advancing tool in the deformation zone. Figure 4-12(a) shows a picture of this prow in Zn. As we have already observed, the segmentation in Zn, brass 260, brass 360 and Si steel, is triggered by the nucleation of a crack in the prow region close to where the chip back surface intersects the workpiece surface ahead of the tool. A schematic of the prow region and segmented chip is given in Fig. 4-12(b); this is analogous to the *in situ* picture of Fig. 4-12(a).

The formation of the prow due to material pile-up can be idealized as occurring by shearing of workpiece (WP) surface elements (Figure 4-12(b)) along planes inclined at 45° to the WP surface [5]. Based on this model, Nakayama showed that θ provides a direct measure of the surface (shear) strain in the prow. For each incremental shearing step ($\delta\theta$) leading to the prow formation, the corresponding incremental shear strain imposed on workpiece surface (prow) elements is:

$$\delta\gamma = \tan\left(\frac{\pi}{4}\right) - \tan\left(\frac{\pi}{4} - \delta\theta\right) \approx 2\delta\theta \qquad (4\text{-}3)$$

where θ is the angle of inclination of the prow surface with respect to the direction of V_0, and $\delta\theta$ is change in that angle. Then by integrating the incremental shear strain along the path of deforming material elements at the workpiece surface, we get the total shear strain on the prow (surface) as:

$$\gamma = \int \delta\gamma = \int 2\delta\theta = 2\theta \qquad (4\text{-}4)$$

If the surface crack triggering the segmentation occurs at a critical angle θ^*, then from measurement of this angle we can get the shear strain at crack nucleation as

$$\gamma^* = \int \delta\gamma = \int 2\delta\theta = 2\theta^* \qquad (4\text{-}4)$$

A similar expression for the shear strain has been arrived at by Okushima [16] who assumed chip formation to occur across a shear zone of finite width, rather than a shear plane.

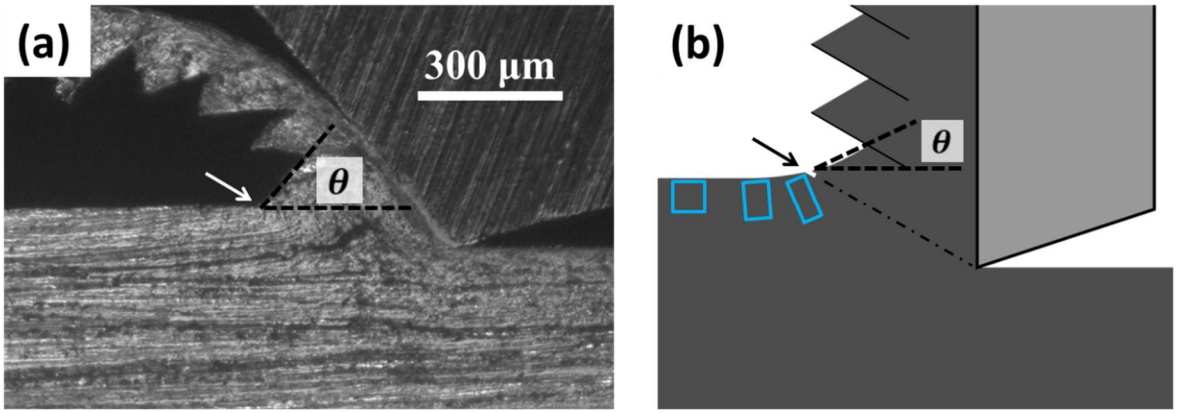

Figure 4-12. (a) The nucleation of crack on the workpiece-chip surface in the prow region causing the segmentation in cutting of Zn. (b) Schematic of prow formation by shearing of surface elements as suggested by Nakayama [5]

The total shear strain on the prow surface due to the pile-up is hence 2θ (θ in radians) and the corresponding von Mises effective strain (ε) (for plane strain) is $2\theta/\sqrt{3}$. Hence, $\varepsilon^* = 2\theta^*/\sqrt{3}$ is the strain at prow-crack initiation, where θ^* is the prow angle at crack initiation. That this is a good estimate of ε^*, has been established by comparison with direct strain measurements made using the PIV analysis in prior work with brass 260 [17]. In the ensuing, we use direct measurements of θ^* from the imaging to estimate ε^* at the prow-crack initiation point. These are then also compared with direct measurements of ε^* made via the PIV analysis of the high-speed image sequences.

Figure 4-13 shows the variation of prow-angle at crack initiation, θ^*, with α, for Zn, and the strain as estimated from the angle (black points). The right-hand strain axis is scaled according to the Nakayama's angle-strain equation (Equation 4-4). The ε^* values at prow crack initiation, and leading to segmentation, as measured by the PIV are shown in red (Note: Appendix C describes measurement of strain, with details, using PIV in the prow region. This is done by integration of incremental strain along material flow path lines). The plot shows the relative constancy of θ^* (~ 37°, dotted line) and, by extension, ε (~ 0.75) at prow crack initiation, for α

between -60° and -10° (segmented-flow). This θ^* and strain constancy has been previously observed in segmented chip formation with brass 260 [17]. The observations suggest that prow-crack formation is governed by a critical strain criterion, this critical strain value being relatively independent of deformation geometry (α). That segmentation occurs at constant strain in the cutting-deformation geometry is consistent with the simplest version of the Cockroft-Latham theory of ductile failure, see discussion in chapter 2. This reduced version assumes the stress to be constant during the deformation leading to the failure [61].

Figure 4-13 also shows that the strain estimated by Nakayama's model of prow formation is quite close to the strain value obtained directly using the PIV. This suggests that prow formation indeed occurs by shear of workpiece surface elements at 45° to the workpiece surface. This correlation provides a basis for estimating the prow strain even from *ex situ* measurements of the prow angle θ, with micrographs such as the one shown in Fig. 4-5.

The prow formation was observed even in the absence of segmentation such as in pure sliding without chip formation at large negative rake angles, as well as when cutting with a laminar-flow type 2 chip at large positive rake angles. The corresponding prow angles are also plotted in Fig. 4-13 as "sliding" and "laminar" respectively. In the sliding range, α = -70°, θ ~ 10° and ε ~ 0.2. This is well below the critical (failure) strain ε^* = 0.75; at this condition, only pure sliding occurred without any chip formation or prow cracking. Likewise, for α = 0°, θ ~ 20° and ε ~ 0.4; at this condition, a type 2 chip is observed, with laminar flow and no segmentation. The laminar flow and sliding observations are also consistent with the hypothesis that fracture will occur on the WP surface only if a critical strain value (0.75 for Zn) is exceeded.

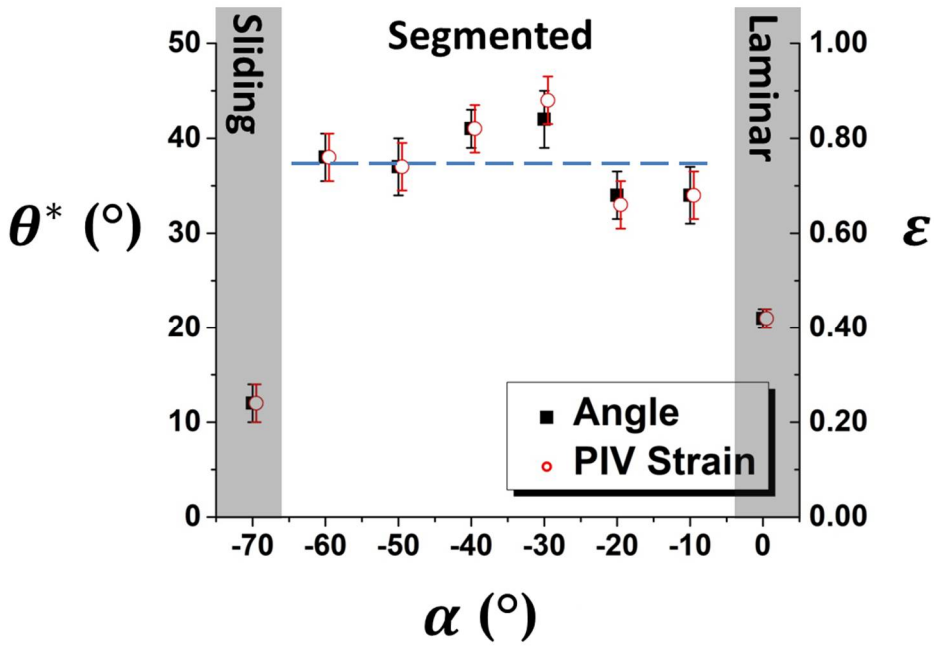

Figure 4-13. Variation of prow angle (θ^*) at onset of cracking and prow strain (ε) with α. Both the prow strain obtained from the prow angle (θ^*) and from the direct PIV analysis of the flow are shown. The dotted line is a least square fit of the (θ^*) data. V_0 = 1 mm/s.

A similar critical-strain controlled fracture and segmentation has been observed in cutting of half hard (H02) brass 260 [17]. In this prior work, a critical value of the prow surface strain (ε^*), approximately 0.8 for crack nucleation in segmentation of brass 260, was noted, for a range of rake angles - θ^* = 35° for rake angles in range of α = -50° to α = +15°. Furthermore, as observed here, in the sliding and type 2 chip (laminar flow) formation regimes, the prow strain was smaller than the critical value and no cracking was observed either.

The PIV and prow angle measurement schemes were applied to the other materials considered in this study – brass 260 (quarter hard), brass 360 (half-hard) and Si-steel – wherein segmentation was observed. The results of the critical slope (θ^*) and critical surface strain (ε^*) at the onset of surface crack initiation for these work materials are summarized in Table 4.1. The

strain estimates were obtained using the prow angle measurements (Nakayama approach – Equation 4-4), as well directly by the PIV.

Table 4-1. Critical slope (θ^*) and critical surface strain (ε^*) of surface crack nucleation for work materials

Material	Rake angle (α)	Critical slope (θ^*)	Critical surface strain (ε^*)- PIV calculations	Critical surface strain (ε^*)- Nakayama estimation
Commercially pure zinc	-60° – -10°	37 ± 2°	0.81 ± 0.09	0.75 ± 0.04
Brass 260 [17] H02-Half hard	-50° – +15°	35 ± 1°	0.80 ± 0.06	0.70 ± 0.02
Brass 260 Quarter hard	-30° & 0°	54 ± 4°	1.15 ± 0.13	1.09 ± 0.08
Brass 360 Half hard	0° & +30°	49 ± 4°	1.02 ± 0.13	0.99 ± 0.08
Silicon Steel (Fe-4%Cr-4%Si)	+10°	65 ± 5°	-	1.31 ± 0.1

In all of these cases, the crack initiation and associated ductile fracture appear to follow a critical strain criterion. The critical strain values fall in the range of 0.75 to 1.3. Furthermore, there is close correspondence between the prow-based strain estimates and the direct PIV measurements, reinforcing the shear-deformation controlled prow-formation hypothesis (model). The observations suggest opportunities for using the chip-formation segmentation to study ductile fracture in metals, and obtain another index of workability for metals that may be more relevant to deformation processing. A further study in this latter regard is warranted.

We do not report critical surface strain (ε^*) obtained by PIV for the cutting of the silicon steel. Unfortunately, in this case, the image sequences recorded of the deformation region were obscured somewhat by debris generated during the cutting; this impeded the PIV analysis.

4.4 Hydrostatic Pressure and Triaxiality Condition at Failure Origin

It is worth examining briefly the role of hydrostatic stress (p) in the current fracture development in the prow region, since it is well known that ductile failure in metals is quite sensitive to the level of this hydrostatic stress (p). Typically, the strain at fracture increases with increasing hydrostatic pressure, as established in the pioneering work of Bridgman [47], Pugh [50] and others [48], [59]. This role of hydrostatic pressure is also macroscopically manifested in micro/nano hardness testing with sharp indenters. In these cases, it is possible to produce fully plastic indentations, without cracking, at light loads, in brittle solids like glasses and ceramics. This is because under a sharp indenter, there is significant hydrostatic pressure superimposed onto shear stresses in the indentation deformation zone which suppresses cracking. Recent work on ductile failure [64] has suggested that the local stress triaxiality, as expressed by a parameter η = ratio of hydrostatic stress (p) to effective stress ($\bar{\sigma}$), can influence the failure strain, with ductile fracture predicted as being infeasible for η < -1/3. It is worth examining the prow failure observations in the framework of some of these theories.

Consider 2-D plastic deformation of an element on the WP surface ahead of the tool to form a prow element. If this material element is treated as a rigid, plastic solid with representative shear yield stress (k), then the principal stresses in the element are $-2k$, $-k$ and 0 (negative sign due to compressive stresses). This stress state corresponds to an effective (von Mises) stress of $\bar{\sigma} = \sqrt{3}k$, and $p = -k$, with $\eta = -1/\sqrt{3}$ [12]. Since η in the prow is independent of α, this could explain the observed constancy of strain for prow crack formation. Interestingly, in the present case, since failure occurs even with η $(= -1/\sqrt{3}) < -1/3$, it is a counter-example to the popular ductile failure theory proposed by Wierzbicki [64]. We will discuss, further, the contribution of

hydrostatic pressure in section 5.1 wherein we show that segmentation can be suppressed by increasing the hydrostatic pressure on the free surface of the chip.

One other observation is finally in order regarding the strain fields in cutting and the critical strain value for segmentation. In the cutting of Zn (Fig. 4-4), the strain field data shows that in all of the segmentation cases, the critical prow strain for ductile failure has values (Figs. 4-4 b-e, also Table 4-1) that are somewhat smaller than the strain in the interior of the type 2 chip (laminar flow), see Fig. 4-4 e. Yet no failure is observed in the interior of the type 2 chip, despite the higher strain. The reason for the chip interior being able to support a larger level of deformation without failure, than the prow surface, is likely due to greater levels of hydrostatic pressure in the chip interior than on the prow surface (where $p = -k$). The latter fact is known based on prior finite element analysis of stresses in the chip volume and prow region (private communication, Dr Narayan Sundaram, Indian Inst. Sci., Bangalore, India). We hope to explore this aspect in some more detail in the future.

4.5 Segmentation Morphology and Force Oscillations

In this section we pay specific attention to the morphological attributes of segmentation in free machining, and correlations between segmentation morphology and characteristics of the cutting force profiles.

Figure 4-14 shows the chip morphologies from FM brass 260 and Zn; these are through thickness cross sections (along chip length) taken from the side of the chip. The typical saw-tooth characteristic of the type 3 segmented chip is seen in both cases in this side view. Based on this 2D morphology, it would appear that the segmentation is similar in both materials. It has been often stated [44] or assumed (private communication with Dr. Rachid M'Saoubi, Seco Tools) that segmentation will cause force oscillations with adverse consequences for tool life. Some of this

speculation has come from measurements of force profiles in cutting under conditions of shear band formation which produces a very similar saw-tooth chip (see type 4 chip in Fig. 1-2). Given the similarity in segment morphology between the brass and Zn, one may expect similar cutting force profiles, including oscillations, for these two materials.

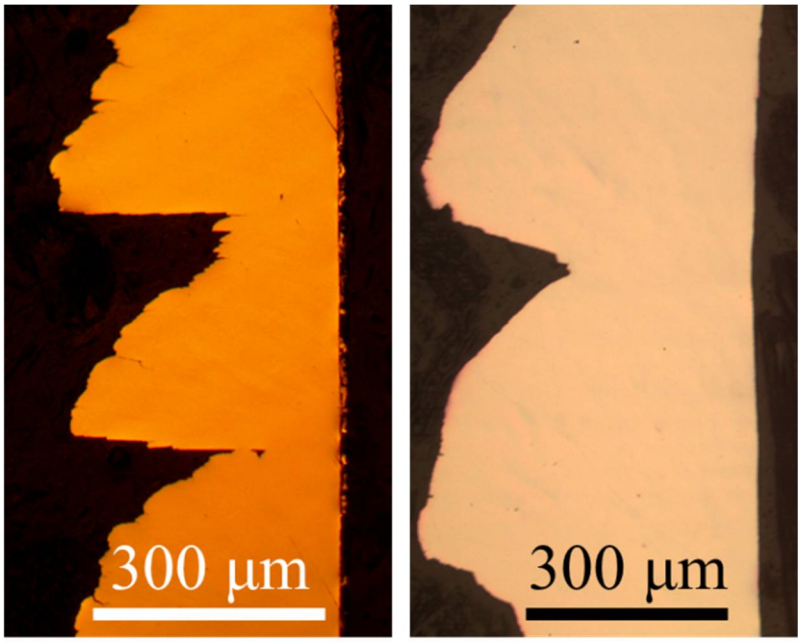

Figure 4-14. Optical micrographs of through thickness cross sections of segmented chips taken from the side. Rotary plunge cutting α = +5°, V_0 = 500 mm/s. (a) Brass 260 t_0 = 100 μm and (b) zinc t_0 = 250 μm

However contrary to this expectation, the specific cutting force profiles were quite different between the two materials (Fig. 4-15) (Note the specific force is the force per unit (undeformed) chip cross-section area, i.e., cutting force/$w\ t_0$). There are significant oscillations in the force recorded with the brass 260, with oscillation frequency of ~ 240 Hz. This frequency is nearly identical to the segmentation frequency of ~ 250 Hz derived from the micrographs of chips, confirming a strong correlation between segmentation and force oscillations. However, with the Zn, the segmentation did not result in force oscillations such as were observed in the cutting of the Zn (Figure 4-15).

To understand this difference, we examined the 3-D morphology of the chips, going beyond the side-view thickness cross-section. The morphology of the back (free) surface of the chips showed significant differences in the nature of the segmentation between the Zn and brass 260, providing clues also to differences in the force profiles.

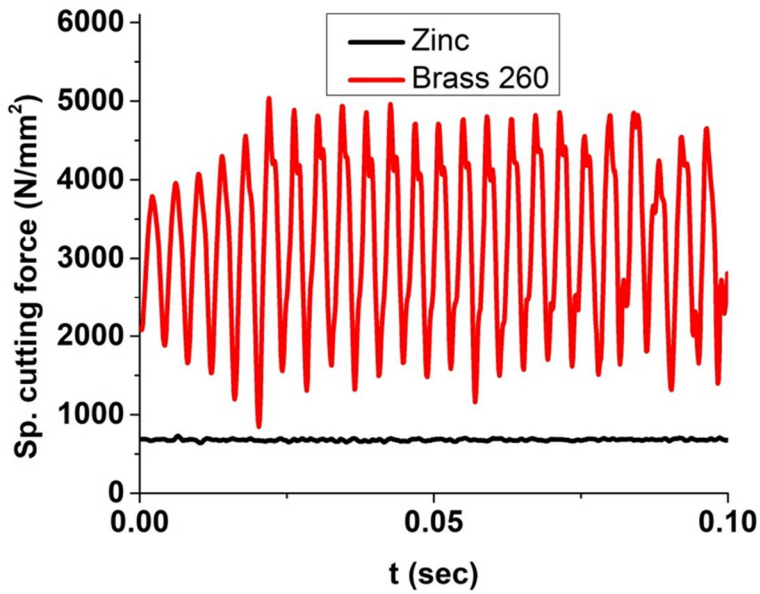

Figure 4-15. Specific cutting forces corresponding to the segmented chip formation for the brass 260 and Zn. The cutting conditions correspond to Fig. 4-16.

Figures 4-16(a) and 4-16(b) show the segmentation morphology across the width of the chip back-surface for cutting of brass 260 and Zn, respectively. The segments are seen to run straight across the width in brass 260 while in Zn they meander across the width. Both chips, however, showed similar saw-tooth morphology from the side, Figure 4-14. It is this difference in the nature of the segmentation that is reflected in the cutting forces. Since the "straight-across-width" morphology would mean that every width cross-section of the brass 260 chip experiences an identical (segmentation) deformation condition at the same time, the force profile shows a loading and unloading pattern resulting in a force oscillation at the same frequency as the segmentation frequency. Whereas, in the Zn chip, since each width location experiences a

somewhat different (segmentation) deformation condition at a given time, the segmentation effect on the force is diffuse; hence, the lack of any force oscillation. That is the meandering segmentation potentially involves simultaneous activation of multiple segmentation events across the chip width. Since each of these segments will be in a different state of development at a specific time, the cutting force does not show any specific oscillatory pattern that corresponds to the segmentation frequency. We hypothesize therefore that segmentation will lead to force oscillations in cutting only if it is of the "straight-across-width" type, and not for the meandering segmentation case.

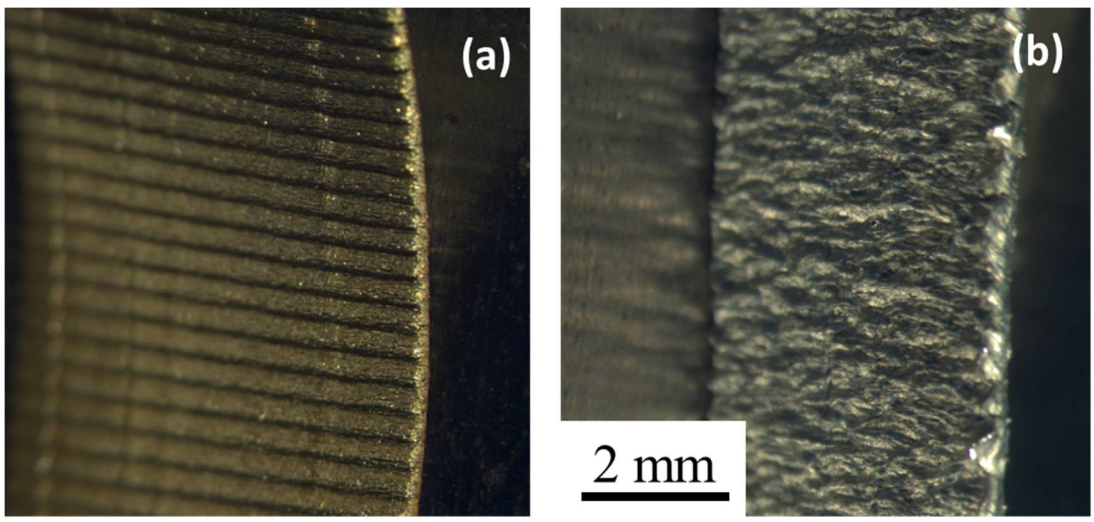

Figure 4-16. Optical micrographs of chip back-surface showing differences in segmented chip morphology across the chip width, (a) straight segments in brass 260, t_0 = 100 μm (b) meandering segments in zinc, t_0 = 250 μm. Rotary plunge cutting. α = 5°, V_0 = 500 mm/s.

We also examined the 3D morphology of the chip back surface profiles using optical and stylus profilometry. To quantify this morphology, we used the roughness parameters for the back surface of the chips - R_a, R_q, S_a, S_q, and R_z. Note that in the present context these do not represent surface roughness parameters for a surface as in the conventional sense; instead, they represent the "roughness" arising from the groove profiles of the segmentation). The definitions of these parameters and associated details as to how they were obtained (e.g., sampling length, cut-offs etc.)

are given in Appendix A. It will suffice to define them briefly here for interpretation of the results. The parameter definitions are: R_a arithmetic average of the roughness profile along a line scan; R_q root mean square of profile deviation from average profile for a line scan; S_a arithmetic average of the surface roughness (extension of R_a to a surface) for a surface map; S_q root mean square deviation from average surface (extension of R_q to a surface); and R_z average peak-to-valley profile roughness from a line scan. Thus R_a, R_q, and R_z are parameters that are evaluated over a line profile while S_a and S_q are extracted from 3D profilometry of a full representative surface region. Also note that R_a and R_q are essentially analogous parameters.

The 3D surface roughness profiles (optical profilometry) for the back surface are shown in Figure 4-17(a) and 4-17(b) for the brass 260 and Zn chips, respectively. These confirm the occurrence of straight segments across the width in the brass 260 chips, and meandering segmentation in the Zn. The 3D profile of Figure 4-17(a) for the brass 260 has an $S_a = 25.06$ μm (arithmetic average) and $S_q = 30.57$ μm (rms value); the corresponding parameters for the zinc chip (Figure 4-17(b)) are $S_a = 29.06$ μm and $S_q = 37.54$ μm.

Regularly spaced bands (grooves), with spatial frequency 2.75 bands/mm, were detected in the line profile scan made across the chip length in the brass 260 chip (Figure 4-17c). These are consistent with straight grooved segments running along the chip width. However, in the line scans taken from the Zn chip, there was no dominant band frequency observed, consistent with meandering segments. A representative line profile across the Zn chip length is shown in Figure 4-17(d). The line profile of Figure 4-17(c), for brass 260, has $R_a = 23.98$ μm, $R_q = 29.98$ μm, and $R_z = 102.82$ μm while that of zinc shown in Figure 4-8(d), has $R_a = 24.07$ μm, $R_q = 29.67$ μm, and $R_z = 93.5$ μm. It must be noted that while the back (free) surfaces of the zinc and brass 260 chips have similar “roughness” parameter values, their 3-D topography is quite different.

Another interesting observation is effect of (or lack thereof) segmentation on the cut surface of workpiece. Segmentation in cutting of brass 260 as well as zinc resulted in production of smooth cut surfaces on the top face of workpiece. All the workpiece cut surfaces formed (not shown here) have a roughness value of less than $R_a = 0.76$ µm, $R_q = 0.92$ µm, and $R_z = 0.94$ µm. Hence, we clarify the misconception/assumption that segmented cutting always results in formation of rough features on the surface of workpiece.

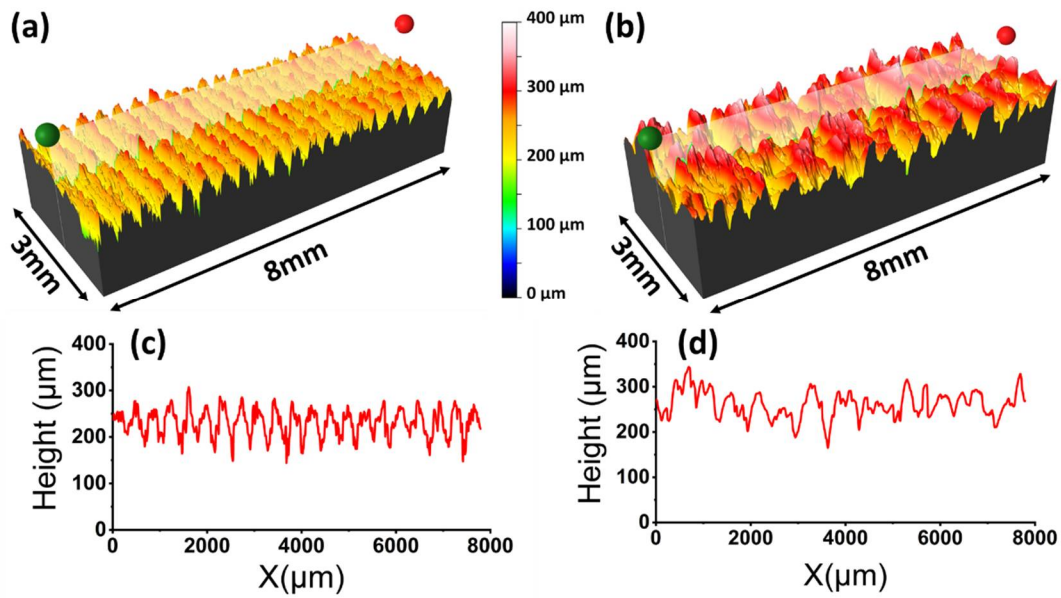

Figure 4-17. Optical profilometry of chip back-surface showing segmentation morphology of (a) brass 260, straight segments across width, $t_0 = 100$ µm and (b) zinc, meandering segments across the width, $t_0 = 250$ µm. Representative line scans of the same surfaces along the length of the chip (at the line profile between green and red ball) are shown in (c) brass 260 and (d) zinc. Rotary plunge cutting, $\alpha = 5°$, $V_0 = 500$ mm/s.

The forces and segmentation morphology were also analyzed for the brass 360 and Si-steel material systems. These observations further confirmed the correlation (and hypothesis) between the segmentation morphology (straight vs meandering) and force profile attributes (oscillation/no-oscillation).

Figure 4-18 shows 3D optical surface profile of chip back-surface for the brass 360 chip (S_a = 34.04 μm, S_q = 41.63 μm, R_a = 32.41 μm, R_q = 39.05 μm, and R_z = 146.79 μm). It is clear from the 3D surface profile that the segmentation runs straight across the chip width as in the brass 260. Furthermore, in this case, because of the somewhat more extreme nature of the segmentation (note the segmentation was many times found to encompass the entire chip length), the workpiece cut surface in the wake of the tool was also observed to have undulations, see Fig. 4-6. The workpiece surface profile parameters were S_a = 1.35 μm, S_q = 1.72 μm, R_a = 1.55 μm, R_q = 1.26 μm, and R_z = 6.22 μm. The workpiece undulations were found to have an average wavelength or pitch p = 238.4 μm, based on frequency analysis of the surface profile. It is very likely that these undulations resulted from the segmentation process (see also discussion below). From the wavelength/pitch of the workpiece undulations and the workpiece speed (V_0 = 6 mm/s), we estimated the temporal frequency of the undulations (segmentation) as $f_{work} = \frac{6\ mm/s}{238.4\ \mu m}$ = 25.2 Hz.

The corresponding specific cutting force profile for the brass 360 is shown in Figure 4-18(c). Consistent with the segments running straight across the chip width, we see oscillations in the force profile. The oscillation frequency is f = 23.9 Hz; with average force value of 409 N/mm^2 and peak-to-valley force amplitude of the oscillatory component 84 N/mm^2. This frequency is very close to the segmentation frequency f_{work} = 25.2 Hz derived above from the workpiece surface profile measurements. This close correspondence between the two sets of frequencies is strong evidence that the force oscillations arise directly from the segmentation process, that is they are one-for-one correlated.

Additional information about the segmentation mechanics and underlying deformation could be derived from the surface profiles. The segments on the chip back surface (Fig. 18(a))

were found to have an average wavelength or pitch p_c = 130.4 μm. As noted earlier, the undulations on the cut workpiece surface have a wavelength/pitch p = 238.4 μm. Based on these two wavelength values, and consideration of the cutting kinematics [13], [39], we can estimate the chip thickness ratio as $\lambda = \frac{p}{p_c}$ = 1.83 (equation 4-1). This value is essentially identical to the cutting ratio estimated from the *in situ* imaging (λ = 1.85) using workpiece and chip velocity measurements. Using this λ = 1.83, and equation 4-2, we can estimate other deformation parameters such as the shear angle; this angle is obtained as φ = 29°. This estimate is in close agreement with the corresponding shear angle value of φ = 30° obtained directly from the *in situ* imaging and PIV analysis, see also Fig 4-8.

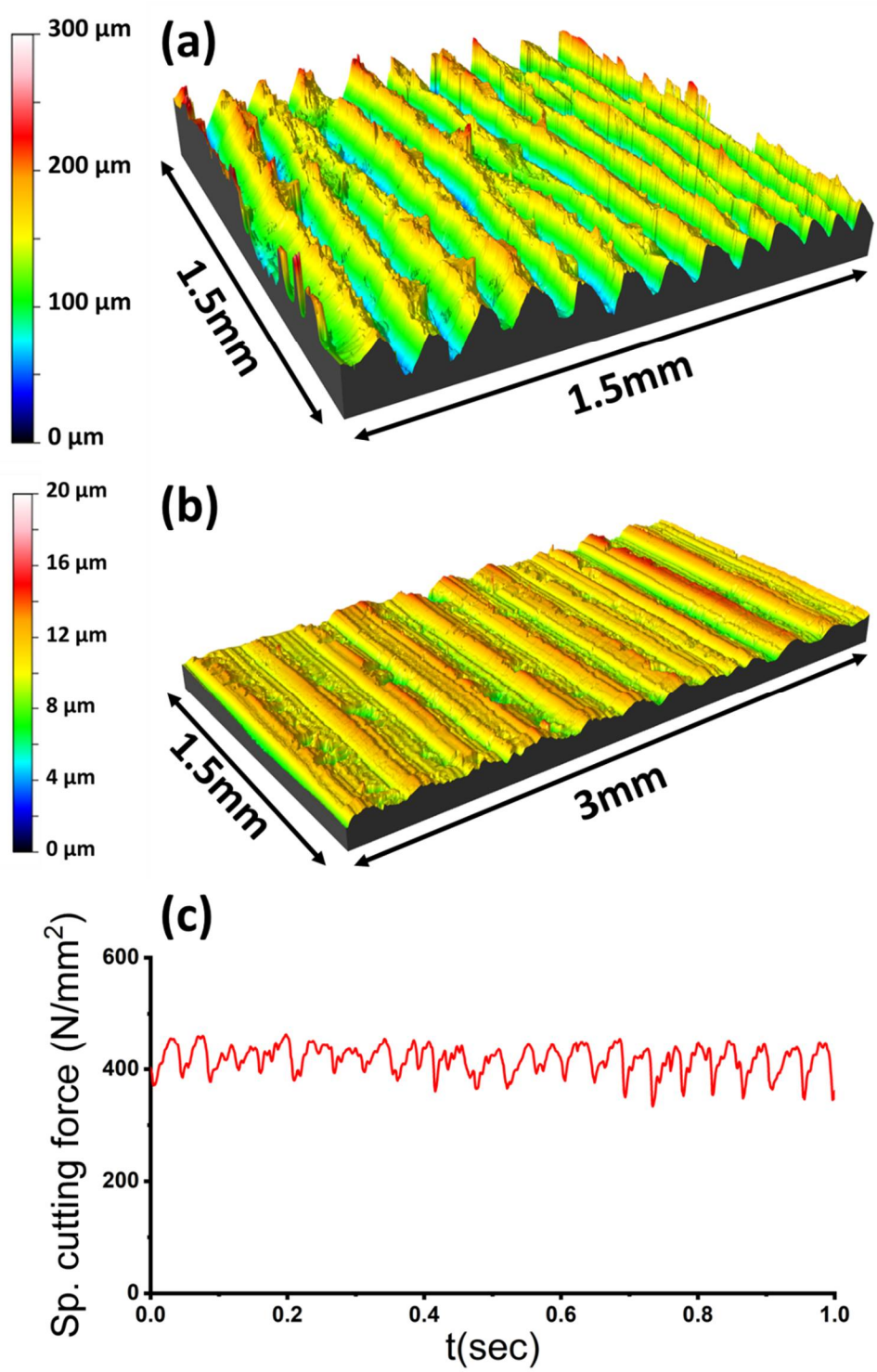

Figure 4-18. Optical profilometry of (a) chip back-surface, and (b) workpiece surface after cutting. (c) Specific cutting force. Brass 360, $\alpha = 0°$, $V_0 = 6$ mm/s, and $t_0 = 120$ µm.

The segmentation in the silicon steel was of the meandering type analogous to the Zn. Figure 4-19(a) shows the 3D surface profile of the chip back-surface (same cutting conditions as figure 4-11) for this steel. While the segmentation in figure 4-19(a) is quite pronounced, no one segment covers the entire width of the chip. In this case, the specific cutting force (figure 4-19(b)) also showed no distinct force oscillation, remaining fairly constant. The observed gentle variation in the cutting force appears to be the result of activity of 2 or more segments across the width of sample at any point of time.

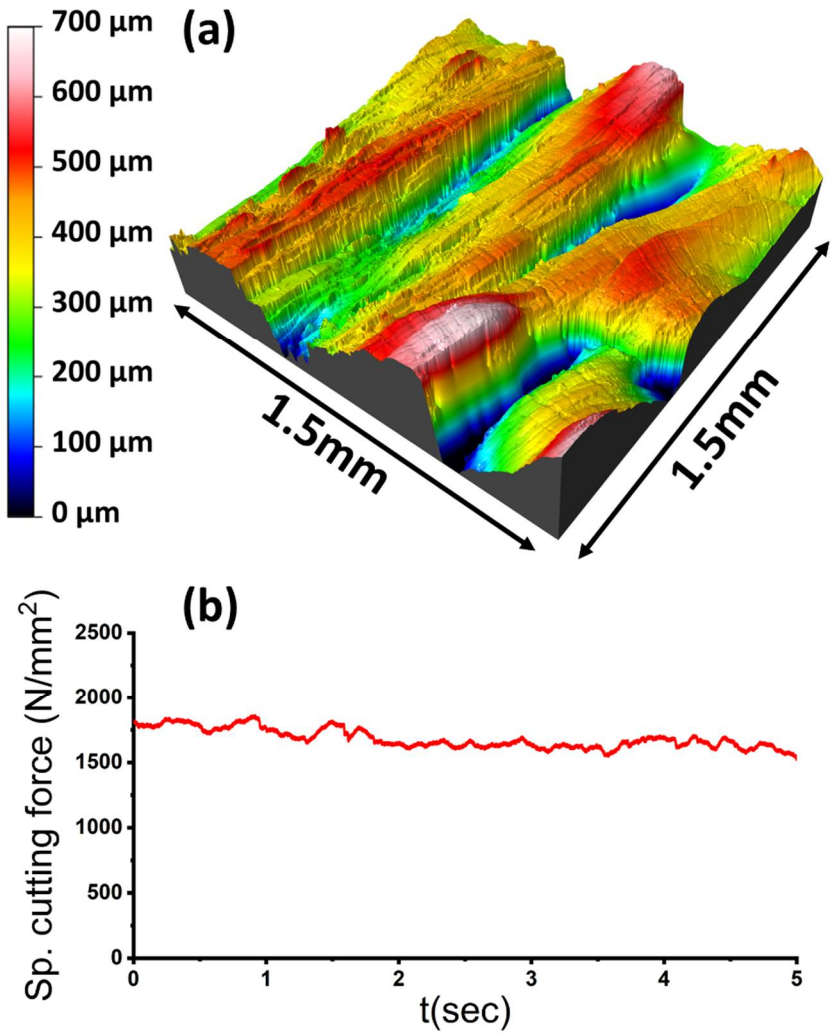

Figure 4-19. (a) Optical profilometry of chip back-surface and (b) specific cutting force. Silicon steel, α = +10°, V_0 = 3 mm/s, and t_0 = 120 µm.

In summary, the occurrence of segmentation results in promotion of surface roughness on the back-surface of the chip. There are 2 types of segment morphologies based on the segmentation pattern across the width of the chip. The first type with meandering segments seen in cutting of Zn and silicon steel. The second type, wherein the segments run straight across the width of the chip, occurs with brass 260 and brass 360. In the latter case, the cutting force shows oscillations that are in sync with the segment formation. Meandering segmentation involves simultaneous activation of more than one segmentation event across the width of the chip. Since each of these segments will be in a different state of development at a specific time, the cutting force does not show any specific oscillatory pattern that corresponds to the segmentation frequency. It has also been observed that in some of the extreme cases of the segmentation like in brass 360, the workpiece cut surface also has a replica of the chip segmentation features. We have also highlighted how key deformation parameters of the cutting process can be derived from post-cutting analysis of the segmentation features and surface profiles.

The occurrence of the straight or meandering segmentation morphologies likely has workpiece material origins: microstructure and ductility/workability. Future work will attempt to resolve this.

5. CONTROLLING SEGMENTAION

We now turn our attention to possible methods for suppressing segmentation as well as for enhancing it. Based on the observations discussed in the last chapter of how segmentation is often triggered by a crack nucleating on the back surface of the chip in the prow region, and propagating towards the tool tip, we propose material-agnostic methods for controlling segmentation. By 'Control', here, is meant not only suppression of segmentation, but also means to induce it to occur in metals, e.g., ductile metals, where segmented flow would not be the norm. The observations pertaining to segmentation control in this chapter also bring out some additional, hitherto, unknown aspects of segmentation mechanics. They suggest new routes for studying ductile failure in metals.

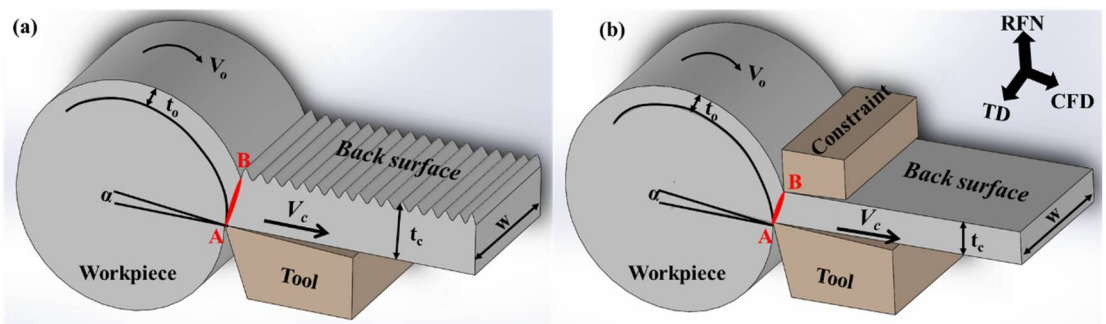

Figure 5-1. Schematic of Free Machining (FM) and constrained cutting by Hybrid Cutting Extrusion (HCE) techniques. (a) FM process is the conventional process of cutting of material. (b) HCE is the process of controlling material flow and output chip thickness, t_c, through application of a constraint to the back surface of the chip/strip. This constraint application *a priori* defines chip geometry and shape, at the exit of the deformation zone unlike in FM.

5.1 Suppression of Segmentation in Zinc by Constrained Cutting Using Hybrid Cutting Extrusion (HCE)

Based on our observations that segmentation is initiated by a crack in the prow region, and in light of theories of ductile failure, it would appear that if prow crack nucleation were to be suppressed by decreasing p (i.e., increasing hydrostatic pressure and reducing the stress triaxiality

η), then a smooth continuous chip should form by laminar flow. In fact, given that the effective stress in the deforming prow is constant ($= \sqrt{3}\,k$), the only means of varying η is via p. One way of increasing the hydrostatic pressure in the prow is by application of a local constraint here, via a suitably placed die that clamps down on the back of the chip (e.g., Fig 5-1(b)). The application of such a constraint will also define the geometry of the chip, *a priori*, at the exit of the deformation zone, unlike in free machining (FM), see Fig. 5-1(a), where this exit chip thickness is undefined. If segmentation can indeed be suppressed by this type of constrained cutting, then given that the exit geometry is now defined, we should also be able to use this constrained cutting process to produce metal sheet/strip in a single deformation stage by machining chip-formation. The application of this type of constrained chip formation to explore suppression of segmentation is motivated by prior work where it was found that constrained cutting could suppress shear banding in chip formation [12].

To explore suppression of segmentation by application of a constraint, we utilize the deformation configuration shown in Fig. 5-1(b). This constraint cutting method, we call hybrid cutting-extrusion (HCE), where the chip forms by a simultaneous process of cutting and extrusion. In contrast to free machining (FM), where the chip back-surface is free, HCE utilizes a constraint that is placed along the back (free) surface of the chip in the deformation zone to constrain and control the flow of material. While in FM, the chip thickness ratio, $\lambda = \frac{t_c}{t_0}$ (figure 5-1(a)), is a variable, that is determined by the cutting condition and material behavior, in HCE it is an input parameter (pre-set) that is by setting the distance between constraint and cutting tool rake face at a desirable value, t_c (exit or deformed chip thickness). Since the chip thickens considerably during its formation in FM, the (deterministic/pre-set) chip thickness ratio λ in HCE process will always be smaller than the λ in FM process.

We now study how the HCE process influences the segmentation process in cutting of Zn. We also study effects of this constrained cutting on the flow dynamics of segmentation.

The use of constrained cutting (HCE) to influence segmentation and prow-cracking was studied both at low speeds, using linear cutting (Fig. 5-2); and at higher speeds, using rotary (radial) plunge-turning configuration wherein the chip was formed by moving the tool radially in into a rotating workpiece (Fig. 5-1). In both the low-speed and high-speed cutting, a high-speed steel die (constraint) was typically mounted across from the primary cutting tool and pressed against the WP and chip back-surface. By adjusting the location of this die, different levels of λ could be applied. With the harder alloys like the silicon steel, tungsten carbide tools and dies were used.

Figure 5-2(a) shows the usual segmented chip formation that occurs in conventional (free) cutting of Zn at $V_0 = 1$ mm/s. The segmented chip is characterized by alternating regions of lower (1–2) and higher (3–4) strain. The average λ value was ~ 2.5. The dotted white line in the figure demarcates the WP surface and chip back-surface, and the segmentation morphology. Upon cutting with the constraint ($\lambda = 2.0$), the prow-crack and segmentation are seen to be completely suppressed (Figure 5-2(b)). What results now is a chip of uniform thickness, with homogeneous laminar flow and uniform strain ($\varepsilon \sim 2$); this chip resembles a metal strip. The changeover from segmented chip to the smooth continuous chip in the HCE is quite striking. The strain field also shows a thin deformed layer on the chip back-surface, akin to the secondary deformation zone at the tool-chip interface, indicating that the constraint imposes some frictional deformation similar to that prevailing along the tool rake face. The streaklines in Figure 5-2(c) show that laminar flow occurs in the HCE throughout the chip thickness, as well as in the boundary regions exposed to higher frictional forces.

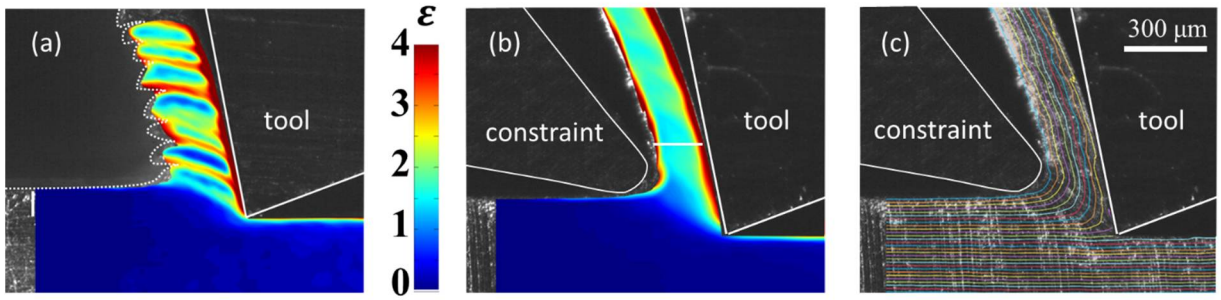

Figure 5-2. Suppressing segmentation at low speeds by constrained cutting, and associated strain fields in chip: (a) conventional cutting (FM, λ = 2.5), and (b) constrained cutting (HCE, λ = 2.0). (c) The streakline pattern for b showing uniform flow. Linear cutting, Zn, α = -10°, V_0 = 1 mm/s, t_0 = 150 μm.

Constrained cutting (HCE) was equally effective at suppressing segmentation in higher-speed cutting of Zn (V_0 = 0.5 to 1 m/sec); this was done in a rotary plunge turning configuration. Figures 5-3(a) and 5-3(c) show a highly-segmented and irregular chip with non-homogeneous microstructure produced in FM. Whereas, a continuous chip of uniform thickness (Fig. 5-3(b)), and relatively homogeneous microstructure (Fig. 5-3(d)) is seen to be produced in the HCE (λ = 1.3). There is no barrier to using constrained cutting at even higher speeds; in fact, HCE has been used to suppress shear banding in cutting of Ti and Ni alloys at speeds of up to 3 m/sec [12], [86].

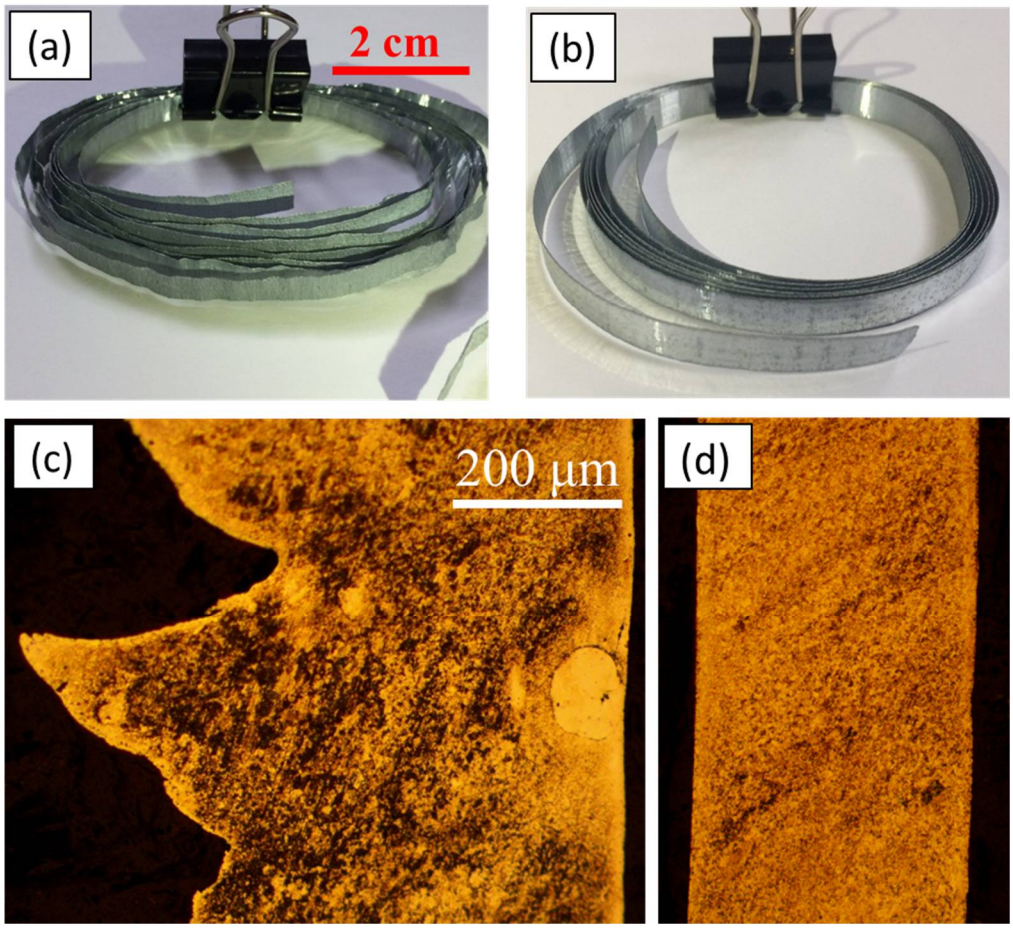

Figure 5-3. Suppression of segmentation in Zn at higher speeds by HCE. (a) Segmented metal strip (chip) with irregular edges produced by FM (λ = 2.2), (b) continuous smooth metal strip (chip) produced by HCE (λ = 1.3), (c) through-thickness chip cross section from conventional cutting showing pronounced segmentation, and (d) through thickness chip cross-section from the HCE showing uniform thickness and homogeneous microstructure in strip. Rotary cutting, Zn, α = 5°, V_0 = 500 mm/s, t_0 = 250 μm.

It was also found that the exact location (and exact lambda) of the constraint needed to suppress segmentation was not very critical with the Zn, unlike in shear banding [12]. In the latter case, the constraint level had to be set sufficiently high (that is smaller lambda) so that the shear band propagation phase, by sliding of adjacent shear band segments could not occur. This corresponded approximately to the constraint being set at the bottom of the "saw-tooth". In other words, to suppress the banding (Type 4 chip in Figure 1-2), the constraint had to be set inward

from the back-surface of the chip by at least a distance equal to the band amplitude (saw-tooth amplitude). In the present instance with HCE of Zn, setting the constraint inward from the chip back-surface, by even a fraction of the segment amplitude was sufficient to arrest the segmentation. For reference, the lambda values in low speed FM and HCE of Zn were 2.5 and 2.0, respectively, giving an indication of the severity (or lack thereof) of constraint needed to suppress the segmentation.

The suppression of segmentation by use of a constraint via HCE can be explained based on considerations of the hydrostatic stress state and stress triaxiality in the prow region ahead of the tool where the segmentation is nucleated by a crack. Consider a plastically deforming element on the WP surface ahead of the tool, as before, but now located under the constraint. The stress state in the element is now $(p_0 + 2k)$, - $(p_0 + k)$, and - p_0, where p_0 is the normal stress applied by the constraint. The friction due to the constraint is neglected. The effective stress in the deforming element is again $\sqrt{3}k$, unchanged from the case of FM discussed earlier in section 4.4. But the magnitude of the hydrostatic pressure in the element is now $(p_0 + k)$, which is $> k$, the hydrostatic pressure in the same prow region of FM. Hence, the stress triaxiality in the prow for the HCE case is $\eta = -(p_0 + k)/\sqrt{3}\,k$, which is $< -1/\sqrt{3}$ (conventional cutting). A conservative assumption for the stress applied by the constraint is $p_0 = 2k$ (yield strength). Then the elemental hydrostatic pressure $= 3k$, which is 3 times that in conventional cutting; and $\eta = -\sqrt{3}$, which is $< -1/\sqrt{3}$ of conventional cutting. Both of these factors (higher hydrostatic pressure and more negative triaxiality) inhibit ductile failure in the prow, suppressing segmentation in the HCE. Furthermore, it is clear why even a constraint of moderate pressure ($\sim 2k$) can be effective in arresting segmentation, explaining also why the location of the constraint is less critical for suppressing the segmentation in the HCE.

Our analysis also explains another apparently paradoxical aspect of segmented chip formation. While a crack is initiated on the prow-surface at $\varepsilon \sim 0.75$, the bulk (interior) of the Zn chip sustains strains as high as 2–3, see Figures 5-2(a) and 5-2(b), without cracking. This is likely due to a more compressive p prevailing in the chip interior, a consequence of greater constraint on the deformation, therein, from adjoining material.

Suppression of segmentation can be beneficial for multiple reasons. Segmented chip formation can cause force oscillations, with adverse consequences for process performance and product quality. Importantly, by suppressing segmentation, it also becomes feasible to use (constrained) chip formation via HCE to produce sheet and strip in a single step by a cutting-based deformation process [87]. This can be of value for producing strip/sheet products from specialty metals and metals of poor workability (e.g., Ti, Mg, Fe-Si electrical steels). Furthermore, unlike rolling processes, typically used to make sheet via multi-stage deformation (often 10-20 stages), the HCE is a single-stage process for sheet production.

The suppression of segmentation by HCE can also be seen from the SEM images, Figure 5-4, and optical profiles, Figure 5-5, of the chip. The SEM image of conventional cutting Zn chip (Figure 5-4(a)) and corresponding optical surface profile (Figure 5-5(a)) show recurring segments along the chip length, with the segments traversing a meandering path across the chip width. In contrast, the back-surface of the chip produced by the HCE shows a relatively smooth profile consistent with suppression of the segmentation, see SEM image of Figure 5-4(b) and optical profile of Figure 5-5(b). A few uneven (patchy) regions however do exist, but they are sporadic and make only a minimal contribution to the roughness. The 3D optical profile of the HCE chip back-surface (Figure 5-5(b) and 5-5(c)) gives an arithmetic average roughness value of $S_a = 0.7$ μm and $R_a = 0.7$ μm. These values are also close to the roughness values obtained on the rake-

face side of the chip (R_a = 0.2 μm and S_a = 0.2 μm, Figure 5-5(d)). The roughness can be further improved by application of a light cold-rolling operation to the strip after the HCE. Typically, the rake face side of the chip has a smooth finish since it is a replica of the tool rake surface. In the so-called patchy areas of the HCE chip, the roughness is higher with S_a= 2.9 μm and S_q = 4.2 μm (not shown here). A summary of typical surface roughness values from various strips produced by the HCE and FM, including the Zn strips, is given in Table 5-1 at the end of this chapter. Note that the different roughness parameters are also defined in Appendix A.

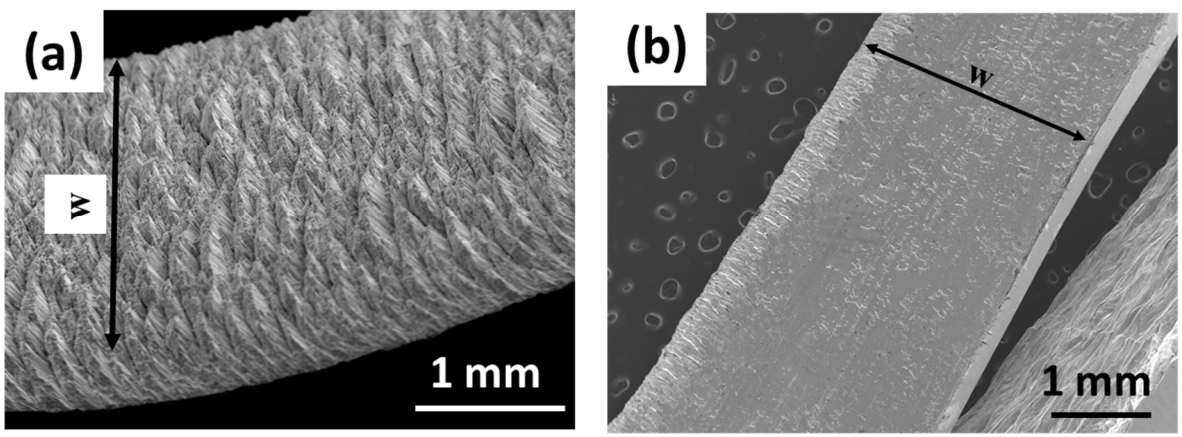

Figure 5-4. SEM images and optical profilometry traces of the Zn chip back-surface showing suppression of the segmentation at higher speeds by constrained cutting: (a) SEM image of chip from conventional cutting showing segmentation, and (b) SEM image of HCE strip showing uniform topography without the segmentation grooves. Rotary plunge cutting, Zn, α = 5°, V_0 = 500 mm/s, t_0 = 250 μm. Same chips as figure 5-3.

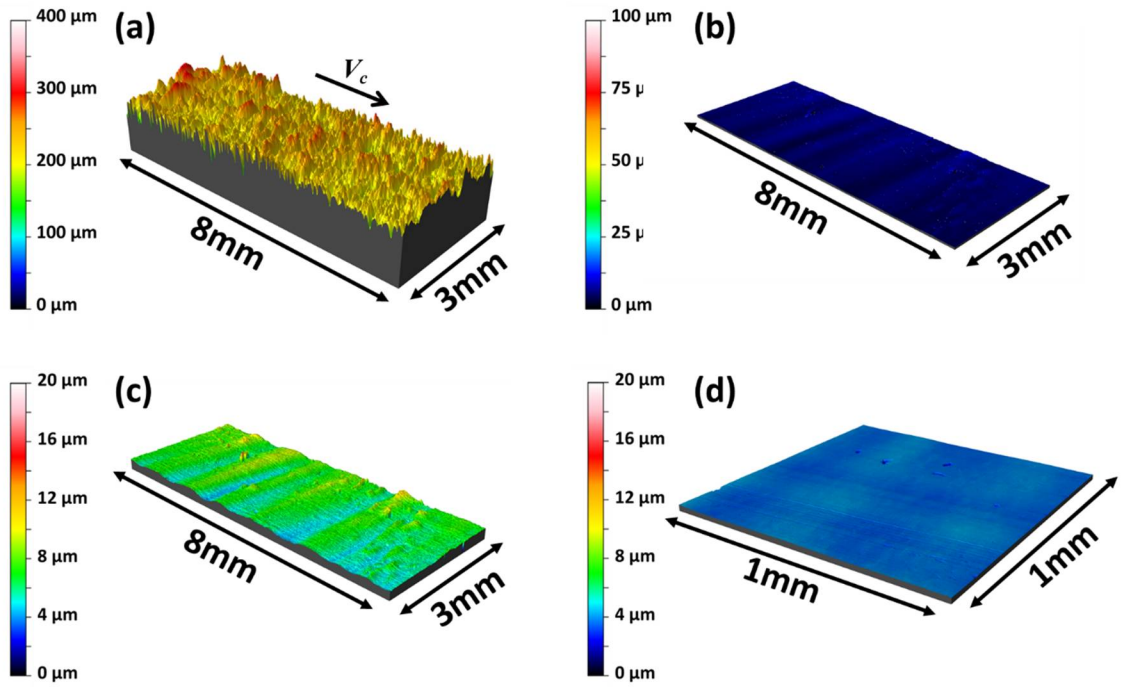

Figure 5-5. Optical profilometry traces of the Zn chip: (a) back-surface of FM chip, and back-surface of HCE strip in (b) 100 µm range, and (c) 20 µm range. (d) Optical profilometry of rake side of constrained cutting chip. Same cutting conditions as Fig. 5-4.

5.2 Suppression of Segmentation in Other Material Systems (Brass and Si Steel)

We now turn our attention to some other material systems of commercial importance for strip and sheet production. These are Hi-Si steel (4% Si content) and brass 260/360 alloys. The former is a soft magnetic alloy under consideration for high-efficiency electric motor/transformer cores. Because of its very poor workability, it is difficult, if not impossible, to produce this alloy in sheet form by conventional multistage rolling processes. All of these alloys, the Si-steel and the brasses exhibit segmentation in conventional cutting (FM) broadly analogous to the Zn. Hence, they provide good material systems to explore the suppression of segmentation via HCE besides being also of practical relevance for applications in strip and sheet forms.

Suppression of segmentation in these alloys was studied using the HCE approach, using the plunge turning configuration at higher speeds (2000-6000 mm/s). Figure 5-6 shows chips

produced by FM and the HCE from brass 360. The FM chips are highly segmented (Fig. 5-6(a)), in fact completely separated as smaller particles. In fact, the majority of the FM chip sections are standalone segments. Even within each of these segmented, there is additional segmentation as revealed by optical profilometry of the back side of the chip. Note that the segmentation grooves in the FM chip run straight across the chip width in the brass 360 (Fig. 5-7(a)), in contrast to the meandering segmentation in the Zn (Fig. 5-5(a)). The peak-to-valley height (R_z) of the segments, as obtained from the profile is ~ 509.7 µm, approximately 75% of the deformed chip thickness.

On the other hand, the HCE produces a continuous strip with a commercially acceptable surface finish on the back surface, see figures 5-6(b), 5-7(b), and 5-7(c). In this case, the λ value used was 1.7 and extent of the constraint was quite severe because of the extreme nature of the segmentation. The corresponding λ for FM is not given for the 360 case since the chip was highly segmented. Upon comparing the surface profiles of the back surface of the FM chip with that of the HCE strip, it is clear that there is an ~ 70-fold decrease in the peak-to-valley roughness of the HCE strip – from R_z = 509.7 µm to 7.1 µm. The corresponding S_a/R_z values are 143.7/132.9 µm (FM) and 1.3/1.7 µm (HCE). The typical surface roughness values are summarized in Table 5-1.

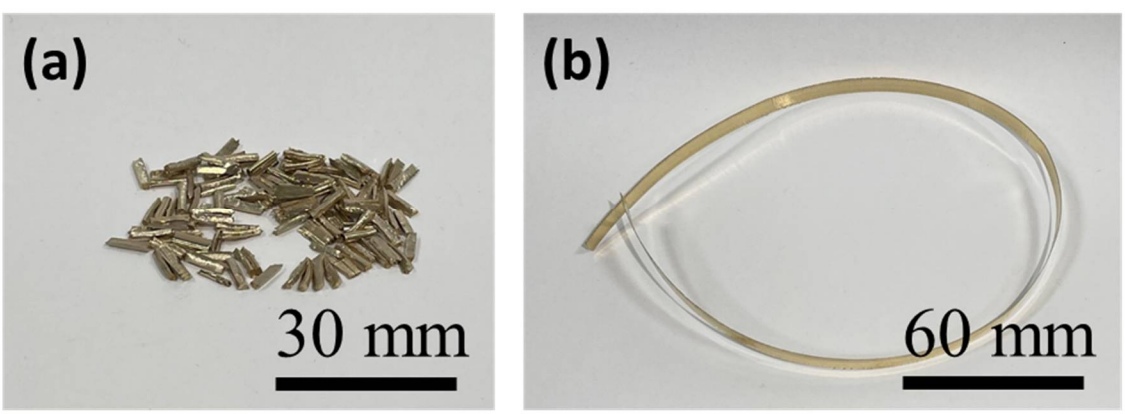

Figure 5-6. Images of (a) FM chip, and (b) HCE strip for cutting of brass 360. Segmentation in FM encompasses the entire thickness of the chips which results in separated chip segments. HCE process suppresses the segmentation and produces a continuous strip. Rotary cutting α = +5°, V_0 = 2000 mm/s, and t_0 = 125 µm.

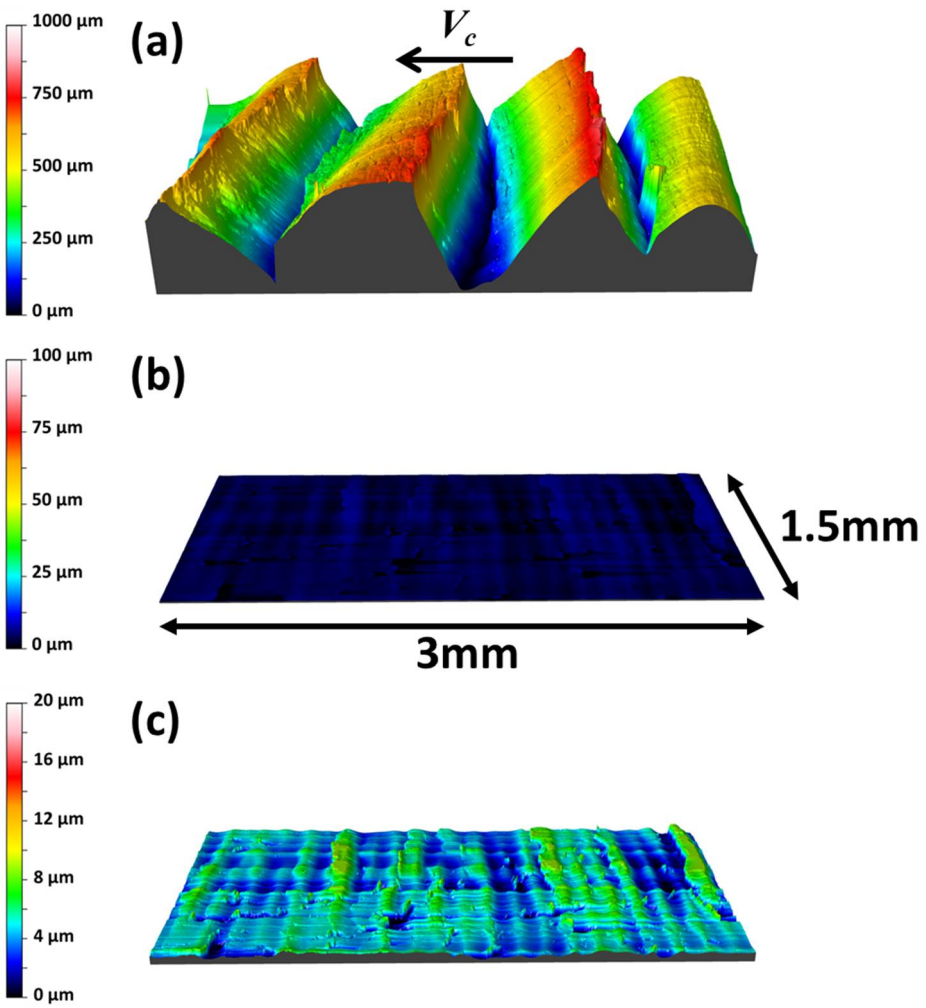

Figure 5-7. Optical profilometry of chip back-surface for cutting brass 360. (a) Profile of FM chip, and profile of HCE chip in (b) 100 µm range, and (c) 20 µm range. Surface profiles are all the same size, 3mm × 1.5mm. Same cutting conditions as Fig. 5-6.

Similar observations were recorded in the ¼ hard brass 260, with segmentation common in FM and the HCE suppressing the segmentation. These results are shown in figure 5-8 and figure 5-9. The segmentation in FM of brass 260 is much less severe than in the brass 360, extending only about 15% into the chip thickness (Fig. 5-9(a)). Whereas in the brass 360, powdery chips result due to the segmentation encompassing the entire chip thickness. This is likely because the brass 260 (¼ hard initial workpiece condition) has greater workability than the brass 360 (1/2 hard

condition). This difference in the extent of the segmentation is also seen in the surface profiles of the back side of the side of the FM chips (Figs. 5-9(c) and (d)). The FM brass 260 chip has a roughness R_z = 107.0 µm which is one-fifth of that of the FM brass360 chip (see Table 5-1). The relative extent of the segmentation and segmentation morphology in FM chips are also clearly seen in the SEM images of the chip back surfaces, from brass 260 and 360, in Fig. 5-10.

The HCE was successful in suppressing the segmentation in the brass 260 enabling continuous strips to be produced (Fig. 5-8(b) and 5-8(d)). Furthermore, the HCE brass 260 strip (back) surface was also much smoother (peak to valley, R_z = 1.4 µm) than the HCE brass 360 strip (R_z~ 7.1 µm). The λ used in the HCE was 1.2 as against a λ value of 1.7 for the FM. The extent of the HCE constraint with the brass 260 was not severe, like with Zn. This is because the segmentation in the FM of brass 260 was not severe, unlike brass 360.

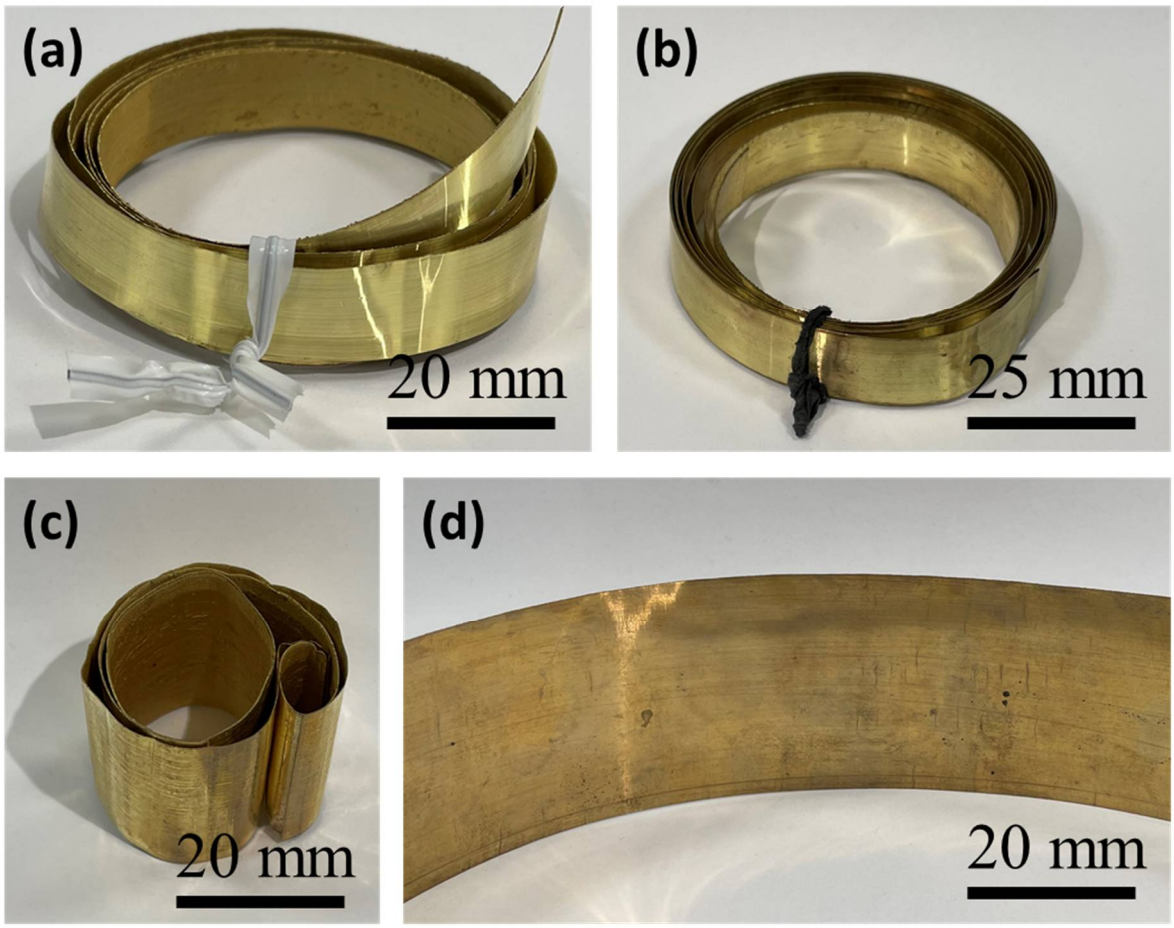

Figure 5-8. Suppression of segmentation in turning of brass 260. (a) and (b) are chips of 10 mm width while (c) and (d) are 48mm wide. (a) and (c) conventional cutting showing segmented chip with rough back-surface. (b) and (d) constrained cutting demonstrating smooth strip surface. Rotary cutting $\alpha = +5°$, $V_0 = 6000$ mm/s, and $t_0 = 250$ μm.

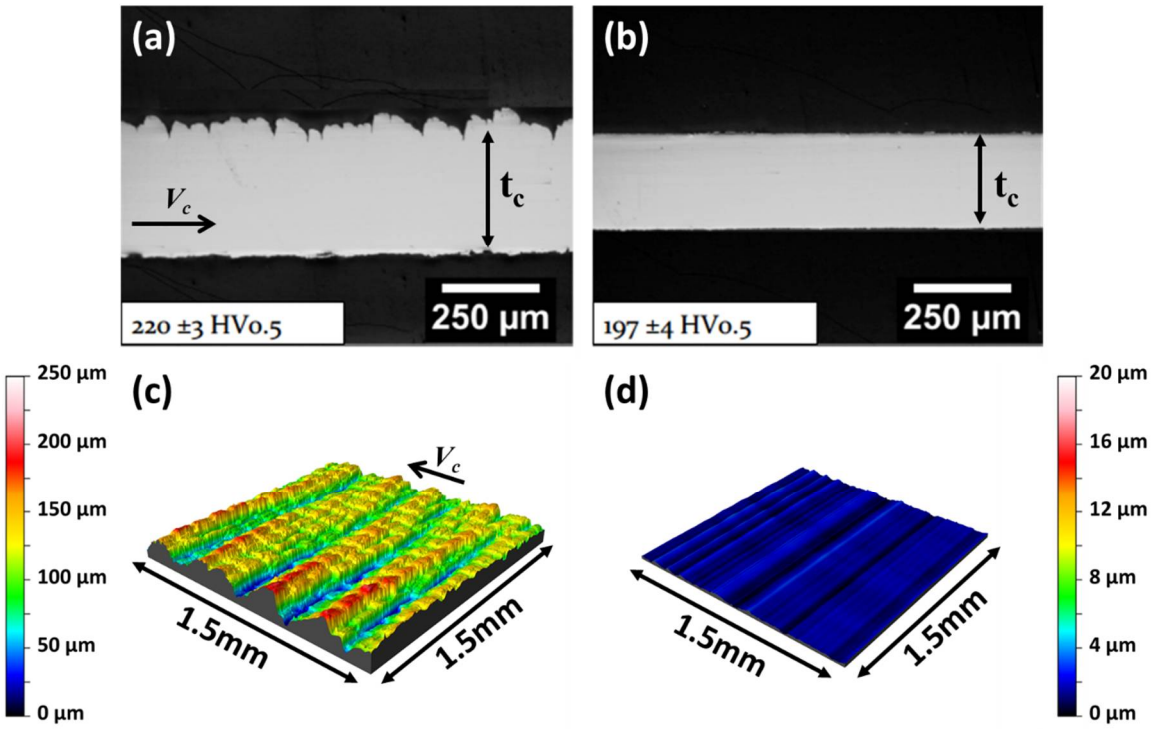

Figure 5-9. Through thickness chip cross section in cutting of brass 260 from (a) FM (λ = 1.7) showing segmentation, and (b) HCE (λ = 1.2) showing uniform thickness and homogeneous structure in strip with smooth surface for cutting of brass 260. Profile of back-surface of (c) FM chip, and (d) HCE chip. Rotary cutting α = +5°, V_0 = 6000 mm/s, and t_0 = 250 µm.

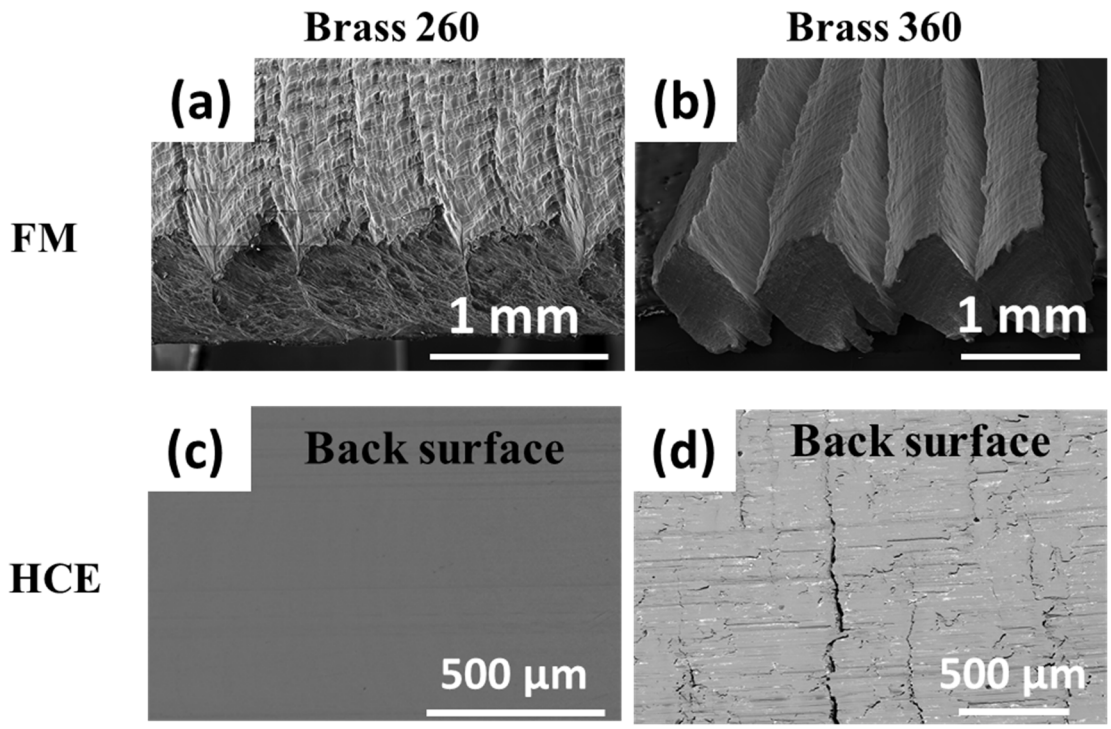

Figure 5-10. SEM images of the chip back surface showing segmentation and suppression of the segmentation at rotary plung cutting. SEM image of chip back-surface from conventional cutting (FM) showing segmentation in (a) brass 260, and (b) brass 360. Strip from hybrid extrusion machining (HCE) showing homogeneous structure for (c) brass 260, and (d) brass 360. Brass 260, cutting conditions: α = +5°, V_0 = 6000 mm/s, and t_0 = 250 µm, same as figure 5-9. Brass 360, cutting conditions: α = +5°, V_0 = 2000 mm/s, and t_0 = 125 µm, same as figure 5-6.

The specific cutting forces (force per unit chip cross-section area) from FM and HCE for the brass 260 and 360 are shown in figure 5-11. The force profiles mirror the segmentation mechanics. The FM specific cutting force for brass 260 (Fig. 5-11(a)) shows high amplitude oscillations similar to the force results presented in figure 4-15. The frequency of the force oscillation is 360 Hz, and correlates with the spatial morphology (frequency) of the chip segments. Furthermore, the HCE specific cutting force for brass 260 is greater than FM specific force, by almost 78%. This is likely due to the additional friction resulting from the strip contact with the constraint die. However, there were no significant force oscillations observed in the HCE consistent with the suppression of the segmentation.

The specific cutting forces for FM and HCE of brass 360 are shown in figure 5-11(b). The FM force again has an oscillatory feature at ~ frequency of 225Hz, which is close to the segmentation frequency of 245 Hz derived from the chip morphology observations. The specific cutting force for the HCE is again larger than the FM cutting force by ~ 63%, due to the additional friction from the constraint die. Furthermore, the HCE force trace also shows an oscillation at ~ 6.2 Hz, which corresponded to the spindle rotation frequency of 375 RPM. Hence, this oscillation has to do with the machine dynamics and not with any chip formation features.

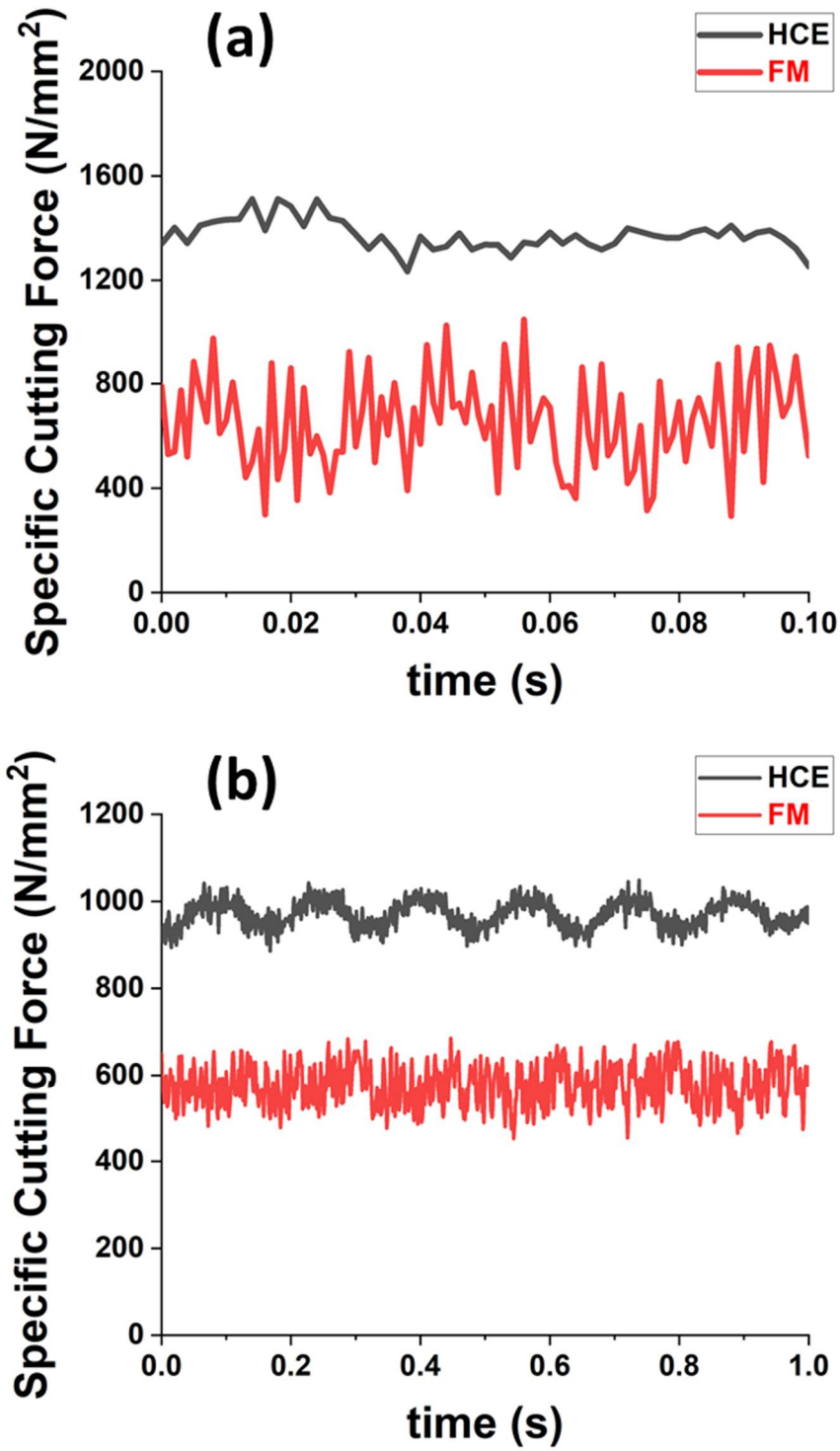

Figure 5-11. Specific cutting force in rotary plung cutting of (a) brass 260, and (b) brass 360. Cutting conditions are the same as in figure 5-10.

The final demonstration of segmentation is with the Si-steel alloy. The results are shown in figure 5-12 and figure 5-13. The FM chip for silicon steel is similar to that of brass 260, with the segmentation extending ~ 25% into the chip thickness. HCE was successful in suppressing the segmentation, see the continuous HCE strip in Fig. 5-13(b). However, since the material has a much higher hardness (240 HV) than the brass 260 (92 HV), the application of the constraint in this case is more demanding requiring also a carbide tool/die. This in turn reflects in a somewhat poorer finish on the HCE chip back-surface (figure 5-12(d) in comparison to that of figure 5-9(d)), see also Table 5-1. However, the peak-to-valley roughness R_z on this back surface is ~ 3 µm for the HCE strip as against an R_z of ~ 115 µm for the FM case. Since the latter reflects the segmentation amplitude, the suppression of the segmentation is quite remarkable as evidenced form the change in the R_z values. Strip widths in the range of 10 to 48 mm have been produced by the HCE, without segmentation, see figure 5-13.

From a practical standpoint, the surface roughness on the HCE strip back surface can be significantly improved even by a light cold-rolling (CR) step following the HCE. This is shown in Fig. 5-13(d) for HCE, where the roughness R_a is seen to decrease from 2.7 µm to 0.8 µm with a cold-rolling reduction of about 30%. Thus, by integrating a light cold-rolling step with the HCE, or even FM, in certain cases, strips of quality comparable to, or even superior to, rolled sheet can be produced. This suggests opportunities for using machining-based chip formation (HCE or FM + CR) as a deformation processing route to produce sheet and strip of commercial widths with further process scale-up.

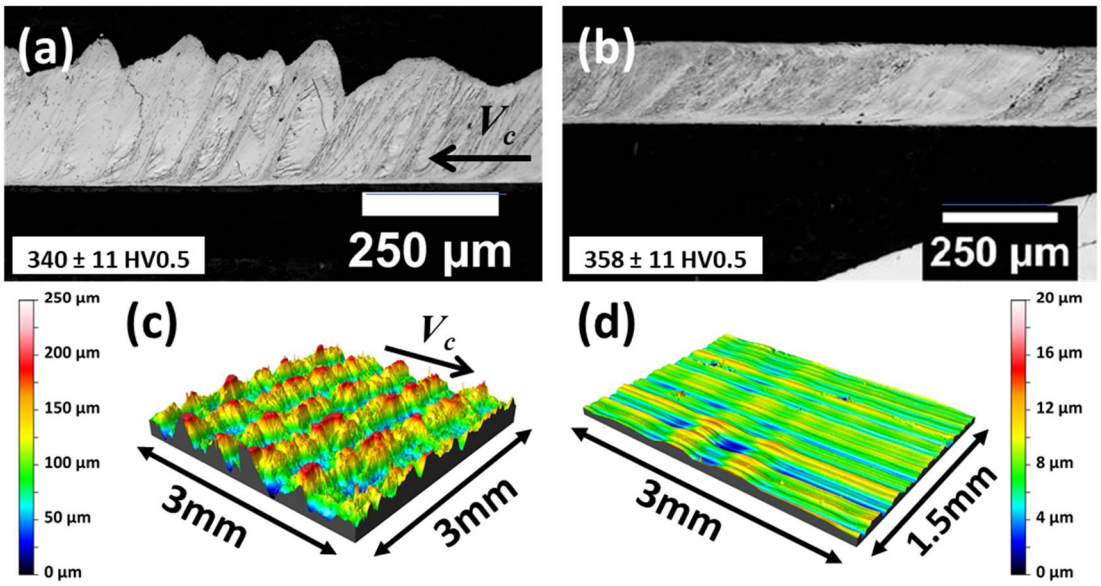

Figure 5-12. Through thickness chip cross section and optical profilometry of FM and HCE of silicon steel. Through thickness chip cross section of (a) FM (λ = 1.8), and (b) HCE (λ = 1.4) strip. Optical 3D profile from back-surface of (c) FM, and (b) HCE strip. Rotary cutting, α = +6°, V_0 = 2000 mm/s, and t_0 = 125 µm.

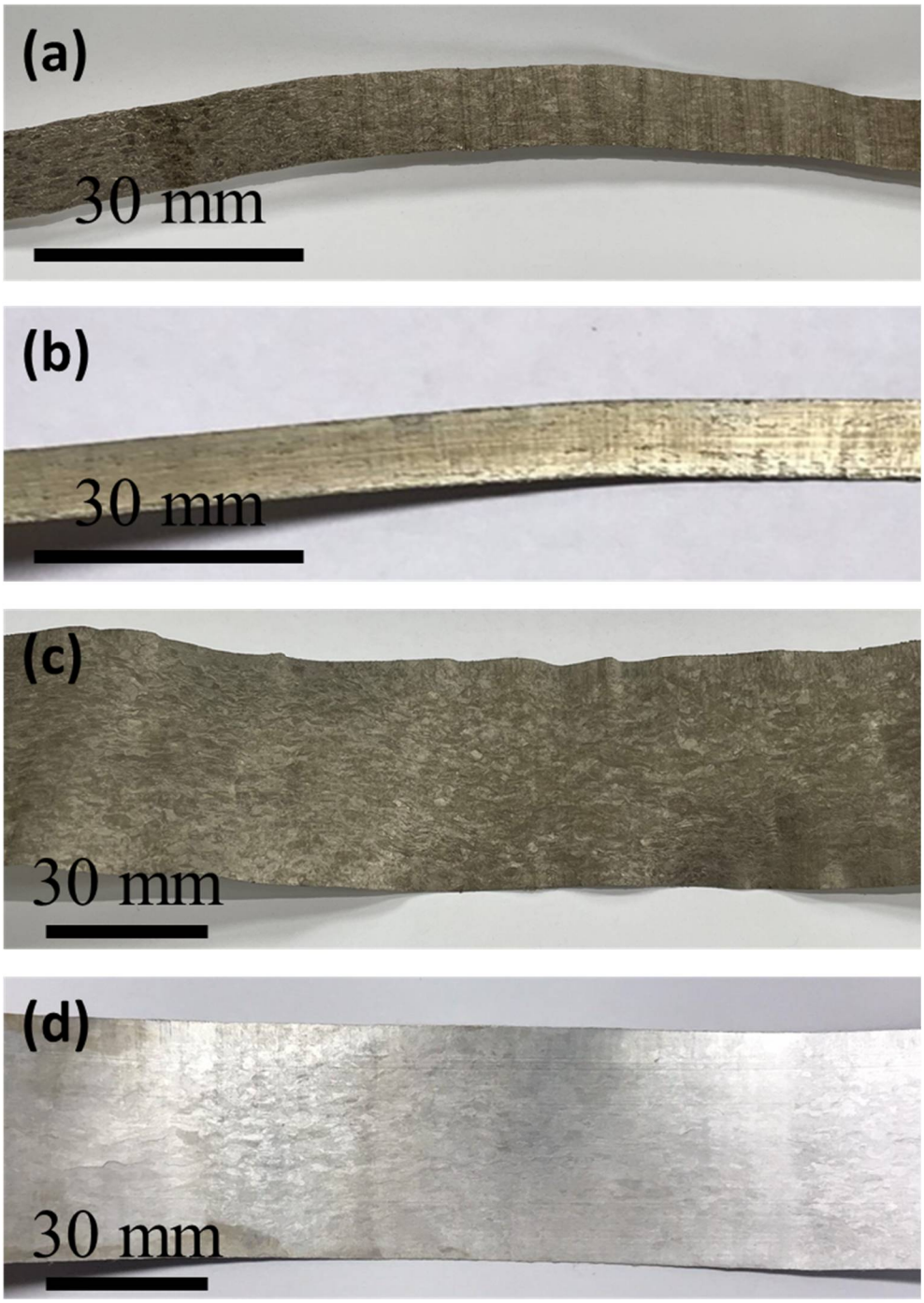

Figure 5-13. Optical image of (a) FM 10 mm wide, (b) HCE 10 mm side, (c) FM 48 mm wide, and (d) HCE + CR 48 mm wide of silicon steel chip. Strip thickness was reduced by 30% through the cold rolling (CR) process, which improved the quality of back-surface of the chip by decreasing roughness. FM and HCE cutting conditions are the same as in figure 5-12.

5.3 Enhancing Segmentation Using a Chemical Medium

We now consider the possibility of inducing segmented chip formation in metals of high workability/ductility that typically do not segment. Our observations of the last chapter suggest that segmentation propensity should be enhanced if the failure (critical) strain is reduced, or the prow strain increased. The former can be influenced by the loading (e.g., hydrostatic tension), material (e.g., reduced workability) or ambient (environmental) conditions. There is no obvious route to creating hydrostatic tension in the prow. Thus, one is led to attempt to consider promoting segmentation by locally embrittling the material in the prow region by use of a suitable environmental medium. This may be done, without altering the workpiece material initial state, by application of chemical media to the WP surface. It is well-known that certain surface-active media can embrittle metals [88], one well-known example being that of Al by Ga. But this liquid metal embrittlement route cannot be used with most machining processes because of its catastrophic nature – the residual "machined surface" would also be severely damaged. However, recent work [9], [89] has shown that a benign, local form of "embrittlement" can be realized by application of common media (inks, adhesives) to the WP surface ahead of the tool. This application limits large-strain deformation (workability) of the metal by effecting a local ductile-to-brittle transition in the cutting zone – a mechanochemical effect.

Figure 5-14 shows the use of this mechanochemical route for effecting segmented chip formation even in a highly workable metal such as (soft) annealed OFHC Cu. In the experiment, one-half of the length of the Cu surface was coated with a common adhesive (Scotch Restickable Glue Stick) while the remaining length was left uncoated (bare). When cutting the bare surface, the chip formed by a highly unsteady mode of flow—sinuous flow—characterized by large-amplitude folding, extensive redundant deformation, and a very thick chip (16-fold thickening, $\varepsilon \sim 4$–8), as highlighted by the streaklines and strain field in Figure 5-14(a). However,

when cutting the glue-coated region, the chip is segmented and much thinner, see Figure 5-14(b), with much smaller chip strain. The cutting forces were also much smaller (up to 80% reduction) than in the sinuous flow case. Concurrently, the cut-surface quality, as characterized by roughness and defects (e.g., tears, pull-outs), was also much improved, by an order of magnitude compared to the sinuous-flow cutting [89]. The segmented-chip evolution exhibited all the key characteristics of segmentation observed earlier – prow formation, nucleation of prow-crack, and prow-crack propagation towards tool tip. Segmentation was again initiated by fracture occurring in a prow-fold. This mechanochemical effect, relatively material-agnostic, has been successful at effecting segmented chip formation in highly workable metals like Al, Fe and Ni — a consequence of reduction in failure strain in vicinity of notches (folds) in the prow. The results attest also to potential benefits of segmented-chip formation, *viz.* smaller forces and better surface quality, than the type 1 chip with sinuous flow.

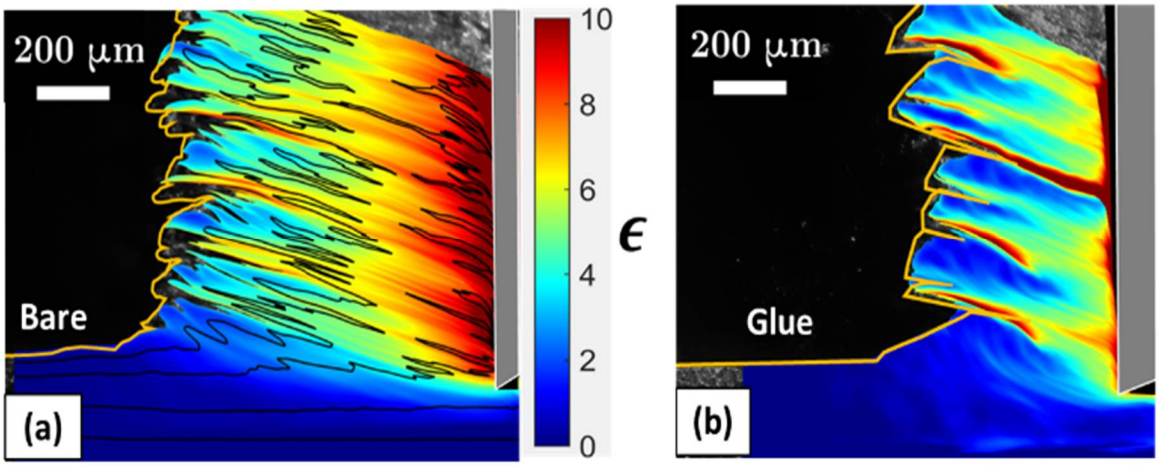

Figure 5-14. Inducing segmentation in cutting of ductile (annealed) Cu via application of chemical medium (glue) to workpiece surface – the mechanochemical effect. The flow attributes in the chip are depicted using strain fields and streaklines. (a) Cutting without medium application showing sinuous flow with folding and extensive redundant deformation; and (b) cutting with medium application which results in segmented flow. Linear cutting, $\alpha = 0°$, $V_0 = 2$ mm/s, $t_0 = 50$ μm.

Table 5-1. Summary of the roughness results for rotary cutting chips.

Material	α (°)	V_0 (mm/s)	t_0 (μm)	Average chip thickness ratio, λ	Chip width, w (mm)	S_a (μm)	S_q (μm)	R_a (μm)	R_z (μm)
Zn (FM)	5	500	250	2.2	3.2	23.4	29.9	26.4	185.5
Zn (HCE)	5	500	250	1.3	3.2	0.7	0.9	0.7	3.2
Brass 360 (FM)	5	2000	125		6.35	143.7	174.9	132.9	509.7
Brass 360 (HCE)	5	2000	125	1.7	6.35	1.3	1.6	1.7	7.1
Brass 260 (FM)	5	6000	250	1.7	6.35-48	24.9	31.4	22.2	107.0
Brass 260 (HCE)	5	6000	250	1.2	6.35-48	0.4	0.6	0.8	1.4
Si-steel (FM)	6	2000	125	1.8	6.35-48	32.5	40.2	30.9	115.2
Si-steel (HCE)	6	2000	125	1.4	6.35-48	1.7	2.3	2.7	3.0

6. MG AZ31B AND WOODS METAL

We have studied segmentation in 2 other material systems: Mg AZ31B and Woods metal (Woods metal is a low melting-point alloy, T_m = 70 °C). Both alloys are known to have limited workability and well-known for producing a saw-tooth chip [90], [91]. The occurrence of the saw-tooth chip indicates that segmentation is likely the dominant mode of chip formation. However, we report and discuss these results separately since there are important differences in the evolution of the segmented flow.

6.1 Flow Dynamics

Selected frames from a high-speed sequence (1000 frames per second) of cutting of Mg AZ31B are shown in figure 6-1. Frame 1 shows start of formation of a new segment. There are several high points on workpiece surface behind the cutting tool resulting from previously formed segments (orange circles). Frame 2 shows occurrence of microcracked region near the tool-tip. This region then extends to the free (back) surface of the chip/workpiece causing the segmentation, see frames 3 and 4. The blue arrow in frame 3 points to the segmentation line/interface, and emergence of the fracture to the free surface. Frame 4 depicts rigid body motion of the just-formed segment along the tool rake face, this motion causing separation of the segment from the rest of the workpiece. As a consequence of this segmentation, a high point is seen to occur on the cut surface of workpiece, see at orange circle in frame 4. The growth speed of the microcracked region during the first half of the segmentation cycle (frames 1 and 2) is ~ 3.5 mm/s, is close to the deformation rate V_0 = 3 mm/s. But propagation speed of the fracture after frame 2 could not be accurately estimated at the frame rate used, with the crack reaching the surface quite rapidly (> 145 mm/s). The segmentation in the Mg alloy, driven by microcracking at the tool tip, is

fundamentally different from the previously shown examples in Zn, brass, and Si-steel. In these latter instances, the segmentation was triggered by a crack forming at the prow surface and then propagating inwards towards the tool tip.

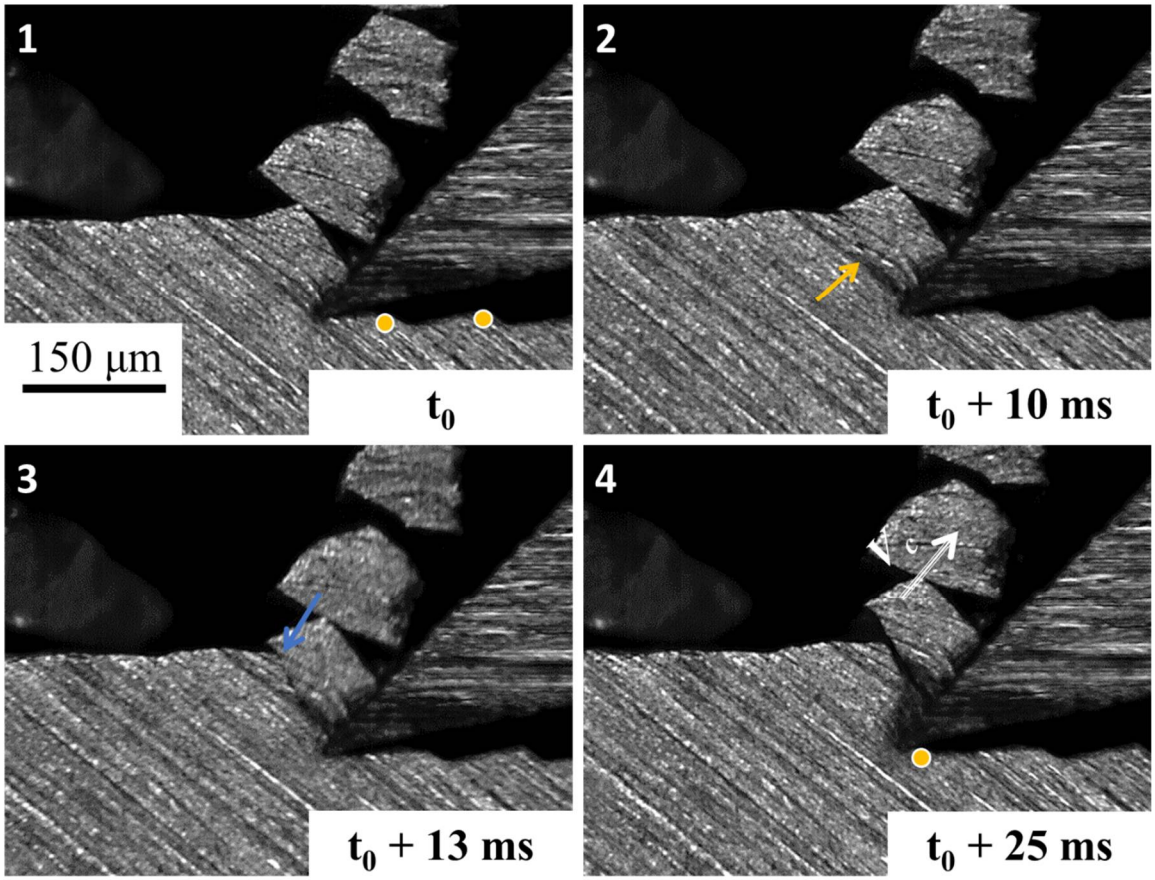

Figure 6-1. Four frames from a high-speed image sequence of cutting of Mg alloy showing microcrack initiation from tool rake face (orange arrow) and propagation of fracture to the free surface of the workpiece/chip. This results in segment formation (blue arrow). Orange circles on cut surface demarcate location of high points on workpiece surface, each arise from a segmentation event. Mg AZ31B, α = +40°, V_0 = 3 mm/s, t_0 = 100 μm.

We now turn to cutting of Woods metal with a tool of α = +20°, see Fig. 6-2. Frame 1 in the figure shows formation of a prow ahead of the advancing tool (like in Zn), and nucleation of a surface crack (red arrow) on the prow surface ahead of the tool. As this surface crack starts growing inward towards the tool tip (blue arrow in frame 2), a microcracked region is seen to occur at the

tool tip (orange arrow). In frame 3, the microcracked region is seen to have grown rapidly to the free surface forming a second segmentation line (lower blue arrow) that does not quite meet the first segmentation line (upper blue arrow) that has developed inwards from the prow surface. It appears that the segmentation surface triggered by the prow surface crack acts like a “free surface” towards which the microcracking-triggered (lower) segment advances. From this point onward, the segmentation due to the microcracked region (bottom blue arrow) stays active while the segmentation due to the prow surface crack (top blue arrow) becomes dormant. Frame 4 shows rigid body motion of chip along tool rake face, even as the microcracking-driven continues. From these preliminary observations, it appears that the segmentation process in cutting of Woods metal is based on a competition between the prow surface cracking and microcracking at the tool tip. The evolution of the segment regions due to the surface cracking is towards the tool tip, following the same pattern as that observed in Zn, brass, and Si-steel. Whereas, the segmentation driven by the tool microcracking evolves similar to the segmentation in cutting of Mg AZ31B. The prow surface crack driven segmentation has an average speed of 2.9 mm/s, close to the deformation rate of V_0 = 3 mm/s. Likewise, the microcracked region at the incipient stage grows at a rate of 3.3 mm/s, which is also close to V_0. But the final stage of growth of the microcracked region to the free surface is significantly faster (> 70 mm/s) as in the Mg alloy.

It is clear from these observations that both the Mg alloy and the Woods metal segment even when cutting is done at large positive rake angles (>= 20 degrees). Furthermore, the segmentation is quite severe, extending from 50 to 100% of the chip thickness, at these positive rake angles. They point to the very low workability of these metals under conditions of deformation processing.

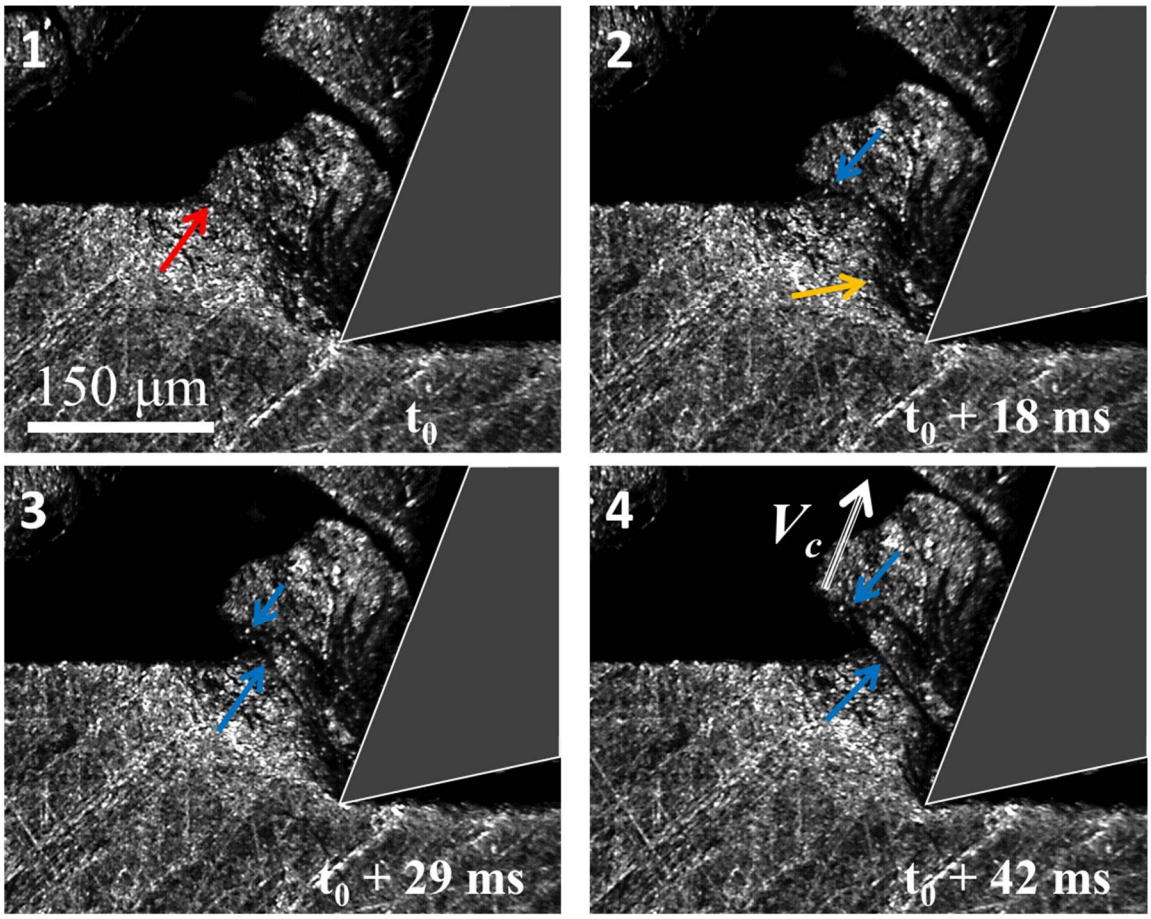

Figure 6-2. Four frames from high-speed image sequence of cutting of Woods metal. Both crack initiation from free surface (red arrow) and microcrack initiation from rake face of the tool (orange arrow) drive the segmentation. α = +20°, V_0 = 3 mm/s, t_0 = 120 μm.

The strain and strain rate fields for cutting of Mg AZ31B and Woods metal are shown in figure 6-3. The strain field in Mg AZ31B shows a distinct concentration of strain at the base of the segmentation zone near the tool tip, where the microcracking is first observed (Fig. 6-3 a, see also at orange arrow). On the other hand, the strain field in the Woods metal cutting shows 2 bands of high strain (Fig. 6-3c). The first band demarcated by red arrow arises from the prow surface cracking, while the second band (orange arrow) is due to the microcracking near the tool tip. The strain field in the chip is quite non-homogeneous in both of these metals, varying between 0.5 and

3.7 in the Mg alloy, and between 1.1 and 3.8 in the Woods metal. The volume averaged strain is 1.7 ± 0.2 in the Mg AZ31B and 3.2 ± 0.2 in the Woods metal.

The strain rate field in the two alloys is concentrated in narrow zones (analogous to shear planes) that are aligned with the orientation of the microcracked regions rather than the free-surface crack (Figs. 6-3 b and d). The strain rates in these narrow deformation zones are ~ 50/sec, much higher than in the Zn (~ 10/sec) and brass (20-25/sec); compare figure 6-3 with Figs. 4-2 4-8, and 4-10, strain rate plot in cutting of Zn, brass 360, and brass 260, respectively. Note however that Zn does not segment when cut with a tool of α = +20°; and cutting of brass 260 with a tool of rake angle +20° results in segmentation that extends to less than 15% of chip thickness [17]. However, the segmentation is quite severe in cutting of Mg AZ31B and Woods metal even with tools of large positive rake angle, α = +40° and α = +20°, respectively.

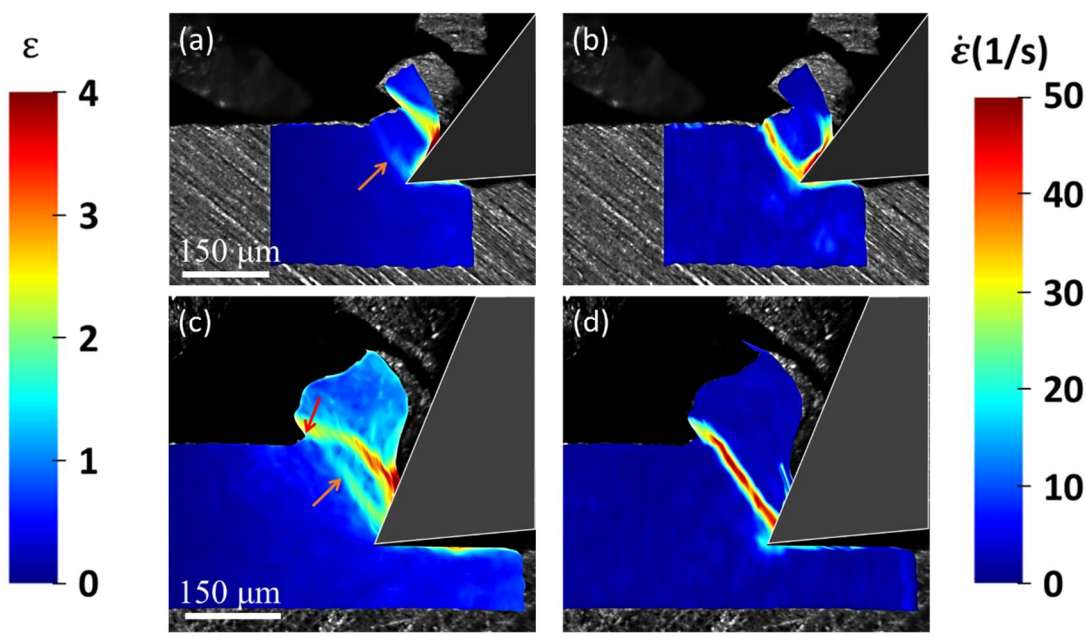

Figure 6-3. Strain and strain rate fields in segmented cutting of Mg alloy and Woods metal. (a) and (b) Mg AZ31B with tool of α = +40°; (c) and (d) Woods metal with tool of α = +20°. Microcracking and surface crack regions are shown at orange and red arrows, respectively. Frames selected from the same cutting experiments shown in figure 6-1 and figure 6-2.

In summary, we have discussed observations of the segmentation flow dynamics in the Mg AZ31B and Woods metal. The observations show that microcracking from the tool tip region plays a major role in the nucleation and development of segmentation in these material systems.

6.2 Morphology and Cutting Forces

Optical profilometry traces of the free (back) surface of the segmented chips are shown in figure 6-4(a) and 6-4(b), respectively for Mg AZ31B and Woods metal. In the Mg AZ31B, the segments are seen to run straight across the width of the chip. Based on the wavelength/pitch (p) and amplitude (p_c) of the chip segments, and $\lambda = \frac{p}{p_c}$ (equation 4-1), the segmentation frequency is estimated at ~ 23 Hz. The corresponding force shows an oscillation with frequency of 22 Hz that clearly is due to the segmentation (figure 6-4(d), black trace). The cut workpiece surface with the Mg AZ31B, see figure 6-4(c), also has roughness features consistent with the segmentation profile; see chip segmentation topography figures in 6-4a and b, and also occurrence of high points on cut workpiece surface in figure 6-1.

The segmentation features in the chip with the Woods metal, while mostly straight, do show some meandering across the chip width (figure 6-4(b)). The force trace shows a definite oscillation with frequency of 16 Hz (figure 6-4(d), red trace), arising most likely from the segmentation. It is worth noting that the segmentation in this metal involves a competition between microcracking and surface cracking (figure 6-2). As a result, the formation and growth of microcracks, and associated segmentation, causes the force oscillation. While the segmentation part arising from the surface cracks, may be contributing to their meandering nature.

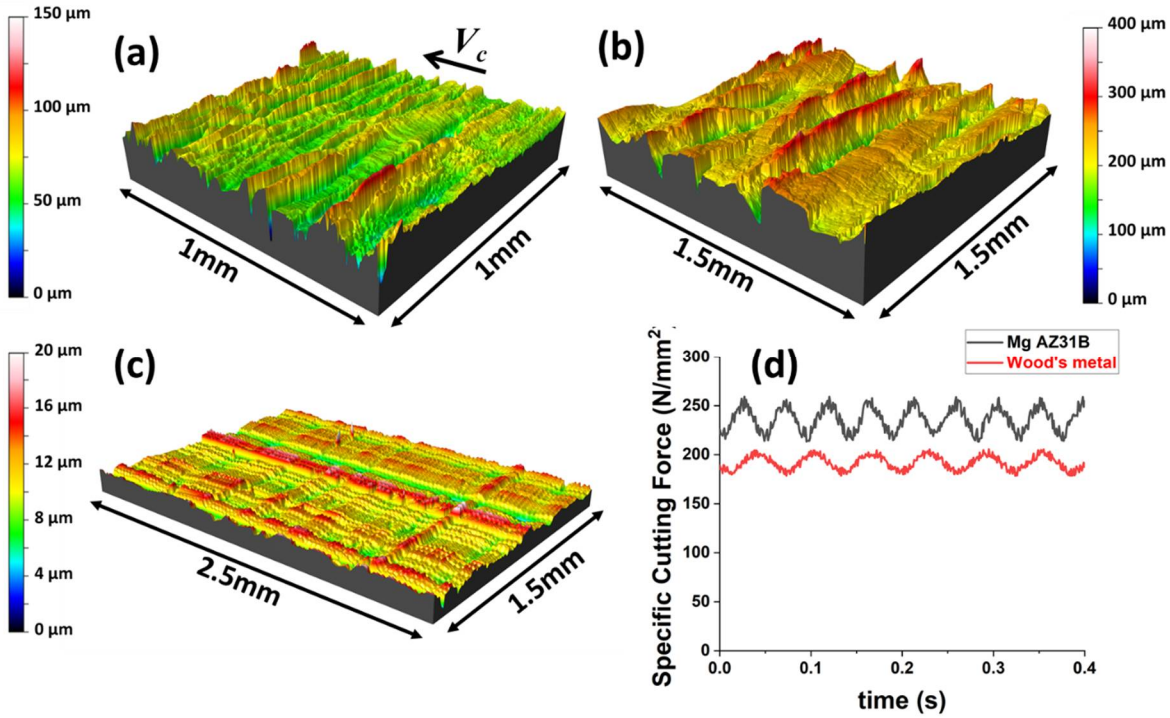

Figure 6-4. Optical profilometry and forces in cutting of Mg alloy and Woods metal. a) Mg AZ31B chip profile, α = +40°, V_0 = 3 mm/s, and t_0 = 100 µm, and (b) Woods metal chip profile, α = +20°, V_0 = 3 mm/s, and t_0 = 120 µm. (c) Profile of cut workpiece surface of Mg AZ31B. (d) Specific cutting force traces showing oscillation related to segmentation.

6.3 Control

We attempted to suppress the segmentation in the Woods metal and Mg alloy using constrained cutting by HCE, analogous to what was done with Zn, Brass, and Si-steel. Note however the nature of the segmentation in these alloys is triggered mainly by tool tip microcracking. There is significant body of work done on successful suppression of flow localization in magnesium by HCE from our group [92], [93]. Hence, here we focus on possibility of producing a type 2 (laminar flow) chip/strip in Woods metal by HCE.

Figure 6-5 shows successful suppression of the segmentation in Woods metal by HCE. The chip flow is seen to be uniform (laminar) with smooth streaklines (Fig 6-5a). These streaklines are very similar to those in figure 5-2(c) from HCE of zinc. The strain field presented in figure 6-5(b)

also shows homogeneous deformation over most of the strip volume (thickness), except for thin zones of strain concentration adjoining the tool/die faces due to frictional secondary deformation. The specific cutting force for FM and HCE of Woods metal is shown in figure 6-5(c) for $\alpha = 0°$. The HCE force is seen to be constant with an average value of 405 N/mm^2. This force is greater than the average force in FM by ~ 32%. However, the FM force shows the usual oscillations at the segmentation frequency.

We can also make a comparison of the FM forces for $\alpha = 0°$ (fig. 6-5 c) and $\alpha = +20°$ (figure 6-4(d)). The average specific cutting force is higher (305 N/mm^2) for the FM at $\alpha = 0°$, in comparison to that (195 N/mm^2) for $\alpha = +20°$ (figure 6-4(d)). Also, the oscillation frequency of 18 Hz observed in the specific cutting force for $\alpha = 0°$ is somewhat higher than that (~ 16 Hz) for $\alpha = +20°$. Both of these observations are quite consistent with the cutting mechanics of segmentation and underlying deformation.

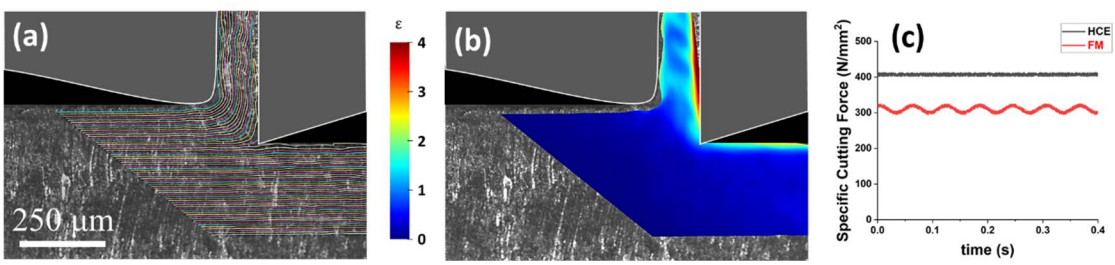

Figure 6-5. Suppressing segmentation by HCE in Woods metal: (a) streakline pattern, and (b) strain field. (c) Specific cutting force for FM ($\lambda = 1.5$) and HCE ($\lambda = 1.3$) at the same cutting conditions. Linear cutting, $\alpha = 0°$, $V_0 = 3$ mm/s, and $t_0 = 100$ µm.

In summary, we have demonstrated that microcracking from tool tip controls the flow dynamics of segment formation in cutting of Mg AZ31B and Woods metal. Force oscillations occur in both cases closely correlated with the segmentation process. Lastly, suppression of the segmentation by the HCE was achieved, resulting in formation of strip of uniform thickness and with uniform (homogeneous) deformation. The corresponding cutting force profiles in the HCE

were also constant and without any oscillations. Interestingly, HCE appears to be able to suppress segmentation, irrespective of whether it is initiated from the free surface of the workpiece/chip in or at the tool tip.

7. SOME OBSERVATIONS ABOUT ROLE OF MICROSTRUCTURE IN SEGMENTATION

In this chapter, we present some exploratory observations about the possible role of grain boundaries in influencing the deformation in cutting, and segmentation. The motivation for this exploration is related to observations that surface folding in deformation of polycrystalline metals during sliding and cutting has a microstructure origin [8] – grain-to-grain variation in flow stress, and differential deformation of surface grains due to their varying orientations.

To study, the role of grain boundaries we use *in situ* imaging of the cutting process but with the workpiece alloys thermally etched (prior to the cutting) to reveal the grain boundaries. Thermal etching involves annealing of the material in a controlled temperature and atmosphere, to reveal grain boundaries by differential displacements [94], [95]. This technique is well-developed for specific alloy systems. In the present case, since the segmentation process in cutting is of interest, we select workpiece material systems that can be thermally etched; and that can easily segment (e.g., Ti6Al4V) or wherein segmentation can be induced by some parametric influence (e.g., mechanochemical effect in Cu, deformation geometry). In the present exploratory study, we use thermally etched Cu and Ti6Al4V to record the segmentation process via *in situ* imaging techniques. More information on thermal etching procedures used to reveal the microstructure of the Cu and Ti alloy is given in Appendix B.

The specific experimental approaches were as follows. The use of a surface film to locally embrittle a workpiece surface and promote segmentation in cutting (mechanochemical effect) was the approach used with annealed Cu (thermally etched). In this case, as we have seen, segmentation is triggered by a crack nucleating in the chip-formation deformation zone (and prow region) on the free surface of the workpiece/chip ahead of the tool. The specific knowledge about the

segmentation location is useful for determining which part of the workpiece should be imaged. On the other hand, in cutting of Ti6Al4V, segmentation is triggered by microcracking at the tool tip, as in the MgAZ31B and Woods metal; the crack thus nucleated propagates to the free surface of the chip/workpiece. We utilize the high-speed imaging to examine the crack initiation, and its relation to grain level features; and subsequent development of the segmentation.

7.1 Segmentation from Free Surface Cracking

A thermally etched sample of OFHC copper was prepared with an average grain size of 460 µm. A thin film of ink was applied to the workpiece surface using a Sharpie marker. Cutting of this Cu workpiece was done with a high speed steel tool at low speed, and the deformation/segmentation was recorded using the high-speed camera setup. Figure 7-1 shows four frames from cutting of the thermally etched copper. Frame 1 shows a previously formed surface crack/segment A (blue arrow) in the chip, and a grain boundary B (white arrow) located ahead of the advancing tool. In Frame 2, the grain boundary B enters the prow region. A crack is now initiated at the surface of the prow. The location of this crack is coincident with the grain boundary B. Frame 3 shows that the crack at grain boundary B has propagated inwards towards the tool tip, resulting in segmentation. In the same frame, a new grain boundary C has just reached the prow region. A crack is now triggered on the prow surface at this boundary C. Frame 4 shows development of this crack as before, inwards towards the tool tip, with a new segment resulting. These observations suggest that the nucleation of the segmentation process is strongly influenced by the grain boundaries, with the boundaries serving as crack nucleation locations in the prow region. Of course, in this case, the ink film plays a role also in the triggering of the segmentation process. It is quite possible that the embrittling effect of the ink is more pronounced at the grain boundaries. The exploratory observations point to grain boundaries as sites for surface cracking.

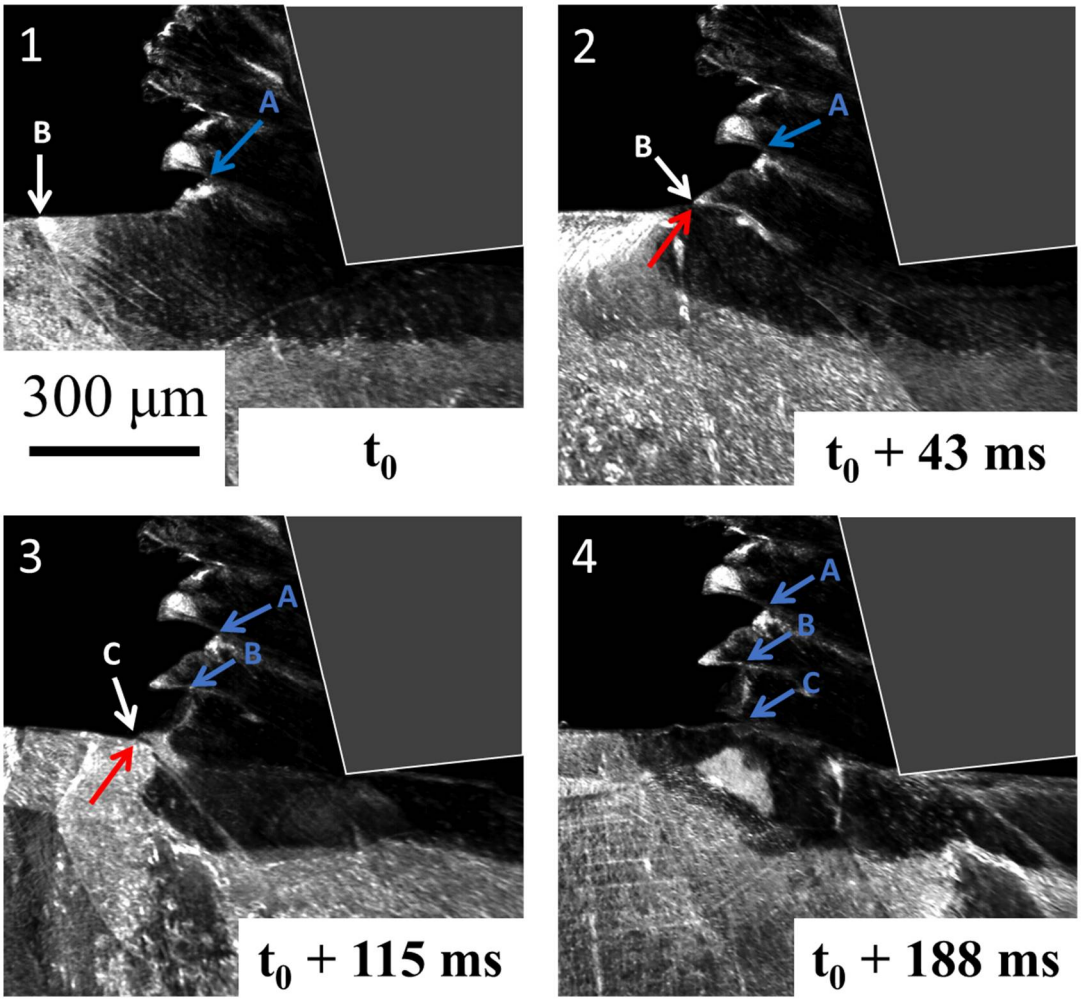

Figure 7-1. Four frames from a high-speed image sequence showing segmentation in cutting of annealed Cu coated with an ink film. The copper is thermally etched to reveal the grain level structure. White arrows show location of specific grain boundaries. Red arrows show surface crack nucleation points, and blue arrows show location of crack tip after the surface crack has propagated. This propagation of the surface crack results in segmentation. α = -10°, V_0 = 3 mm/s, t_0 = 90 µm.

7.2 Segmentation from Microcracking at Tool Tip

The triggering of segmentation by microcracking at the tool tip has been observed in alloys such as Mg AZ31B and Woods metal. It also occurs in Ti6Al4V. We used the Ti alloy to study this type of segmentation and its relation to microstructure since Ti6Al4V can be thermally etched

to reveal the microstructure. We are able to thermally etch Ti6Al4V to make the microstructure visible, see Figure 7-2. The grain size in this alloy was ~ 330 µm.

The cutting of Ti6Al4V resulted in segmented flow as seen in figure 7-2. Frame 1 shows grain A, outlined by red dashed line; the two white arrows show the intersection of the grain boundary with the free surface. In Frame 2, the grain A is nearing the tool tip; concomitantly, a microcracked region forms at the tool tip (yellow arrow) but away from the grain boundary. Frame 3 shows development of this microcracked region towards the free surface. At this stage, the grain A has advanced into the microcracked region with the bottom part of the grain about to be cut into two parts by the microcrack. Frame 4 shows further development of the segment at blue arrow with the crack propagating through the grain. In this case, the segmentation development occurs between the grain boundaries and through the grain. The feature of this segmented chip formation is crack initiation from the tool tip, at rake face of the tool, and growth of this crack towards the free surface of workpiece/chip intersection region. This development of the segmentation appears to be not influenced by the grain boundaries.

These exploratory observations suggest opportunities for using the approach of *in situ* imaging of cutting of thermally etched metal alloy samples to study deformation and flow phenomena in cutting like segmentation, shear banding and sinuous flow.

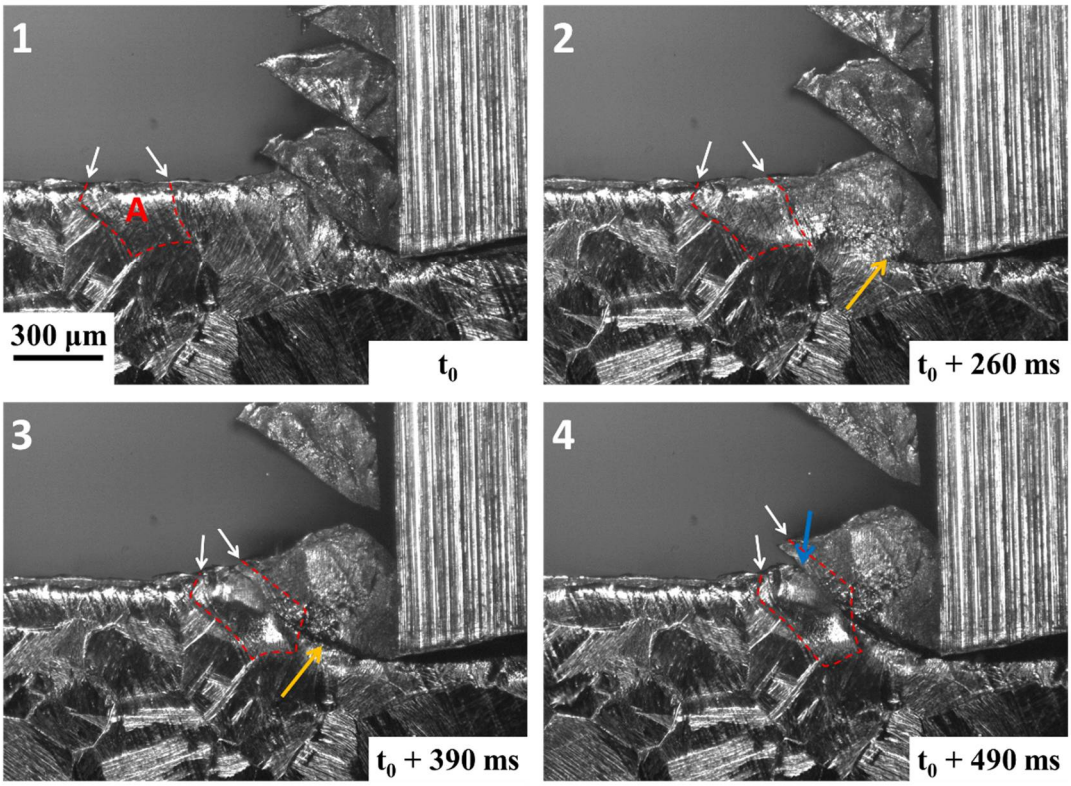

Figure 7-2. Four frames from high-speed image sequence showing segmentation in cutting of thermally etched Ti6Al4V. Dashed red line demarcates boundary of grain A. White arrows show where grain boundary reaches the free surface. Yellow arrow shows the microcracked region. Blue arrow shows the boundary of segmentation, $\alpha = 0°$, $V_0 = 1$ mm/s, $t_0 = 200$ µm.

8. DISCUSSION

A study has been made of the deformation mechanics of segmented chip formation (type 3 chip, Fig. 1-3), one of the principal types of chip formation, and the underlying plastic flow field. By using high-speed *in situ* imaging, at high resolution, and image correlation analysis (Fig. 3-1); complemented by force measurement and chip/workpiece surface topography characterization, we have characterized the plastic flow and fracture underlying the segmentation process in a range of metal alloys.

The imaging has enabled details of how the flow field triggers fracture events in the deformation zone of chip formation on the chip/workpiece surface ahead of the advancing tool. Propagation of these fractures towards the tool tip, leads to the characteristic saw-tooth morphology of the segmented chip. With minor exception, the *in situ* observations have confirmed, by direct observational evidence, a hypothesis due to Nakayama [5] and Shaw [13] that segmentation is initiated from the back (free) surface of the chip. This was observed in cutting of Zn (Fig. 4-1), brass 260 (Fig. 4-9) and 360 (Fig. 4-6) alloys, and Fe-4%Si-4%Cr (Fig. 4-11) electrical steel. Measurements of the strain field suggest that the free-surface crack which triggers the segmentation process is nucleated at a critical strain value, this strain value being relatively independent of the deformation zone geometry (Fig. 4-13). Segmented chip formation is thus shown to arise from a ductile fracture process that is strain-controlled – perhaps, the simplest version of the Cockroft-Latham failure theory [61] that is based on damage accumulation during plastic deformation.

The segmented chip morphology is found to be of two types (Fig. 4-16): 1) first, wherein the segmentation runs straight across the chip width, that suggests the fracture nucleation is occurring at the same time all across the width. In this case, the segments create a series of parallel

grooves that are parallel to the chip width, but spaced apart with some regularity along the chip length; and 2) second, wherein the segmentation meanders across the chip width; in this case the back surface of the chip has less pronounced grooving. The force profile signatures are significantly influenced by the segmentation morphology. The “straight-across-the-width” segments give rise to characteristic oscillations in the force profile, the frequency of the oscillations matching the segmentation frequency (Fig. 4-15). This oscillation in the force profile is consistent with periodic loading/unloading of the deformation all across the chip width triggered by the free-surface crack formation. Whereas with the meandering segmentation, the aggregate of multiple loading/unloading events at different width locations, all of which are not synchronized in time, leads to a more diffuse, and steady, force profile without significant force oscillations. These correlated observations of segmentation morphology (Fig. 4-17) and force profiles (Fig. 4-15) indicates that contrary to current understanding, the occurrence of segmentation need not always result in force oscillations. Only one type of segmentation morphology, the straight-type, should cause force oscillations. Furthermore, even when the force oscillations occur, it is only in extreme cases of segmentation, where this segmentation encompasses much of the chip thickness, does one see striation marks on the machined workpiece surface. The observed localization of the plastic deformation in segmented chip formation is also likely to be beneficial from an energy standpoint in terms of the material removal process. In fact, we have seen this in the much lower chip strain (volume averaged value) of the segmented chip compared to the more uniform-flow chip formation.

The stress and strain states in segmented chip formation provide a framework in which to examine some current theories of ductile fracture in metals [47], [61], [66]. While the observations are broadly consistent with hydrostatic pressure being of benefit in terms of postponing crack nucleation, the more quantitative predictions of these theories which invoke stress triaxiality as an

important parameter [66] were not found to hold up. The latter was established based on considerations of the stress state in the prow zone ahead of the tool where the segmentation cracking was observed to nucleate. The onset of segmentation at a critical value of strain is intriguing (Table 4-1). For it suggests, that in deformation processing, this may be a worthwhile framework in which to examine failure in conjunction with the hydrostatic stress state. More generally, the segmentation ductile failure suggests that the cutting framework may be a useful one in which to examine ductile fracture of metals especially for processes involving large-strain deformation.

Analogous to shear banding, it was found that while the crack nucleation triggering the segmentation may be very fast (sub-microsecond), the propagation of the crack towards the tool tip occurs essentially at the same speed as the rate of tool advance, that is the loading or deformation rate. It is likely, that as with shear banding, the strain localization along segment interfaces (crack locations) may also develop just preceding the crack propagation phase. It should be noted though that while both the shear-banded chip (type 4) and the segmented chip (type 3) show very similar saw-tooth morphology (see Fig. 1-2), the underlying mechanics is quite different. Ductile fracture plays a dominant role in segmentation, while severe flow localization drives shear banding often without any fracture.

An exploratory attempt (Figs. 7-1 and 7-2) was made using cutting of thermally etched work piece samples and *in situ* observations of the deformation to examine the role of material microstructure in influencing the segmentation process. While less than conclusive, the observations did show nucleation of the segmentation cracking in some instances to occur at grain boundaries. However, in these cases, since the segmentation was triggered by local material

embrittlement at the surface by an ink film, the possibility exists that the embrittlement was more localized at the grain boundary.

With some metals such as MgAZ31B (Fig. 6-1) and Woods metal (Fig. 6-2), microcracks that formed near the tool tip caused the segmentation, rather than free-surface cracking. We do not as of yet have a clear picture of this segmentation mode. This is an aspect that should be considered in the future.

Our phenomenological understanding of the segmentation mechanics, has enabled methods to control the segmentation process. By changing the hydrostatic stress state (increasing the pressure) at the prow surface and constraining the deformation/fracture process driving the segmentation, it was possible to produce continuous strips (chips) with homogeneous deformation; the underlying flow in these cases was also uniform and steady (laminar). This was done by application of a second die across from the primary cutting tool to constrain the chip-geometry at the exit of the deformation zone (Fig. 5-1). The constrained cutting process involves combined cutting and extrusion and is hence called Hybrid Cutting Extrusion (HCE). HCE thus suggests itself as a deformation processing method that can be used to produce metal alloys in sheet, strip and foil forms in a single deformation step. This is to be contrasted with conventional rolling processes to make sheet, all of which involve highly, energy-intensive, multistep deformation processing with large infrastructure. Furthermore, the HCE by suppressing segmentation and confining the deformation offers opportunities for sheet processing with low-workability alloys with minimal or no workpiece pre-heating in contrast to rolling. In rolling, the many stages of workpiece heating to effect hot rolling or restore material ductility between cold rolling steps, coupled with the frictional energy losses that compound with the number of rolling steps, are the principal reasons for the very high specific energy. In contrast, the single-step HCE, even though

it involves higher chip formation forces than conventional machining due to the friction from the constraining die, is expected to be significantly more energy efficient than rolling because it involves only one deformation step. Our work has also shown that HCE can produce strip and foil with surface finish comparable to or superior to rolling (Figs. 5-3 to 5-10).

We have also demonstrated that by locally embrittling the workpiece surface in the deformation zone, we can skew the cutting-deformation process the other way – that is effect segmentation in very ductile metals like OFHC copper that have rarely, if at all, been observed to segment (Fig. 5-14). This demonstrates another aspect of segmentation control – enhancing segmentation by local surface embrittlement by means of a surface-active medium. In this case, the medium very likely lowers the fracture strain of the material at the surface enabling ductile failure. This approach may be of value for cutting metal alloys such as pure Al, austenitic stainless steels, Ta, Nb and even Ni, all of which though relatively soft, are quite ductile and/or undergo significant strain hardening, earning them the name “gummy”. Furthermore, the occurrence of ductile fracture/segmentation in the presence of surface media points to the possibility of using the cutting process to study environmentally-assisted cracking phenomena in metals.

9. CONCLUSIONS

The mechanics of segmented chip formation in cutting of metals has been studied using high-speed *in situ* imaging, complemented by force and surface topography characterization, in a range of metals. The principal findings are as follows.

a) Segmentation is shown to initiate on the free surface of the workpiece/chip in the prow region ahead of the advancing tool. The initiation is triggered by a surface crack that forms and propagates towards the tool tip at a speed similar to that of the deformation rate. Different levels of segmentation occur depending on the extent of the crack propagation towards the tool tip.

b) The surface crack nucleation has been observed to occur at a critical value of the strain. Typically, this is in the range of 0.7 to 1.3 for the different metals studied herein. A critical failure strain criterion is consistent with the simplest form of the Cockroft-Latham ductile fracture theory based on damage accumulation.

c) Two types of segmentation have been observed, each with a distinct surface morphology (topography) across the chip width, and with characteristic force profiles (oscillatory vs steady). Deciphering of the segmentation morphology requires examination of the chip free-surface topography rather than side-view cross sections as is commonly done. In the latter view, both morphologies appear as one and the same.

d) The segmentation process/flow can be controlled. It can be suppressed by use of a second constraining die across from the primary cutting tool that a priori defines the exit chip geometry (Hybrid Cutting extrusion (HCE) process). This suppression can be explained based on considerations of the stress and strain states in the prow region with and without the constraint. The HCE can be used as a manufacturing process to produce sheet, foil and strip forms in a single deformation step from metal alloys. The segmentation can also be induced or enhanced by application of surface media that can locally embrittle the metal in the prow-deformation zone. This inducement of segmentation can be of value for cutting of very ductile and/or highly strain-hardening metals – the so-called gummy metals.

The work has also answered/clarified many of the questions and misconceptions that have prevailed in the literature about segmented chip formation. These questions were highlighted in the last part of the Introduction chapter.

Our study suggests several avenues for future exploration including a) development and scaling of HCE process for producing commercial sheet and strip forms from metal alloys in a single deformation step b) analysis of HCE energy and deformation c) microstructure/texture and mechanical properties of HCE sheet, d) use of segmentation in cutting to further explore ductile fracture in metals, and e) development of mechanochemical machining processes for gummy metals.

APPENDIX A. SURFACE PROFILE PARAMETER DEFINITIONS AND DETAILS

In this appendix, we define and elaborate on measurement of surface profile (roughness) parameters.

In order to understand and define these parameters, we need to familiarize ourselves with certain aspects of profile measurement [96]. These are:

a) evaluation length, which is the overall length of profile that is being measured; this length is selected to be representative of the true profile;
b) sampling length, which is a subsection of evaluation length.

The sampling length is chosen so that we can separate the roughness (short wavelength) and waviness (long wavelength or form) components of the profile. Typically, in characterization of the surface roughness, the evaluation length will be divided into several sampling lengths. Each sampling length is then analyzed for measurement of roughness parameters.

We have chosen the sampling length for all our roughness measurements in this study so that there are at least 5 sampling lengths included in the evaluation length. For measurements made on the back surface of the chip, the evaluation length is oriented parallel to the chip length direction (i.e., along V_c). For workpiece surface measurements, the evaluation length is along the workpiece length direction (i.e., along V_0). The sampling length is important because features larger than sampling length will filter out as waviness, while features smaller than sampling length will become part of roughness data. In this study, we chose sampling length (l) so that it is long enough to include a minimum of 3 peaks of the profile (3 segments) in each sampling length. This selection ensures that the roughness parameters are representative of the segmentation features and capture the relevant segmentation data.

We report the following roughness parameters - R_a arithmetic average of the roughness profile using a line scan; R_q root mean square deviation of the profile from its average profile using a line scan; S_a arithmetic average of the surface roughness (extension of R_a to a surface), S_q root mean square deviation from average surface (extension of R_q to a surface), and R_z average peak-to-valley profile roughness along a line scan. Note that in this study, we are using the "roughness" parameters to evaluate segmentation features like pitch, amplitude etc and not roughness features of a surface in the conventional sense.

R_a, R_q, and R_z are parameters that are evaluated over a line profile, while S_a and S_q are extracted from 3D profilometry of the surface and are attributed to roughness of a surface. For each profile (surface) that is measured, the evaluation length (evaluation area) is the total length (area) of measurement. The evaluation line (evaluation area) is then divided into sampling lines (sampling areas) of equal length (area).

The next step in profile evaluation is to set the reference line (reference surface) for each of the sampling lines (sampling areas). The reference line (reference surface), which sometimes is called center line (center surface), is positioned so that the sum of the squares of the deviations of the line profile (surface) from this reference line (surface) is a minimum. Accordingly, the reference line (reference surface) for each sampling line (sampling area) is a straight line (flat surface), with a unique slope and intercept.

The roughness parameters such as R_a, R_q, and R_z are defined with respect to center line in each sampling length. Below are the mathematical formulas for these parameters:

$$R_a = \frac{1}{l}\int_0^l Z(x)dx \qquad \text{(A-1)}$$

$$R_q = \sqrt{\frac{1}{l}\int_0^l Z^2(x)dx} \qquad \text{(A-2)}$$

$$R_z = \frac{1}{n}(R_{z1} + R_{z2} + \cdots + R_{zn}) \quad \text{(A-3)}$$

where l is sampling length, $Z(x)$ is the deviation (height) of profile from center line at point (x), and R_{z1} is the single largest peak-to-valley found in each sampling length.

The parameters such as S_a, and S_q are defined analogously, based on the reference surface in each sampling area:

$$S_a = \frac{1}{A}\iint Z(x,y)dxdy \quad \text{(4-5)}$$

$$S_q = \sqrt{\frac{1}{A}\iint Z^2(x,y)dxdy} \quad \text{(4-5)}$$

where A is the sampling area, and $Z(x,y)$ is the deviation (height) of the surface profile from the reference surface at point (x,y).

APPENDIX B. USING THERMAL ETCHING TO STUDY MICRSTRUCTURAL DEPENDENCE OF FLOW IN CUTTING

To study the interplay between microstructure and the deformation in cutting, we have developed thermal etching methods to expose the microstructure in the samples prior to the cutting. These procedures have been established for Cu and Ti. Additionally, we have also carried out *in situ* imaging of cutting using the etched Cu samples to understand how the flow develops with relation to the microstructure.

Thermal Etching and Microstructural Deformation in Cutting

In some OFHC copper specimen prepared through stress-relief annealing at 950°C in an inert atmosphere (argon), it was observed that the grain structure is exposed. In some sense, the heat treatment count as an etching step. This method of revealing the grain boundaries by heating of metals is called thermal etching [94]. The basis of this etching method is preferential transfer of material away from grain boundaries, when metal is exposed to a high temperature in an inert atmosphere. Thus, during annealing of a polished surface, grooves are formed at the intersections of grain boundaries with the bare surface. These grooves remain intact after cooling and are clearly visible at room temperature outlining the grain boundaries. Thermal etching has been explored to some extent in the literature, though many years ago [95], [97]. This suggested the possibility that by carrying out cutting experiments with thermally etched samples we could study the coupling, if any, between deformation and microstructure. In fact, this could be done *in situ* using the imaging setup developed.

The conditions for the thermal etching have been documented for Cu, CP-Ti, and Ti6Al4V. We highlight two early observations using thermally etched Cu and Ti.

Figure A-1 shows a sequence of images in cutting of annealed Cu with the thermally etched samples [8]. At this condition, the chip formation occurs by sinuous flow similar to that shown in Figure 5-14**.** This type of flow is triggered by plastic buckling at the surface ahead of the advancing tool. The images in the sequence show that the extremities of the surface buckle are grain boundaries. The grain deformation is also revealed in the sequence. The second example sequence shows observations using this framework in the Ti system (Figure A-2). We can clearly see grains and their locations. This demonstrates the capability to make microstructure-level observations in Ti, including of segmentation.

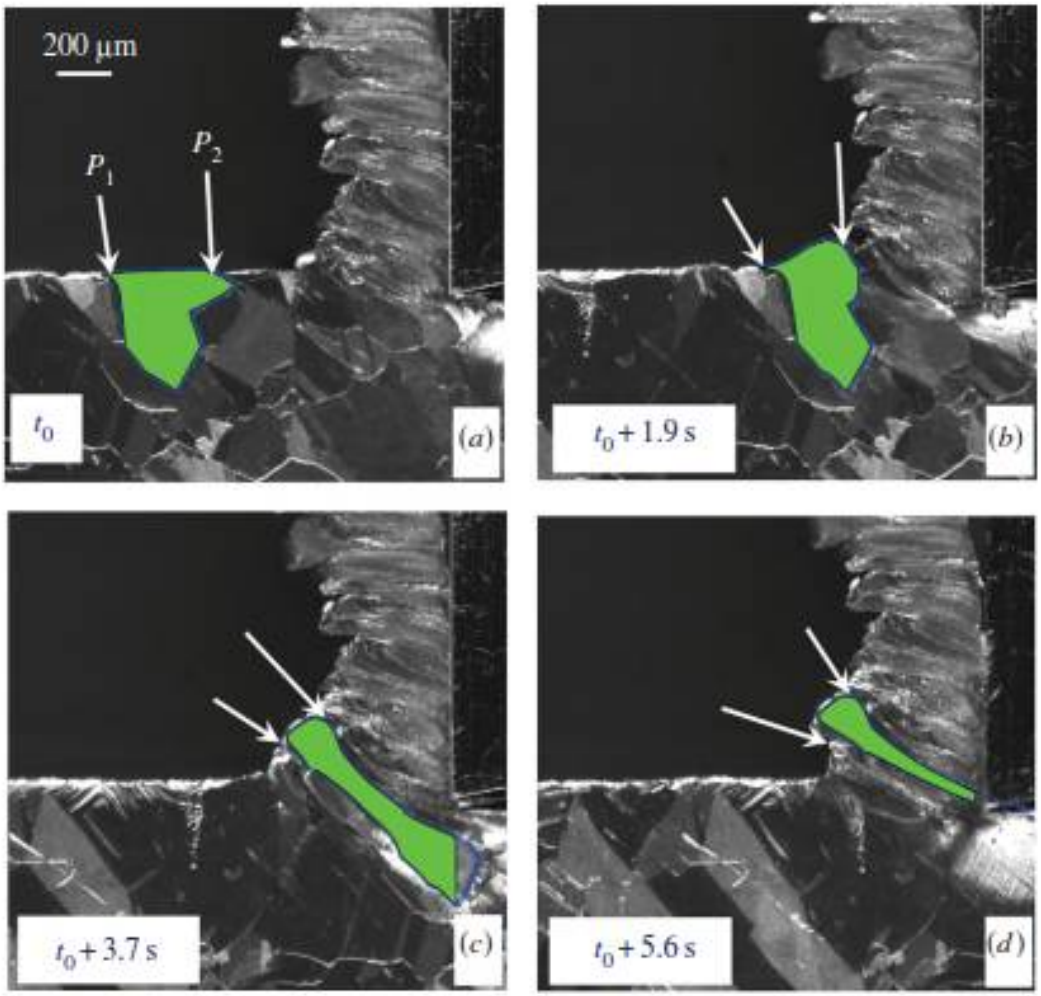

Figure B-1. *In situ* imaging of grain deformation in cutting of annealed Cu with sinuous flow: (a) A Cu grain (green) enters the plastic zone ahead of the tool. Pinning points (see at arrows) are grain boundaries at the free surface. (b) Plastic buckling of a single grain causes a bump on the surface. (c) Simultaneous shear and rotation causes the bump to form a fold between the pinning points (arrows). (d) Fold formation is now complete with a highly elongated final grain. Linear cutting $\alpha = 0°$, $V_0 = 0.5$ mm/s, $t_0 = 50$ μm. [courtesy A. Udupa].

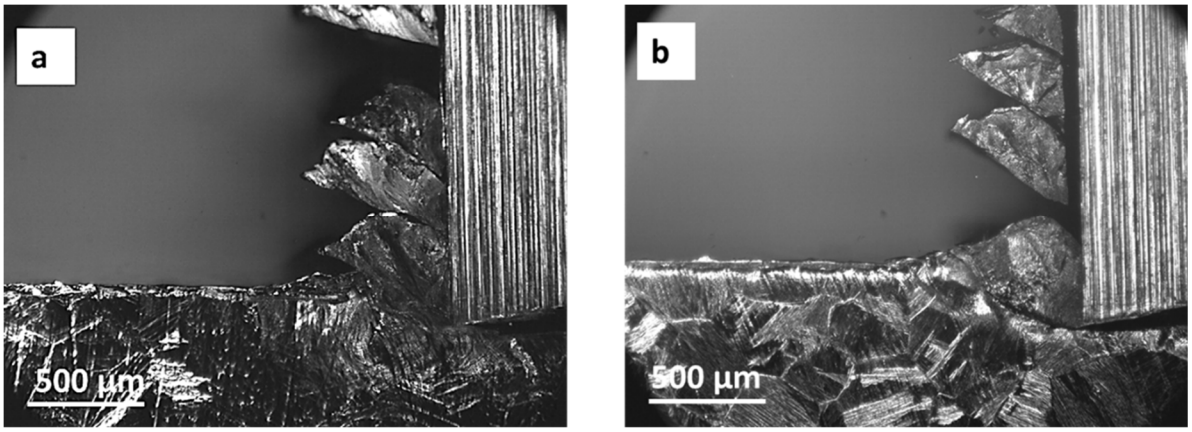

Figure B-2. *In situ* imaging of grain structure in thermally etched Ti: (a) CP Ti Grade 2, and (b) Ti6Al4V. Linear cutting, $\alpha = 0°$, $V_0 = 1$ mm/s.

Since in this framework, we are directly observing the grains and their deformation, it is possible to evaluate dependence of deformation and fracture on grain size. Size effects in cutting can also be explored, especially the relation between grain size and undeformed chip thickness (t_0). It is expected that a small grain size (relative to t_0) will result in laminar flow in cutting of copper, while for a sample with larger grain size we expect to see sinuous flow as shown in Figure 5-14(a).

APPENDIX C. DETAILS OF STRAIN MEASUREMENT IN PROW REGION USING PIV

In Figure 4-13 and Table 4-1, we reported the critical strain (ε^*) values at prow crack point that led to crack initiation at the back-surface of the chip in cutting of Zn and brass. These strain values are calculated by PIV method and tracking of surface elements into the prow region. This is done by integration of incremental strain along specific material flow path lines close to the surface of the workpiece and prow.

It is important to choose the right section of flow for strain analysis to obtain the critical strain (ε^*) value at the correct timestamp. Figure C-1 shows an example of such analysis in cutting of Zn with a tool of rake angle α = -50°. Figure C-1(a) shows the selected section of material that we study in this example. It is in the form of a tilted square because, as shown in figure C-1(b), this shape stays aligned along the direction of concentrated shear band (dashed line A-B) at the onset of crack initiation. Crack initiation in this example occurs at time t_0 where red arrow in part (c), shows the location of crack initiation. We can see that selected area shown in part (b) for critical PIV strain calculation is just above the crack initiation point. The average critical strain (ε^*) in this instance inside the selected area shown in part (b) is 0.84. Part (d) shows the overall strain field in the prow at time t_0. Part(e) shows the same selected area as in part (a) and (b) that is tracked to time (t_0 + 5 ms). As shown in part (f) (blue arrow) crack propagation has already started at this timestamp and it will not lead to correct critical strain value (ε^*) for crack initiation. Hence calculated average strain at time t_0 at the selected area shown in part (b) is the critical strain (ε^*) value at the onset of crack initiation in this example.

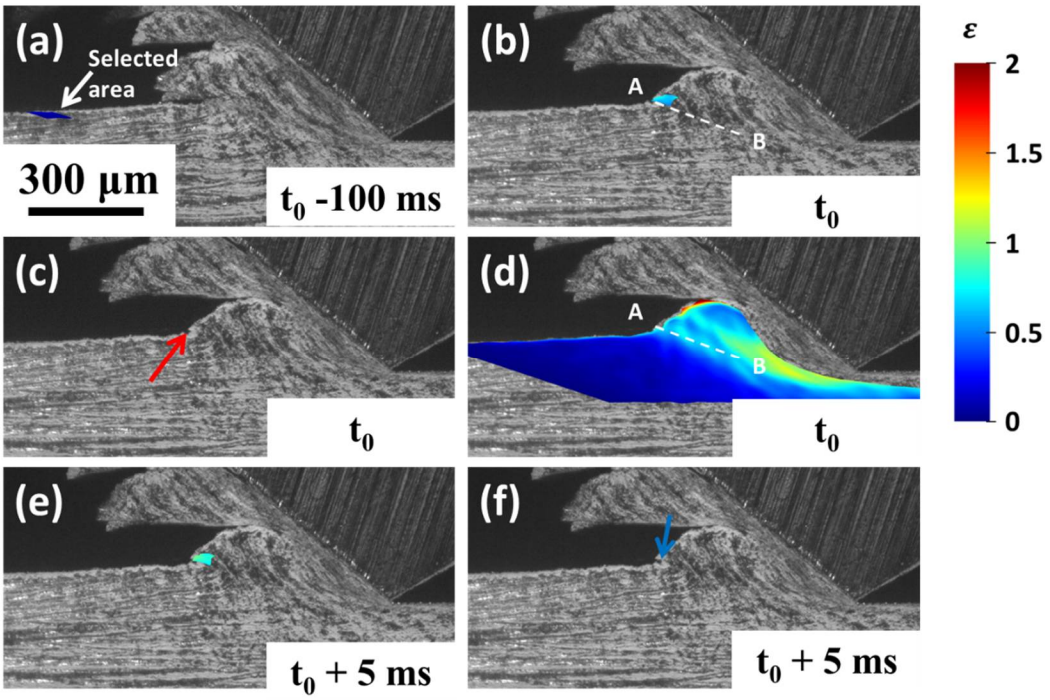

Figure C-1. An example of critical strain (ε^*) calculated through PIV analysis at the onset of crack initiation in cutting of Zn. (a) Selected area to be tracked at the prow region. (b) Strain field in the selected area at the onset of crack initiation in the location of crack initiation point, back-surface of prow. (c) Crack initiation point is shown by red arrow. (d) Overall strain field in the prow at the onset of crack initiation. 5 ms after crack initiation timeline: (e) selected area joins the back-surface of chip, and (f) crack propagation has started represented by blue arrow. Linear cutting α = -50°, V_0 = 1 mm/s, t_0 = 90 µm.

REFERENCES

[1] M. C. Shaw, *Metal cutting principles*. Clarendon Press, 1984.

[2] I. S. Jawahir *et al.*, "Surface integrity in material removal processes: Recent advances," *CIRP Ann.*, vol. 60, no. 2, pp. 603–626, Jan. 2011.

[3] M. E. Merchant, "Mechanics of the Metal Cutting Process. I. Orthogonal Cutting and a Type 2 Chip," *J. Appl. Phys.*, vol. 16, no. 5, pp. 267–275, May 1945.

[4] V. Piispanen, "Theory of Formation of Metal Chips," *J. Appl. Phys.*, vol. 19, no. 10, pp. 876–881, Oct. 1948.

[5] K. Nakayama, "The formation of saw-toothed chip in metal cutting," *Proc. Int. Conf. Prod. Eng. Tokyo*, vol. 1, pp. 572–577, 1974.

[6] K. Viswanathan *et al.*, "On the stability of plastic flow in cutting of metals," *CIRP Ann.*, vol. 66, no. 1, pp. 69–72, Jan. 2017.

[7] H. Yeung, K. Viswanathan, A. Udupa, A. Mahato, and S. Chandrasekar, "Sinuous Flow in Cutting of Metals," *Phys. Rev. Appl.*, vol. 8, no. 5, p. 054044, Nov. 2017.

[8] A. Udupa, K. Viswanathan, Y. Ho, and S. Chandrasekar, "The cutting of metals via plastic buckling," *Proc. R. Soc. A Math. Phys. Eng. Sci.*, vol. 473, no. 2202, p. 20160863, Jun. 2017.

[9] H. Yeung, K. Viswanathan, W. D. Compton, and S. Chandrasekar, "Sinuous flow in metals.," *Proc. Natl. Acad. Sci. U. S. A.*, vol. 112, no. 32, pp. 9828–32, Aug. 2015.

[10] R. F. Recht, "Catastrophic Thermoplastic Shear," *J. Appl. Mech.*, vol. 31, no. 2, p. 189, Jun. 1964.

[11] R. Komanduri, T. Schroeder, J. Hazra, B. F. von Turkovich, and D. G. Flom, “On the Catastrophic Shear Instability in High-Speed Machining of an AISI 4340 Steel,” *J. Eng. Ind.*, vol. 104, no. 2, pp. 121–131, 1982.

[12] D. Sagapuram *et al.*, “Geometric flow control of shear bands by suppression of viscous sliding,” *Proc. R. Soc. A Math. Phys. Eng. Sci.*, vol. 472, no. 2192, p. 20160167, Aug. 2016.

[13] M. C. Shaw and A. Vyas, “The Mechanism of Chip Formation with Hard Turning Steel,” *CIRP Ann.*, vol. 47, no. 1, pp. 77–82, Jan. 1998.

[14] K. Nakayama, M. Arai, and T. Kanda, “Machining Characteristics of Hard Materials,” *CIRP Ann.*, vol. 37, no. 1, pp. 89–92, Jan. 1988.

[15] E. Usui, A. Gujral, and M. C. Shaw, “An experimental study of the action of CCl4 in cutting and other processes involving plastic flow,” *Int. J. Mach. Tool Des. Res.*, vol. 1, no. 3, pp. 187–197, Nov. 1961.

[16] K. Okushima and K. Hitomi, “An Analysis of the Mechanism of Orthogonal Cutting and Its Application to Discontinuous Chip Formation,” *J. Eng. Ind.*, vol. 83, no. 4, pp. 545–555, 1961.

[17] Y. Guo, W. D. Compton, and S. Chandrasekar, “In situ analysis of flow dynamics and deformation fields in cutting and sliding of metals,” *Proc. R. Soc. A Math. Phys. Eng. Sci.*, vol. 471, no. 2178, pp. 20150194–20150194, May 2015.

[18] S. Lee, J. Hwang, M. R. Shankar, S. Chandrasekar, and W. Dale Compton, “Large strain deformation field in machining,” *Metall. Mater. Trans. A*, vol. 37, no. 5, pp. 1633–1643, May 2006.

[19] V. Madhavan, S. Chandrasekar, and T. N. Farris, “Direct Observations of the Chip-Tool Interface in the Low Speed Cutting of Pure Metals,” *J. Tribol.*, vol. 124, no. 3, p. 617, Jul. 2002.

[20] D. Sagapuram, K. Viswanathan, K. P. Trumble, and S. Chandrasekar, “A common mechanism for evolution of single shear bands in large-strain deformation of metals,” *Philos. Mag.*, vol. 98, no. 36, pp. 3267–3299, Dec. 2018.

[21] P. L. B. (Peter L. B. Oxley, *The mechanics of machining : an analytical approach to assessing machinability*. E. Horwood, 1989.

[22] T. L. Brown, S. Swaminathan, S. Chandrasekar, W. D. Compton, A. H. King, and K. P. Trumble, “Low-cost manufacturing process for nanostructured metals and alloys,” *J. Mater. Res.*, vol. 17, no. 10, pp. 2484–2488, Oct. 2002.

[23] M. R. Shankar, B. C. Rao, S. Lee, S. Chandrasekar, A. H. King, and W. D. Compton, “Severe plastic deformation (SPD) of titanium at near-ambient temperature,” *Acta Mater.*, vol. 54, no. 14, pp. 3691–3700, Aug. 2006.

[24] P. L. B. Oxley and W. F. Hastings, “Predicting the Strain Rate in the Zone of Intense Shear in which the Chip is Formed in Machining from the Dynamic Flow Stress Properties of the Work Material and the Cutting Conditions,” *Proc. R. Soc. A Math. Phys. Eng. Sci.*, vol. 356, no. 1686, pp. 395–410, Sep. 1977.

[25] M. Sevier, H. T. Y. Yang, S. Lee, and S. Chandrasekar, “Severe Plastic Deformation by Machining Characterized by Finite Element Simulation,” *Metall. Mater. Trans. B*, vol. 38, no. 6, pp. 927–938, Dec. 2007.

[26] R. M'Saoubi and L. Ryde, "Application of the EBSD technique for the characterisation of deformation zones in metal cutting," *Mater. Sci. Eng. A*, vol. 405, no. 1–2, pp. 339–349, Sep. 2005.

[27] K.-H. Zum Gahr, *Microstructure and wear of materials*. Elsevier, 1987.

[28] L. E. Samuels, *Metallographic polishing by mechanical methods*. ASM International, 2003.

[29] H. Wilman, "Abrasion and surface structure," *Wear*, vol. 14, no. 4, pp. 249–254, Oct. 1969.

[30] G. Boothroyd and G. Boothroyd, "Temperatures in Orthogonal Metal Cutting," *Proc. Inst. Mech. Eng.*, vol. 177, no. 1, pp. 789–810, Jun. 1963.

[31] T. W. Wright, *The physics and mathematics of adiabatic shear bands*. Cambridge University Press, 2002.

[32] S. L. Semiatin and S. B. Rao, "Shear localization during metal cutting," *Mater. Sci. Eng.*, vol. 61, no. 2, pp. 185–192, Nov. 1983.

[33] W. A. Backofen, *Deformation processing*. .

[34] Z. P. Bažant and L. Cedolin, *Stability of structures : elastic, inelastic, fracture, and damage theories*. Dover Publications, 2003.

[35] E. OROWAN, "A TYPE OF PLASTIC DEFORMATION NEW IN METALS," *Nature*, vol. 149, no. 3788, pp. 643–644, Jun. 1942.

[36] W. Kluft, C. A. van Luttervelt, K. Nakayama, and A. J. Pekelharing, "PRESENT KNOWLEDGE OF CHIP CONTROL.," *CIRP Ann. - Manuf. Technol.*, vol. 28, no. 2, pp. 441–455, 1979.

[37] A. Udupa, T. Sugihara, K. Viswanathan, and S. Chandrasekar, "Altering the Stability of Surface Plastic Flow via Mechanochemical Effects," *Phys. Rev. Appl.*, vol. 11, no. 1, p. 014021, Oct. 2019.

[38] D. M. Turley, E. D. Doyle, and S. Ramalingam, “Calculation of shear strains in chip formation in titanium,” *Mater. Sci. Eng.*, vol. 55, no. 1, pp. 45–48, Aug. 1982.

[39] A. Vyas and M. C. Shaw, “Mechanics of Saw-Tooth Chip Formation in Metal Cutting,” *J. Manuf. Sci. Eng.*, vol. 121, no. 2, p. 163, May 1999.

[40] Y. L. Bai, “Thermo-plastic instability in simple shear,” *J. Mech. Phys. Solids*, vol. 30, no. 4, pp. 195–207, Aug. 1982.

[41] B. Dodd and Y. Bai, *Adiabatic Shear Localization.* Elsevier Science & Technology, 2012.

[42] K. Nakayama and M. Arai, “Role of Brittleness of Work Material in Metal Cutting,” *Influ. Metall. Mach. Steel. Iron Steel Inst. Japan, Tokyo. 1977, 421-432*, Jan. 1977.

[43] T. J. WALKER and M. C. SHAW, “ON DEFORMATION AT LARGE STRAINS,” *Adv. Mach. Tool Des. Res. 1969*, pp. 241–252, Jan. 1970.

[44] R. Komanduri and R. H. Brown, “On the Mechanics of Chip Segmentation In Machining,” *J. Manuf. Sci. Eng. Trans. ASME*, vol. 103, no. 1, p. 33, 1981.

[45] B. van der Pol, “On Relaxation Oscillations,” *Philos. Mag.*, vol. 2, no. 11, pp. 978–992, Nov. 1926.

[46] M. C. Shaw and A. Vyas, “Chip Formation in the Machining of Hardened Steel,” *CIRP Ann. - Manuf. Technol.*, vol. 42, no. 1, pp. 29–33, 1993.

[47] P. W. Bridgman, “The Stress Distribution at the Neck of a Tension Specimen,” *Trans. A.S.M.*, vol. 32, pp. 553–574, 1944.

[48] P. W. Bridgman, *Studies in large plastic flow and fracture*. Cambridge, MA: Harvard University Press, 1964.

[49] H. D. Pugh, *Mechanical behaviour of materials under pressure*. Elsevier Pub. Co., 1970.

[50] H. D. Pugh and D. Green, “The Effect of Hydrostatic Pressure on the Plastic Flow and Fracture of Metals,” *Proc. Inst. Mech. Eng.*, vol. 179, no. 1, pp. 415–437, Jun. 1964.

[51] I. E. French and P. F. Weinrich, “The effects of hydrostatic pressure on the mechanism of tensile fracture of aluminum,” *Metall. Trans. A*, vol. 6, no. 6, pp. 1165–1169, Jun. 1975.

[52] I. E. French and P. F. Weinrich, “The influence of hydrostatic pressure on the tensile deformation and fracture of copper,” *Metall. Trans. A*, vol. 6, no. 4, pp. 785–790, Apr. 1975.

[53] I. . French and P. . Weinrich, “The effect of hydrostatic pressure on the tensile fracture of α-brass,” *Acta Metall.*, vol. 21, no. 11, pp. 1533–1537, Nov. 1973.

[54] I. . French, P. . Weinrich, and C. . Weaver, “Tensile fracture of free machining brass as a function of hydrostatic pressure,” *Acta Metall.*, vol. 21, no. 8, pp. 1045–1049, Aug. 1973.

[55] F. McClintock, “Local criteria for ductile fracture,” *Int. J. Fract. Mech.*, vol. 4, no. 2, pp. 101–130, Jun. 1968.

[56] F. McClintock, “CRACK GROWTH IN FULLY PLASTIC GROOVED TENSILE SPECIMENS,” *Pap. FROM Phys. STRENGTH Plast. M. I. T. Press. CAMBRIDGE, MASS. 1969, 307-326*, Jan. 1969.

[57] G. R. Johnson and W. H. Cook, “Fracture characteristics of three metals subjected to various strains, strain rates, temperatures and pressures,” *Eng. Fract. Mech.*, vol. 21, no. 1, pp. 31–48, Jan. 1985.

[58] F. A. McClintock, “A Criterion for Ductile Fracture by the Growth of Holes,” *J. Appl. Mech.*, vol. 35, no. 2, p. 363, Jun. 1968.

[59] J. R. Rice and D. M. Tracey, “On the ductile enlargement of voids in triaxial stress fields,” *J. Mech. Phys. Solids*, vol. 17, no. 3, pp. 201–217, Jun. 1969.

[60] G. Le Roy, J. D. Embury, G. Edwards, and M. F. Ashby, “A model of ductile fracture based on the nucleation and growth of voids,” *Acta Metall.*, vol. 29, no. 8, pp. 1509–1522, Aug. 1981.

[61] M. G. Cockroft and D. J. Latham, “Ductility and the Workability of Metals,” *J. Inst. Met.*, vol. 96, pp. 33–39, 1968.

[62] S. I. Oh, C. C. Chen, and S. Kobayashi, “Ductile Fracture in Axisymmetric Extrusion and Drawing—Part 2: Workability in Extrusion and Drawing,” *J. Eng. Ind.*, vol. 101, no. 1, p. 36, Feb. 1979.

[63] S. E. Clift, P. Hartley, C. E. N. Sturgess, and G. W. Rowe, “Fracture prediction in plastic deformation processes,” *Int. J. Mech. Sci.*, vol. 32, no. 1, pp. 1–17, Jan. 1990.

[64] Y. Bao and T. Wierzbicki, “A Comparative Study on Various Ductile Crack Formation Criteria,” *J. Eng. Mater. Technol.*, vol. 126, no. 3, p. 314, Jul. 2004.

[65] Y. Bao and T. Wierzbicki, “On fracture locus in the equivalent strain and stress triaxiality space,” *Int. J. Mech. Sci.*, vol. 46, no. 1, pp. 81–98, Jan. 2004.

[66] T. Wierzbicki, Y. Bao, Y.-W. Lee, and Y. Bai, “Calibration and evaluation of seven fracture models,” *Int. J. Mech. Sci.*, vol. 47, no. 4–5, pp. 719–743, Apr. 2005.

[67] *ASM Handbook Volume 12: Fractography*. ASM International, 1987.

[68] D. Hull, *Fractography : observing, measuring, and interpreting fracture surface topography*. Cambridge University Press, 1999.

[69] W. D. Biggs, *The brittle fracture of steel*. Pitman Publishing Corporation, 1960.

[70] C. Tipper, *The brittle fracture story.* Cambridge [England]: University Press, 1962.

[71] P. V Dembowski, J. Pepe, and T. E. Davidson, “Hydrostatic pressure induced ductility transitions in pure bismuth and tin-bismuth alloys,” *Acta Metall.*, vol. 22, no. 9, pp. 1121–1131, Sep. 1974.

[72] M. Oyane, T. Sato, K. Okimoto, and S. Shima, “Criteria for ductile fracture and their applications,” *J. Mech. Work. Technol.*, vol. 4, no. 1, pp. 65–81, Apr. 1980.

[73] W. B. Palmer and P. L. B. Oxley, “Mechanics of orthogonal machining,” *Arch. Proc. Inst. Mech. Eng. 1847-1982 (vols 1-196)*, vol. 173, no. 1959, pp. 623–654, 1959.

[74] W. B. H. Cooke and W. B. Rice, “Inhomogeneous shearing during continuous chip formation,” *J. Eng. Ind.*, vol. 95, no. 3, p. 844, Aug. 1973.

[75] J. H. Dautzenberg and J. H. Zaat, “Quantitative determination of deformation by sliding wear,” *Wear*, vol. 23, no. 1, pp. 9–19, 1973.

[76] N. K. Sundaram, Y. Guo, and S. Chandrasekar, “Mesoscale folding, instability, and disruption of laminar flow in metal surfaces,” *Phys. Rev. Lett.*, vol. 109, no. 10, pp. 1–5, 2012.

[77] A. Mahato, Y. Guo, N. K. Sundaram, and S. Chandrasekar, “Surface folding in metals: a mechanism for delamination wear in sliding.,” *Proc. Math. Phys. Eng. Sci.*, vol. 470, no. 2169, p. 20140297, 2014.

[78] M. Raffel, C. Willert, S. Wereley, and J. Kompenhans, *Particle Image Velocimetry, A Practical Guide*, 2nd ed. New York: Springer, 2007.

[79] R. J. Adrian, “Particle-Imaging Techniques for Experimental Fluid Mechanics,” *http://dx.doi.org/10.1146/annurev.fl.23.010191.001401*, Nov. 2003.

[80] T. G. Murthy, J. Madariaga, and S. Chandrasekar, “Direct mapping of deformation in punch indentation and correlation with slip line fields,” *J. Mater. Res.*, vol. 24, no. 03, pp. 760–767, Mar. 2009.

[81] E. P. Gnanamanickam, S. Lee, J. P. Sullivan, and S. Chandrasekar, “Direct measurement of large-strain deformation fields by particle tracking,” *Meas. Sci. Technol.*, vol. 20, no. 9, p. 095710, Sep. 2009.

[82] W. F. Hosford and R. M. Caddell, *Metal forming : mechanics and metallurgy*. Cambridge University Press, 2007.

[83] T. Thomsen and E. G. (Erich G. Thomsen, *Mechanics of plastic deformation in metal processing*. .

[84] M. F. Littmann, “Iron and Silicon-Iron Alloys,” *IEEE Trans. Magn.*, vol. 7, no. 1, pp. 48–60, 1971.

[85] J. M. D. Coey, *Magnetism and magnetic materials*. 2010.

[86] D. Sagapuram *et al.*, “On control of flow instabilities in cutting of metals,” *CIRP Ann.*, vol. 64, no. 1, pp. 49–52, Jan. 2015.

[87] J. B. Mann, M. Saei, A. Udupa, B. S. Puentes-Rodriguez, and D. Sagapuram, “Applications of Machining in Materials Manufacturing,” 2020.

[88] R. M. Latanision, “Surface effects in crystal plasticity,” *Adv. Colloid Interface Sci.*, vol. 6, no. 4, pp. 267–312, Dec. 1976.

[89] A. Udupa, K. Viswanathan, M. Saei, J. B. Mann, and S. Chandrasekar, “Material-Independent Mechanochemical Effect in the Deformation of Highly-Strain-Hardening Metals,” *Phys. Rev. Appl.*, vol. 10, no. 1, p. 014009, Jul. 2018.

[90] M. Efe, W. Moscoso, K. P. Trumble, W. Dale Compton, and S. Chandrasekar, “Mechanics of large strain extrusion machining and application to deformation processing of magnesium alloys,” *Acta Mater.*, vol. 60, no. 5, pp. 2031–2042, Mar. 2012.

[91] S. Yadav, G. Feng, and D. Sagapuram, “Dynamics of shear band instabilities in cutting of metals,” *CIRP Ann.*, vol. 68, no. 1, pp. 45–48, Jan. 2019.

[92] D. Sagapuram, M. Efe, W. Moscoso, S. Chandrasekar, and K. P. Trumble, “Controlling texture in magnesium alloy sheet by shear-based deformation processing,” *Acta Mater.*, vol. 61, no. 18, pp. 6843–6856, Oct. 2013.

[93] D. Sagapuram, M. Efe, K. P. Trumble, and S. Chandrasekar, “Flow transitions and flow localization in large-strain deformation of magnesium alloy,” *Mater. Sci. Eng. A*, vol. 659, pp. 295–305, Apr. 2016.

[94] W. W. Mullins, “Theory of Thermal Grooving,” *J. Appl. Phys.*, vol. 28, no. 3, pp. 333–339, Mar. 1957.

[95] W. . Mullins, “The effect of thermal grooving on grain boundary motion,” *Acta Metall.*, vol. 6, no. 6, pp. 414–427, Jun. 1958.

[96] H. Dagnall, *Exploring surface texture*. Rank Taylor Hobson, 1980.

[97] W. W. Mullins and P. G. Shewmon, “The kinetics of grain boundary grooving in copper,” *Acta Metall.*, vol. 7, no. 3, pp. 163–170, Mar. 1959.